Understanding the origin of glass forming ability in metallic glasses

Thesis by
Andrew Hoff

In Partial Fulfillment of the Requirements for the
degree of
Doctor of Philosophy

CALIFORNIA INSTITUTE OF TECHNOLOGY
Pasadena, California

2018
Defended May 25, 2018

ACKNOWLEDGEMENTS

Like my time here at Caltech, this acknowledgments section runs a bit too long and yet feels like there is so much not yet done. There are far too many people who I need to thank, so to anyone who is not named I apologize in advance, you were very much appreciated.

First and foremost I want to thank my advisor, Professor Bill Johnson. When I visited Caltech as a prospective student metallic glasses and his research were not on my radar. Indeed, metallurgy was probably the area of study I was least interested in, and the group website which was 5 years out of date did not help my interest. His presentation to the prospective students got me hooked, and while I knew nothing about the field his presentation was inspiring. More importantly, I knew he was the person I wanted to work for, and seven years later I am so thankful for the opportunity he gave me. His guidance and help, his always open door, the multi-hour conversations that started from simple questions, his insatiable and infectious desire to learn, and generosity with time have made my time at Caltech wonderful. I will always appreciate his guidance and mentoring.

My work here could not have been done without the help of numerous people in lab. Marios Demetriou in particular has been a constant source of ideas, feedback, and help. I would not have been able to accomplish what I have without his help and guidance. Michael Floyd has been significant help with equipment in lab and was my go to person to run ideas by. I thank him for making the lab a little less solitary these last few years. Georg Kaltenboeck has provided critical help with viscosity measurements, machining, and other lab equipment, but I would be remiss if I did not also thank him for making my job easier with his excellent APh105 solution sets. Scott Roberts taught me how to use and maintain a good portion of the equipment in lab. My life would have been easier had I listened to his advice on avoiding being the person in charge of fixing equipment. Hillary Smith has helped me immensely with my calorimetry work. I also thank her for the opportunity to go on beam time, which was an incredible experience. Matt Johnson was an excellent help for all sorts of lab questions, his experience proved invaluable on more than one occasion. Jong Hyun Na got me started on fragility measurements and provided me with material, which was incredibly helpful.

I had wonderful students who worked with me in the summer. I was blessed to be able to work with David Joseph, Lindsay Ladd, and Katherine Tighe, and I hope they gained as much as I did from our time working together.

Everyone mentioned has been wonderful, but there are a few people that deserve particular mention for non-work reasons. Professor Brent Fultz has been a wonderful mentor and I have appreciated the insights and guidance he has provided throughout the years. Glenn Garrett was my first mentor in the Johnson group when I arrived at Caltech and I have appreciated his guidance and friendship since. Dale Connor had a particular quality that made him the best officemate I could have asked for: his usual absence from the office. I miss those long, rambling conversations we had when we both had better things to do.

I cannot express how grateful I am to have had such wonderful admins during my time here. Christy Jenstad gets a particular shoutout as someone who was always looking out for me, got me the best TA position ever, and just made the department a wonderful place. She also gave me a couch. There is a reason that for years I would tell prospective students "And this sounds crazy, but Christy is seriously a great reason to consider Caltech." Pam Albertson was an amazing source of help, and I really appreciated the work she did to ensure I got paid and that the lab ran smoothly. Jennifer Blankenship was helpful in every position she held, but I especially appreciated her help in running the MRLs. On that note, I appreciate Tiffany Kimoto, Liz Jennings, Michelle Rodriguez, Cecilia Gamboa, Sonya Lincoln, Celene Barrera, and Jonathan Gross for helping me immeasurably in trying to track down faculty or in general actually get the MRLs working. Thanks to Connie for letting me help TA APh 100 and for always letting me use the fax machine. Thanks to Pam, Celene, Jonathan, Christy, and Jennifer who have all had to help me throughout the years with reimbursements. I know the last thing they want to do is deal with dozens of crinkled receipts, so I thank them for their patience.

There are many people who have helped me get to where I am, but I am most indebted to my family for my success. There is no way to convey the depth of the gratitude I have for the love, comfort, guidance, and unconditional support they have given me throughout my life.

Last but certainly not least, I would like to thank Melissa. She has been incredibly supportive and helpful and has encouraged me during challenging times. My time at Caltech would not have been nearly as enjoyable without her. Thank you.

ABSTRACT

The glass forming ability of metallic glasses has been one of their most studied yet least understood properties. Crystal nucleation in a recently development Ni-based metallic glass was studied by undercooling in a DSC under a variety of conditions and showed stochastic very deep undercooling behavior. The glass forming ability of a family of Ni-based alloys was analyzed and was found to depend only on two experimentally accessible factors, the reduced glass transition temperature and the liquid fragility. Neutron scattering experiments showed that in two model glass formers vibrational entropy had essentially no change through the glass transition, demonstrating that the change in entropy through the glass transition is due almost entirely to configurational entropy. The configurational enthalpy of a pair of recently developed Pt-based metallic glasses show almost no change in the undercooled liquid between the liquidus and TTT-nose, demonstrating the inability of current models to explain the thermodynamics of supercooled liquids.

PUBLISHED CONTENT AND CONTRIBUTIONS

[1] Jong Hyun Na et al. “Compositional landscape for glass formation in metal alloys”. In: *PNAS* 111.25 (2014), pp. 9031–9036. DOI: 10.1073/pnas.1407780111.
I measured the fragility of the alloys.

[2] Hillary L. Smith et al. “Separating the configurational and vibrational entropy contributions in metallic glasses”. In: *Nature Physics* 13 (2017), pp. 900–906. DOI: 10.1038/NPHYS4142.
I made and prepared samples, collected neutron scattering data, collected heat capacity data.

TABLE OF CONTENTS

LIST OF ILLUSTRATIONS

Number *Page*

Chapter 1

THE EFFECTS OF PROCESSING ON NUCLEATION IN THE BULK GLASS FORMING ALLOY $Ni_{71.4}Cr_{5.52}Nb_{3.38}P_{16.67}B_{3.03}$

1.1 Abstract

Nucleation of a nickel-based metallic glass was studied by heating and cooling samples in flux in a Netzsch 404C DSC at cooling rates far below the critical cooling rate. Experiments indicate that at DSC cooling rates there is a potent nucleation pathway whose temperature depends on processing conditions, but fluxing and overheating can occasionally increase the degree of undercooling that can be achieved. While no glasses were ever made in the DSC, a large sporadic jump in maximum undercooling indicates that intrinsic GFA in this and related systems may be much higher than achievable GFA when processed.

1.2 Introduction

Glasses are an integral part of everyday life for a large portion of the world, and have been used throughout history for artistic, religious, and practical purposes. The study and improvement of glasses is as old as humanity's use of glasses, but there is still much that remains unknown about them. Glasses are formed when a liquid is cooled sufficiently quickly that crystallization is avoided. Once the material is cooled below the glass transition temperature, a phenomena that will be discussed in great detail throughout this thesis, it becomes a glass. As a glass, it maintains a liquid-like atomic configuration, with atoms that lack any long-range order.

Glasses below the glass transition structurally behave as solids. Because there is no crystal structure, there are no grains. This means that normal mechanisms of crystal deformation and plasticity which rely on dislocations are not available to glasses, which is the cause of the brittleness of glasses. This brittleness and tendency towards catastrophic failure modes limits glass to largely non-structural applications, with the transparent nature of soda lime and other oxide glass making it very useful for windows, jars, and other transparent containers. It is only when a glass is heated above its glass transition temperature that it is able to flow and be processed. One reason why glass could be used throughout history is that many glasses like soda lime

glass have very long timescales to crystallization in this temperature range between the glass transition and the melting temperature. This is the basis of glassblowing, and many of these glasses can be processed for as long as necessary without any risk of crystallization.

While oxide glasses based on SiO_2 are the glasses most commonly encountered, many materials can form glassy states. This work concerns itself with metallic glasses, which are metal alloys that are rapidly quenched to lock in the glassy state. These materials have unique mechanical, electrical, and magnetic properties compared to crystalline metals.

Metallic glasses were first discovered in 1960 by Pol Duwez at Caltech[44]. Before the development of the gold silicon alloy in that paper, metallic glasses were not considered possible, as it was believed that crystallization in metal systems happened too rapidly for a glass to form. That first metallic glass required a cooling rate above 10^6 K/s, which limited the samples to being on the order of ten microns thick and required specialized equipment to make. After that discovery an effort was made to find different alloy systems that made glasses and to understand the properties of these materials. Early work identified superconductors and magnetic cores as potential use cases of metallic glasses, with the magnetic properties of metallic glasses finding particular interest. Due to the limitations of being only able to make thin materials, the mechanical properties of metallic glasses were not strongly pursued, and an industry around making very high efficiency metallic glass transformer cores developed. For quite a while after being discovered, transformer cores and nickel-based brazing foils were the only real applications of metallic glasses, as they could be manufactured using melt spinning. Parts that would require thicker cross sections were unable to be manufactured, as thicker parts necessarily cool more slowly, giving the material enough time to crystallize.

Of all the macroscopic properties of metallic glasses, the glass forming ability (GFA) of these alloys have been one of the most studied and yet least understood. One challenge in understanding glass forming ability is the difficulty in defining what exactly GFA is. For purposes of this thesis glass forming ability will be defined either as the diameter of the maximum rod that can be made amorphous, the critical cooling rate of the alloy, or the time to crystallization at the nose of the TTT diagram. These definitions are all related and care will be taken to ensure clarity in the text. Unless otherwise noted, the maximum casting diameter is the definition

most commonly used as it is generally the easiest to determine (but is, perhaps, the least consistent of the definitions).

In comparison to other glasses, notably silicate glasses, metallic glasses as a whole have significantly smaller processing windows and significantly smaller GFA. The best glass forming alloy found to date, $Pd_{40}Cu_{30}Ni_{10}P_{20}$, has had a 7.2 cm diameter cylinder successfully cast[35], more commercially oriented alloys are substantially smaller. Any attempt to make an amorphous rod larger than the maximum GFA will fail, as the samples will not cool fast enough and will crystallize before forming a glass. The crystallization behavior of metallic glasses varies widely depending on composition. Generally, crystallization of one part of a sample will lead to further crystallization of the rest of the sample. Some alloys can be processed into metallic glass matrix composites which exhibit significantly higher toughness than monolithic metallic glasses[33], but as a general rule crystallization of metallic glasses is a strongly undesirable phenomenon. Because processing and manufacturing of parts will use processes substantially less optimal for maximizing GFA, in practice parts will be confined to be substantially smaller than the already relatively small GFA. This is because commercial manufacturing of metallic glasses would not allow for high purity atmospheres research grade materials, and would introduce high strain rates and complicated flow patterns (in casting processes). These processing constraints and other related challenges have been a large factor in the inability of metallic glasses to be manufactured on a commercial scale for the wide variety of applications that could benefit from the other, largely mechanical, properties that metallic glasses bring to the table.

1.3 Classical Nucleation Theory

To form a glass, nucleation of a crystal phase must be avoided upon cooling from the melt. Above the liquidus the material will exist as a homogeneous liquid with no crystals present. Between the liquidus and the solidus solid and liquid phases coexist when in thermodynamic equilibrium. Below the solidus no liquid is favored thermodynamically, it can only be due to challenges in nucleating a crystal phase that a liquid will exist upon cooling from a melt. All metals can be cooled below their thermodynamic melting point. Even pure metals, which until recently[101] had never been successfully cooled from a melt into a glass, can be cooled to $.8T_M$ with care but without too much difficulty[84]. Multicomponent alloys, particularly ones based around eutectics, can be undercooled significantly further.

At temperatures just below the liquidus the difference in energy between the solid and liquid phases is small. This difference in energies, the thermodynamic driving force, is small for small undercoolings and grows the further the sample is undercooled. It is important to note that even though the driving force is small for small undercoolings, once a crystal is successfully nucleated it will grow as it is the favored phase. At very deep undercoolings the thermodynamic driving force becomes very significant. It is only the kinetic freezing of the liquid configuration that prevents the crystal from forming. Understanding the thermodynamics of crystal nucleation in liquids is critical to understanding nucleation phenomena. Classical nucleation theory (CNT) is a theory that was developed to account for nucleation of phases but notably has been applied to the nucleation of crystals from undercooled liquids. CNT misses some key elements of the physics of crystal nucleation, particularly for deeply undercooled liquids. The nucleation rates predicted by CNT can be many orders of magnitude off compared to experimental data, and the discussion section of Chapter 2 details a way in which the physical intuition of CNT is likely wrong. However, it is still a useful framework for understanding some of the mechanisms involved.

Classical nucleation theory has been developed far beyond what will covered here, but in its most basic form starts from the assumption of a homogeneous liquid with composition fluctuations. These fluctuations create and destroy local regions of short range order, and some of those regions have the order of a crystal phase. At temperatures below the liquidus, there is at least one crystal phase that has a lower energy than the liquid, and below the solidus there are no thermodynamically stable liquids. These regions, called clusters, have competing energy terms. The bulk of the cluster is lower energy than the surrounding liquid, but there is an interface between the cluster and the liquid that has an energy cost. When the interfacial term dominates, thermodynamics favors a dissolution of the cluster, while if the bulk dominates, it has the tendency to nucleate into a crystal. Due to simplicity and energy minimizing reasons, spherical clusters are the pedagogical choice for showing nucleation. Because the volume for a sphere (bulk) grows as r^3 whereas surface area for a sphere (interface) grows as r^2, there becomes a critical radius where the different terms switch in terms of dominance. Below this critical radius, the cluster tends to shrink, while above, it tends to grow.

This interface is the nucleation barrier in CNT, without this barrier nucleation would occur significantly quicker as thermodynamics would encourage the growth of even

few atom clusters that would eventually become nucleation centers. Starting from the assumption of spherical clusters, the Gibbs free energy of the cluster can be written as:

$$\Delta G = \frac{4}{3}\pi r^3 \Delta G_v + 4\pi r^2 \sigma \tag{1.1}$$

where ΔG is the difference in energy between the cluster and the surrounding liquid, r is the radius of the cluster, ΔG_v is the Gibbs free energy difference between the bulk phase of the cluster and the liquid (below the liquidus this term is negative), and σ is the interfacial energy. It is clear from this expression that the first term is the bulk term and takes the form of the volume of a sphere, whereas the second term is interfacial and takes the form of the surface area.

It can be readily seen by differentiating ΔG with respect to r and setting it equal to zero that the critical radius for a cluster is

$$r^* = \frac{2\sigma}{|\Delta G_v|} \tag{1.2}$$

This expression, while perhaps overly simplistic, suggests that the only factors that need to be worried about are the interfacial energy between the crystal and liquid as well as the free energy of formation of the crystal at the given temperature. A schematic of this can be seen in Fig. 1.1.

The easiest modification to the classical theory concerns heterogeneous nucleation sites. The preceding equations works when you have a homogeneous liquid which only can interact with itself. In reality, everything from container walls to impurities in the liquid can and do act as nucleation sites. The effects of these sites is to lower the free energy of forming a crystal by reducing the area of high energy surfaces. This occurs because as the cluster is forming on these sites the interfacial energy between the cluster and the substrate is lower than that of the cluster and the liquid. This lower energy surface reduces the energy required to create the cluster by a geometric factor:

$$\Delta G = \left(\frac{4}{3}\pi r^3 \Delta G_v + 4\pi r^2 \sigma\right) f(\theta) \tag{1.3}$$

where $f(\theta)$ is bounded by $0 \leq f(\theta) \leq 1$ and is given by the geometry of the nucleation site (often given as a spherical cap)[43]. The effect of these heterogeneous nucleation

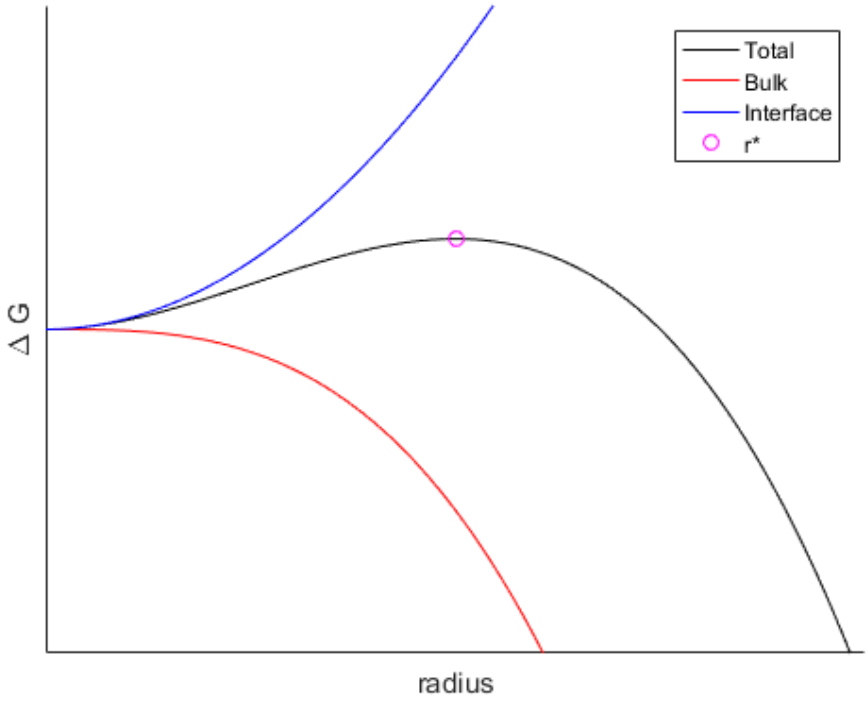

Figure 1.1: Schematic diagram of the energies of cluster formation in classical nucleation theory. The total energy is a competition between two forces, the bulk energy which is lower than the liquid, and an interfacial term which acts to raise the overall energy of the cluster. At small radii the cluster energy is positive and so thermodynamically wants to shrink to zero. If the radius of the cluster grows, it passes a critical radius (denoted as r*) after which it becomes thermodynamically favorable for the cluster to continue growing and is statistically likely to grow. As a liquid is further undercooled the bulk term becomes more dominant, reducing the critical radius needed for a cluster to turn into a crystal nucleation site.

sites is to make crystal formation significantly easier, reducing the timescale for a cluster of critical size to be formed. For glass forming systems, this will mean that quenching will need to be done quicker when heterogeneous nucleation sites are present to prevent crystal nucleation. In practice, when heterogeneous nucleation sites are available it will almost exclusively be the pathway in which nucleation occurs.

While CNT provides a nice and intuitively appealing framework for thinking about nucleation it falls short in making concrete predictions for metallic glasses[69][6]. The value in using CNT to underpin our physical intuition of crystal nucleation in these systems is strongly limited by a large caveat. One big factor in CNT, the role of the interface between the liquid and solid, may not be the physical mechanism limiting crystallization in metallic glasses. Chapter 2 will cover work done to create a model of GFA, and in that model this interfacial energy does not affect GFA.

CNT attempts to cover the thermodynamics, but as mentioned earlier, the kinetics of deeply undercooled liquids is what prevents glasses from spontaneously crystallizing at low temperatures. To see this interplay between kinetics and thermodynamics it is useful to look at a time-temperature-transformation (TTT) diagram, as seen in Fig. 1.2.

This TTT diagram of Vitreloy 1 was created in an electrostatic levitator. In contrast with the predictions of a simple CNT model, where the lower temperatures would lead to greater thermodynamic driving forces and hence nucleation rates, the temperature that exhibits the quickest crystallization is around 585°C, closer to the liquidus temperature than the glass transition. This "nose" temperature minimizes the time to crystallization, with temperatures above and below the nose having significantly longer times to crystallization. Above the nose temperature there is not a strong driving force to crystallize, whereas below the nose temperature there is a strong driving force but diffusion is so slow that atoms cannot rearrange themselves in time. TTT diagrams are defined by doing isothermal holds until the transformation, but practically, if the sample is continuously cooled past the nose temperature it will become a glass without crystallizing. Continuous cooling curves look a little different than the TTT diagram shown in Fig. 1.2, especially for the part of the curve below the nose, but the TTT curve is still a very useful pedagogical tool for understanding the mechanics of crystallization in continuously cooled samples. Cooling rates slower than the critical cooling rate will result in hitting the top of the

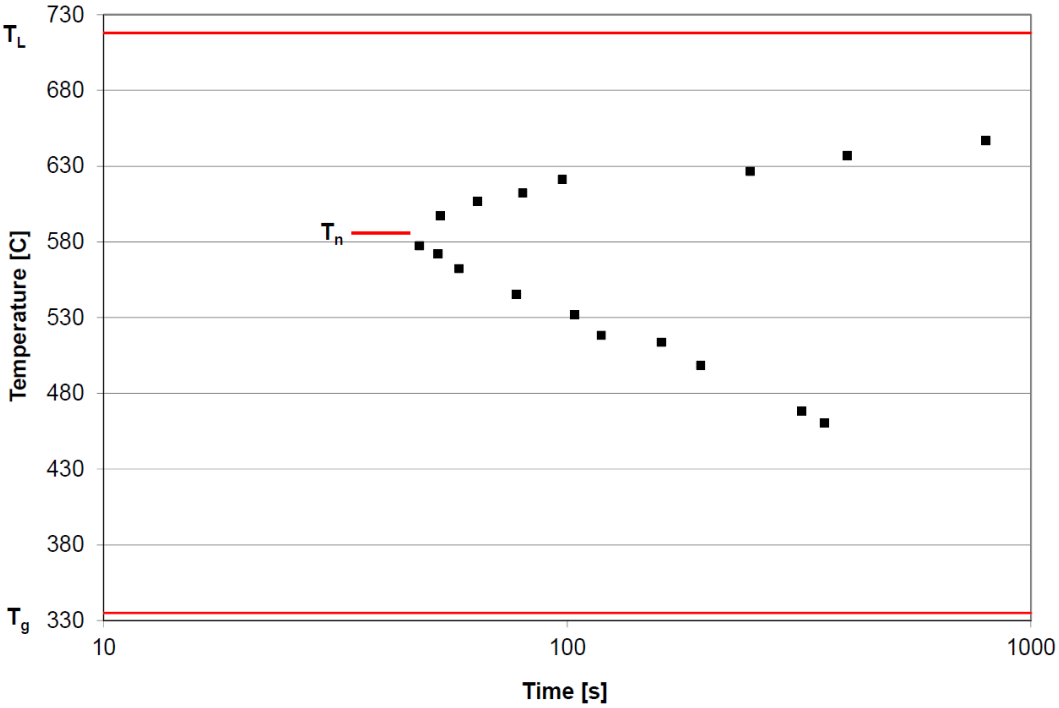

Figure 1.2: TTT diagram for Vitreloy 1 ($Zr_{41.2}Ti_{13.8}Cu_{12.5}Ni_{10}Be_{22.5}$) by cooling in an electrostatic levitator. The red lines denote (from the top) Vitreloy 1's liquidus, nose, and glass transition temperature. The black squares denote the onset of crystallization for a given temperature. Reproduced with permission from Aaron Wiest's thesis[91].

TTT curve, with slower cooling rates resulting in higher nucleation temperatures. Increasing the cooling rate will reduce the nucleation temperature until the critical cooling rate is passed, at which point crystal nucleation is bypassed. In the homogeneous nucleation limit, there is a range of cooling rates that will result in occasional glass formation and occasional crystallization just due to the stochastic nature of nucleation.

TTT diagrams are the most robust way of determining GFA when the approach is possible and practical. Due to the lack of temperature changes in the isothermal holds, spatial heat differentials should be minimized and so the entire sample is reacting to the same thermal conditions. The samples are not subjected to flow, which eliminates strain rate effects and helps keep the sample experiencing homogeneous conditions. However, performing TTT experiments for glass formers in many alloy systems is impossible or very difficult, given the challenges in finding appropriate containers that do not act as heterogenous nucleation sites or in keeping them

stable in ultra high vacuum conditions, and the latter approach requires expensive instrumentation in the form of electrostatic levitators.

1.4 Processing Factors that Affect GFA

It is well known that processing affects a materials GFA, even in container-less ultra high vacuum systems where external factors are minimized. Processing is almost entirely detrimental to intrinsic GFA, though it can help address the effect of impurities. Intrinsic GFA is being used in this case to denote the GFA attainable due to the alloy without any deterimental effects by inpurities or other environmental conditions. By studying the effects of processing on GFA the material can be better understood on a technological and scientific level. The negative aspects of processing with regard to GFA often come in the form of casting, one of the few ways to make rods of metallic glass. Casting introduces the challenges of controlling flow, managing the thermal behavior of the samples, and impure environments. There are two notable processing steps that can improve GFA by reducing the effects of impurities in the material: fluxing and overheating. These processes cannot improve the GFA of the material above its intrinsic, homogeneous nucleation controlled limit, but it can get us close to that value. While there are several intrinsic properties that can affect GFA, those details will be covered in the next chapter.

Overheating is a phenomenon where there exists a temperature far above the liquidus where GFA and mechanical properties markedly improve. In the literature overheating is mostly understood with reference to GFA, but mechanical properties have been noted as being improved as well[100]. A demonstration of this is shown in Fig. 1.3 as shown in Mukherjee *et. al*[59]. In this figure of Vitreloy 105, nucleation temperature is shown as a function of overheating temperature. It is clear that at around 1150°C and 1220°C there is a change in the primary nucleation pathway. While this particular alloy does not form a glass in the electrostatic levitator which this experiment was performed in, we can conclude that this overheating affect increases GFA. By removing the highest temperature nucleation pathway the alloy can cool further, where it will then be nucleated by a different less potent heterogeneous nucleation event, homogeneously nucleate, or form a glass. This improvement has been shown in several zirconium glasses [59][53], zirconium based composites [54], and with the effects of added impurities [50]. The cause of this overheating effect is not fully understood. In the case of Zr-based glasses, it is thought that overheating involves transformation from a eutectic intermetallic phase

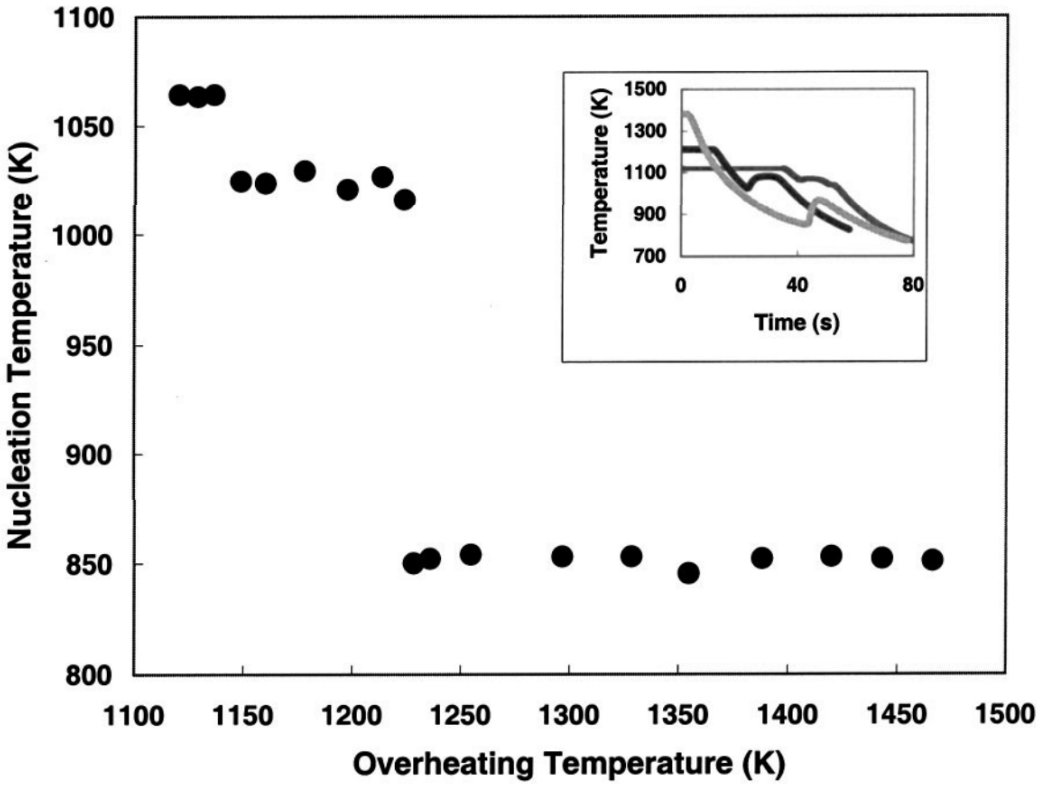

Figure 1.3: Nucleation temperature vs overheating temperature for the metallic glass forming alloy $Zr_{52.5}Cu_{17.9}Ni_{14.6}Al_{10}Ti_5$ (Vitreloy 105). There are two overheating threshold temperatures at 1150K and 1220K. The cooling curves obtained from different levels of overheating are shown in the inset. The temperature rises in the inset are recalescense events showing crystal nucleation in the liquid. Reproduced with permission from Mukherjee *et. al*[59]

to a dissimilar intermetallic phase [86]. Despite the implications for glass forming ability and other properties, overheating effects have not been well documented in other metallic glass systems.

Fluxing is another process to increase glass forming ability and improve mechanical properties. The most common fluxing treatment is heating a molten alloy while in contact with liquid B_2O_3 (to be referred to as boron oxide). This process was discovered in the 80's in a palladium-based glass [46]. Since then fluxing has been applied to numerous systems, including Ni-[62], Pt-[70], Pd-[56] and Fe-based glasses[74]. Boron oxide cannot be used in any system containing a wide variety of elements, notably zirconium, titanium, aluminum, magnesium, or most rare earths. These elements are more favorable oxide formers than boron as can be seen on an

Ellingham diagram and as such would strip the oxygen from the boron. However, it has been shown that alloys containing silicon, an element with marginally more stable oxides than boron, are sometimes helped by fluxing with boron oxide[27]. In those systems the increase in GFA is partially due to the removal of oxygen but likely also partially due to alloying effects of substituting boron for silicon[21].

1.5 Experiment Design

A Netzsch 404C DSC was used to undercool a recently developed Ni-based alloy, $Ni_{71.4}Cr_{5.52}Nb_{3.38}P_{16.67}B_{3.03}$. This alloy was selected for its large GFA (>10mm) and potential commercial interest. Samples were given by Glassimetal Technologies for this project. Processing for this alloy had been previously optimized by Glassimetal Technologies and had been fluxed prior to receiving the alloy. To prevent any heterogeneous nucleation from the container and to prevent any container reaction with flux, a quartz liner was made to fit inside the alumina pans as shown in Fig. 1.4. These liners were made by taking a tube that had a 1mm diameter wall and sealing one end, leaving one end unsealed. Our starting quartz tube had a slightly larger outer diameter than the inner diameter of the alumina pan so the sealed end had to be reduced in diameter to allow for the liner to fit in the pan. In comparison with the idealized schematic in Fig. 1.4 the quartz liner usually was significantly thicker at the bottom and tended to lean in the pan due to size differences between the quartz liner and the pan. The process of sealing one end increases the thickness of the seal significantly compared the wall thickness. The sample was placed in these liners; during the experiments with flux anhydrous boron oxide was added in the liner with the sample. The amount of boron oxide was not weighed or otherwise proportioned, as excess boron oxide was not believed to affect the results. Later work with alloys containing silicon suggest an effect due to chemical substitution, but to date no result has suggested chemical reaction in alloys where all elements have less oxygen affinity than boron[27][28][21]. Care was taken to ensure that the sample, when molten, would be fully submerged in boron oxide but that the level of boron oxide would not allow it to climb over the walls of the liner. About 2 mm^3 of material was placed in the liner. Due to the size of the liner, the sample sits very high in the sample pan. This makes measurements of heat released in recalescence unreliable, but due to the sharp nature of the recalesence event an onset signal could be measured even with samples significantly smaller than the ones used in this experiment, in testing samples smaller than 1mg could still have quite noticeable

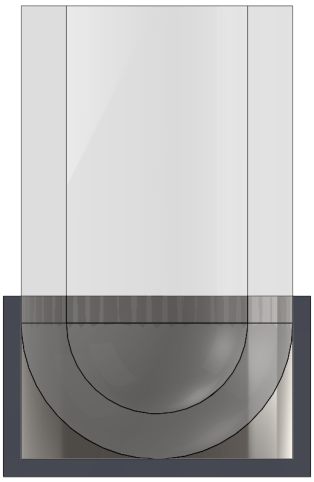

Figure 1.4: Schematic drawing of the sample holder during the undercooling experiments. It is a cross section of alumina sample pan with a quartz liner inside

crystallization events.

During the operation of the DTA a constant flow of 30 ml/min ultra high purity (UHP) argon was sent through the system. The system was pumped down and backfilled with argon three times before each run. The samples were heated and cooled at 20K/min.

Data were first collected by cycling the same sample from 600°C to a temperature far above the liquidus of 866°C. Overheating temperatures between 1150°C and 1350°C, measured at 50°C intervals, were tested. In these experiments individual samples were melted and recrystallized numerous times without removing the sample. The number of cycles was limited by the program that the Netzsch could run. 600°C is significantly above the glass transition in this alloy system, but it is generally also far below the nucleation temperature. This minimum temperature was chosen because upon cooling the boron oxide flux had a tendency to crack the quartz, which posed risks for the sample head of the DSC. Experiments were thus only allowed to cool down to B_2O_3's glass transition temperature of around 300°C at the end of an experiment.

A second set of experiments was performed by heating and undercooling single samples to the target temperature, holding for a set amount of time, and cooling down. These samples were not cycled as the goal was to eliminate any effect of

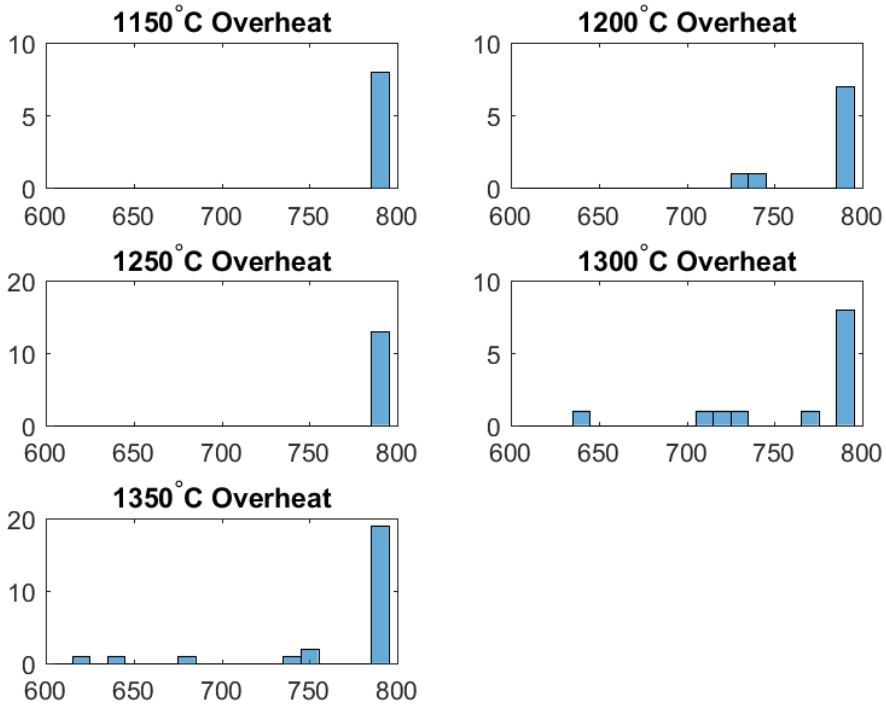

Figure 1.5: Histogram of nucleation temperatures for NCPB 210. The nucleation temperature for several overheating temperatures are plotted as a histogram with 10°C binning. The overheating temperature listed gives the maximum temperature the sample was heated to with no time spent at that temperature for an isothermal hold. The x-axis represents nucleation temperature which gives the onset of initial nucleation.

progressive cleaning of the sample and would allow for analysis of the sample after a measurement if one was particularly promising. As in the first experiment, the overheating temperatures were varied. Additionally, overheating was tested with and without flux, and to see if a hold time at the overheating temperature made a difference.

1.6 Results

Initial tests with cycling the samples in flux provided interesting but largely inconclusive results. The results of these cycles are presented in Fig. 1.5. There is a strong heterogeneous crystal nucleation event that occurs around 790°C at 20°C min^{-1} cooling rates. This nucleation event occurs in the substantial majority of cases. Given a liquidus temperature of 866°C this represents a standard undercool-

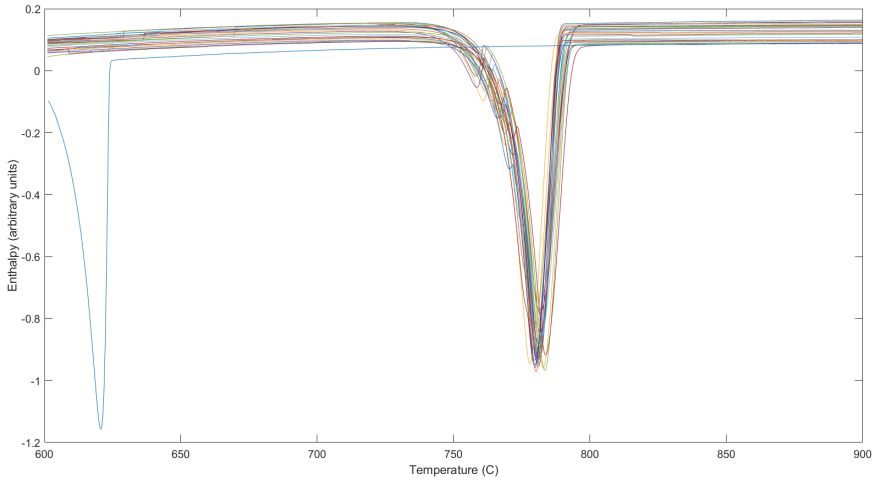

Figure 1.6: Deepest undercooling in NCPB 210. The sample nucleated at 623.8°C, over 160°C below the modal nucleation event.

ing of 76°C. Given that this showed up in the substantial majority of cases, it is likely that this nucleation event is what limits GFA in this alloy, and almost certainly is the limitation when making rods of significantly larger size (such as around its 10mm GFA).

Select cycles demonstrated behavior that was very surprising. While the majority of nucleation events happened close to 790°C, occasional runs would have nucleation events in the low to mid 600°C range, which is expected to be near the nose of the TTT curve for this alloy. An example of this behavior can be seen in Fig. 1.6. This degree of spontaneous undercooling is challenging to account for. Additionally, the lack of thresholding effects[59], where an increase in temperature shows as a discontinuous decrease in the nucleation temperature, indicates that the nucleation mechanism is not as straightforward as in alloys like Vitreloy 105. While there does seem to be an effect of overheating temperature on nucleation temperature, this effect is not consistent between cycles. The lack of any nucleation event below 785°C for 1150°C and 1250°C, with only a relatively small further undercooling at 1200°C, suggests that there these temperatures are not high enough to see an overheating effect, though there is not enough data to make a conclusion with any certainty. 1300°C and 1350°C show a higher proportion of deeper undercooling events as well as some instances of substantially deeper undercooling, again suggesting an overheating effect that begins between 1250°C and 1300°C.

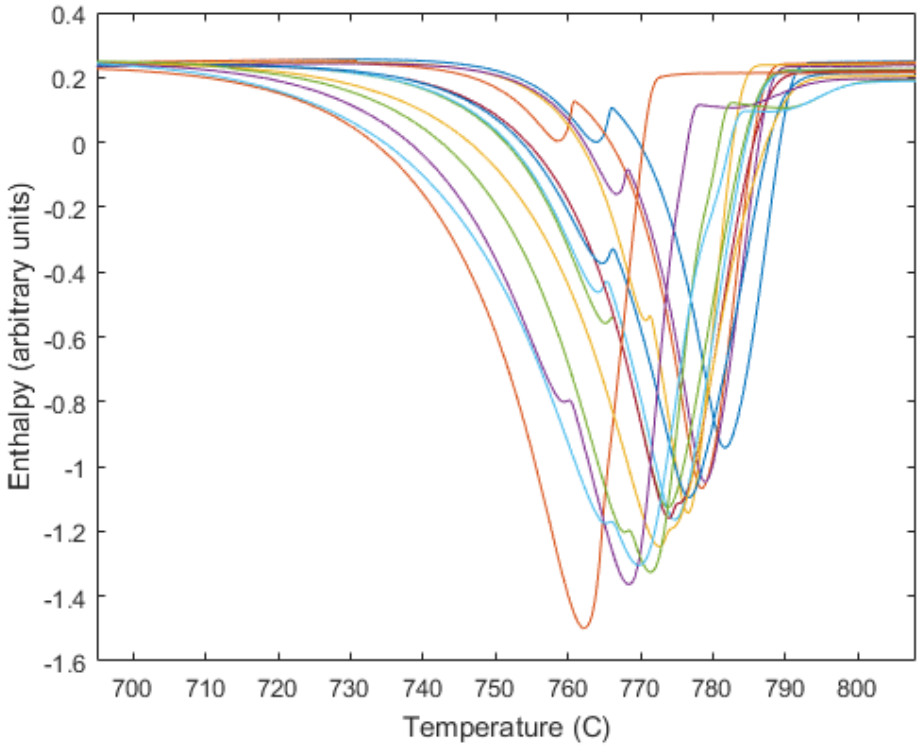

Figure 1.7: A series of cooling runs from the same cycle which shows the transition from having a secondary nucleation event at shallower undercooling to having a single nucleation event at around 770°C

In contrast with works such as Perepezko[92] there was no improvement in undercooling as the number of cycles increased. Indeed, there was no consistency in when these deep undercoolings would occur. The deepest undercooling, 623.8°C, occurred as the last run in a cycle where no other run undercooled below 785°C as shown in Fig. 1.6. The undercooling events at 637.9°C and 679.7°C in the 1350°C overheating runs happened back to back, but were otherwise in cycles where there was no other substantial degree of undercooling and were preceeded and followed by similarly uneventful 790°C nucleation events.

In this nickel alloy there is a primary nucleation event that often starts at 790°C and when that nucleation event occurs there is a secondary nucleation event that happens at around 760°C. When the system is undercooled to where nucleation begins at 770°C the nucleation events seemingly merge into a single event, as shown in Fig. 1.7.

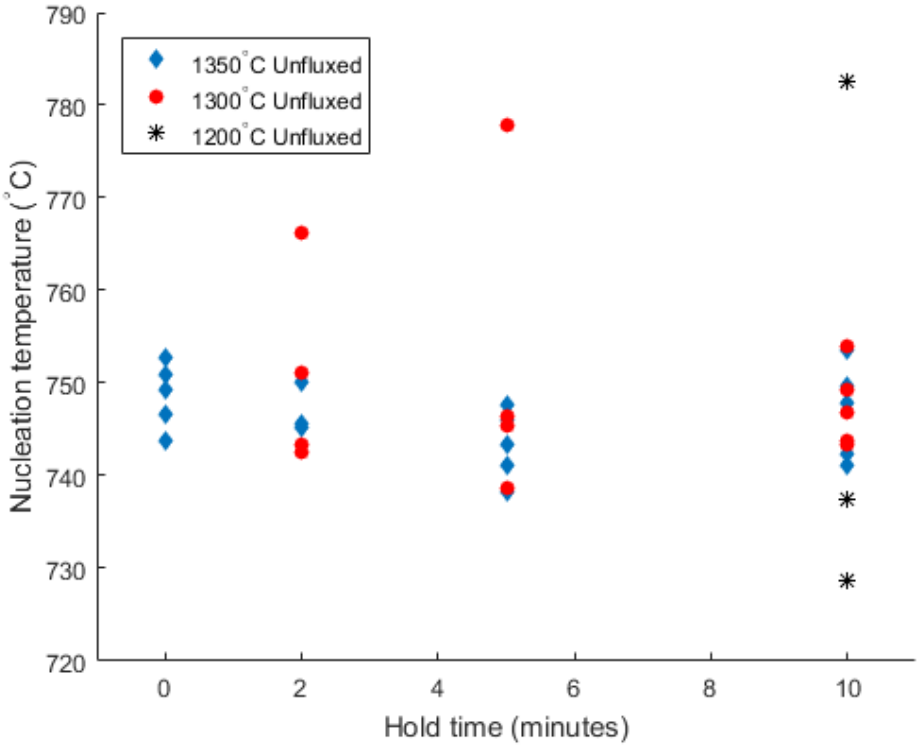

Figure 1.8: Nucleation temperature for unfluxed samples as a function of overheating temperature and hold time. Unfluxed samples were heated to the overheating temperature denoted in the legend, held for a time specified in the x-axis, then cooled at 20°per minute.

Because cycling did not improve undercooling in a consistent way, single runs were undertaken to better isolate the effects of different processing parameters. In addition, to try and disambiguate the effects of overheating from nucleation samples were measured unfluxed at first then flux was done for 1350°C runs. The results from this are shown in Figs. 1.8 and 1.9.

Fig 1.8 shows the effect of overheating at three different temperatures and for varying hold times for unfluxed samples. These hold times, at 0, 2, 5, and 10 minutes, were designed to see if there was an effect of how long the sample was held at the overheating temperature. Longer hold times were not considered safe for the unfluxed samples because of concerns that phosphorus in the alloys would outgas at long hold times, thus changing the composition. There is seemingly no effect due to the hold time at these temperatures, with the seeming improvement for 1300°C at 10 minute holds likely being an artifact of the number of samples run. The samples

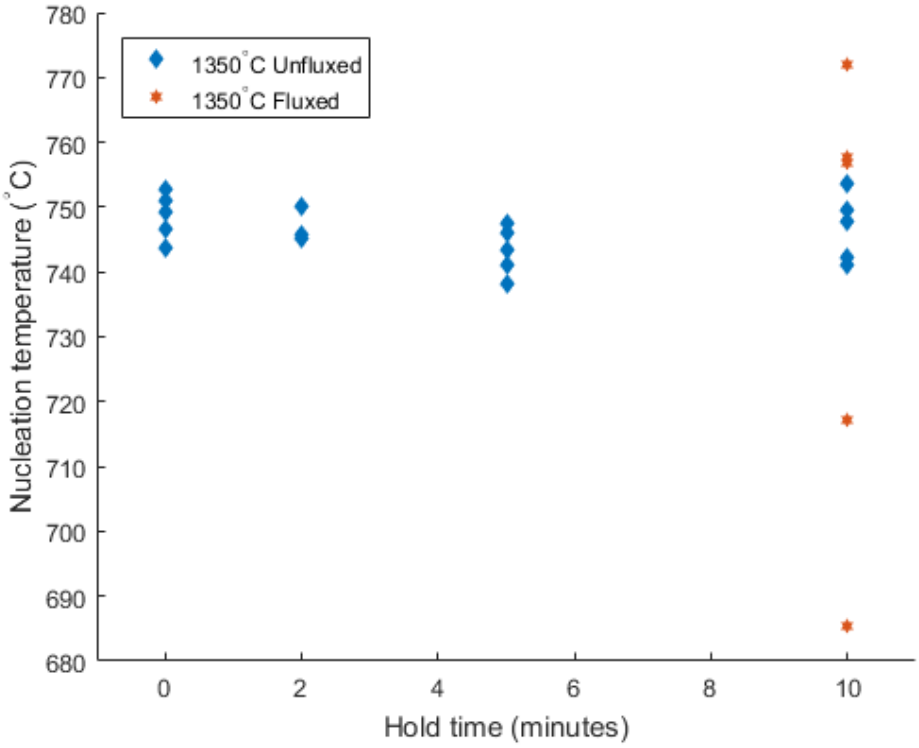

Figure 1.9: Nucleation temperature for samples heated to 1350°C. Fluxed and unfluxed samples were heated to 1350°C, held for a time, then cooled at 20°C per minute.

overheated to 1350°C had a relatively tight spread in their nucleation temperatures that did not change appreciably with hold times. 1200°C samples had significantly higher spread in their nucleation temperatures, but interestingly, included some deeper undercooling than what occurred for higher overheating temperatures.

Fig. 1.9 shows the effect of fluxing at 1350°C and holding for 10 minutes and compares it to unfluxed samples. What becomes readily apparent is that fluxing the alloy introduces a very wide spread in nucleation temperatures, with some samples undercooling far deeper than their unfluxed counterparts and others nucleating at higher temperatures.

1.7 Discussion

The results from these experiments are hard to interpret in light of previous experiments on overheating and fluxing, which had much more straightforward results. Much of this is likely due to the particulars of this alloy and its processing history,

but it presents some interesting ideas for GFA.

Starting from the cycling data, it is clear that the nucleation event at 790°C controls the GFA of the system. It is the nucleation pathway that is expressed in the large majority of cooling runs and given that actual rods of material contain many times the amount of material as these samples it is almost certain that a region of material in a bulk part will nucleate at this temperature. The family of nickel-alloys this system belongs to are strongly controlled by nucleation of crystal phases, once a crystal is formed the growth of that crystal will grow at m s^{-1} rates (from personal discussion, see footnote)[1]. Other glasses, particularly in the Zr-based glasses exhibit much more sluggish behavior[64]. This means that a nucleation event anywhere in the sample will cause the entirety of the sample to crystallize very rapidly.

Once this nucleation pathway is avoided, however, undercooling can continue for a very long time. This can be most dramatically seen in Fig. 1.6. What these very deep undercooling events demonstrate is that the nucleation event at 790°C is heterogeneous nucleation. It is unclear if the there are other heterogeneous nucleation events that need to be avoided, there are not enough runs to get sufficient statistics to make that determination. It looks quite possible that nucleation below 790°C is homogeneous, or at least that any heterogeneous nucleation pathways are not nearly as catalytic for crystal nucleation.

Particularly if the nucleation events in the mid 700°C are heterogeneous, and given the single run unfluxed data that appears to be the case, it suggests an interesting possibility. The nucleation events in the 630°C range should be very near the nose temperature. Given that bypassing the nose is sufficient for making a glass, in these experiments glasses were almost formed, and likely would have if either homogeneous nucleation had not occurred right when it did or if a higher cooling rate was used. This glass would have a GFA at least a factor of two or three higher than the nominal GFA of the alloy, creating the highest GFA Ni-based glass, and would be one of the highest intrinsic GFA metallic glasses in existence. Even if the estimate of the nose temperature is wrong, it is clear that with not too much higher cooling rates a glass could be formed in the DSC.

However, this very high intrinsic GFA seems unlikely to be ever seen in practice. Despite fluxing and overheating, it seems a single heterogeneous nucleation site is

[1] Communication with Prof. William L. Johnson, California Institute of Technology, December 2017

enough to reduce the GFA to the 10mm or so seen in practice, and removing this nucleation site seems to be based more on luck than any processing method tried so far. Because a run with a deep undercooling would most often revert back to nucleating at 790°C in fluxed samples or 750°C in unfluxed samples, successes in removing or dissolving what is likely an oxide particle seem to be transitory successes. These alloys had previously been fluxed, and the fluxing during the creation of the sample did improve its GFA during that step. As such, it is perhaps unsurprising that additional fluxing did not improve nucleation behavior significantly in the modal case, as the large majority of oxide particles would have been already removed and additional fluxing likely provided marginal benefit at that point. Additionally, one large difference between these experiments and creating a large sample is the flux to sample ratio. While the flux should not be chemically interacting with the sample, it has been shown that the ratio of flux to sample can affect the kinetics of processes between the two[21].

The single run samples provide more evidence that the value of fluxing was inconsistent and even possibly detrimental. That fluxing reduced the amount of undercooling in some runs suggests that fluxing can even be detrimental to GFA, even when the material has no elements with more favorable oxide formers than boron. The change in modal nucleation temperature from 790°C in fluxed cycled experiments to 750°C in single unfluxed runs indicates that the presence of flux actually introduces heterogeneous nucleation sites. However, the deep undercooling cycles only occurred in the presence of flux, indicating that fluxing could occasionally remove this nucleating event.

The mechanism by which this happens is unclear. Compared to the unfluxed runs which simply sit in quartz, the boron oxide flux has a much higher contact with the sample and has much higher diffusion than the quartz. There is an equilibrium oxide concentration in the sample and outside the sample in the flux. Boron oxide can reduce the alloy by reacting with metal oxides in the sample or by creating metaborates by reacting with oxygen in the system[27]. Most previous studies on fluxing were not performed on alloys with boron, which the alloy in this work does contain. Given that we could be dealing with a single oxide cluster forming the basis of the nucleation pathway, it is possible that the flux is incapable of further reducing the oxygen concentration in the sample. This is especially possible considering that the alloy contains boron and likely has an equilibrium amount of

boron oxide in the sample. In this hypothesis, on the runs where oxide is removed, it returns to the sample in subsequent cycles, which eliminates the possibility of progressive cleaning of the sample by fluxing. Given that the alloy in this work does contain boron, it is likely that the oxides in the alloy are boron oxide or some metal and boron oxide compound. It is possible that due to this, there is a limit to the ability of flux to reduce the material as the material itself contains oxides that are equally thermodynamically favorable. Another possible explanation for the seeming inability to maintain the high quality material that deeply undercools is that the material is not appreciably cleaner in those runs, but rather that the oxide in the material dissolves upon overheating and fails to recreate the offending heterogeneous nucleation site that run, but reappears the next run in the cycle. While this explanation is not particularly satisfying, the data quality is not high enough to make a meaningful determination of the underlying nucleation pathway.

Overheating seems to help GFA in these alloys, but it is not a clear-cut case. Higher overheating temperatures seemed to be related to increased probability of deep undercooling runs, but without more data that conclusion is tentative. What it did seem to do is improve the consistency of undercooling when heated to 1350°C and the samples were unfluxed. This improvement in consistency may or may not manifest as improved consistency in GFA. Holding times, at least for the relatively short holding times performed in this study, did not seem to have any effect on nucleation.

Performing experiments on emulsions of this alloy would help elucidate some of the nucleation mechanisms in place. Because it seems likely that there are just a few isolated critical heterogeneous nucleation sites, creating a suspension of small isolated particles should allow for a single experiment with a large number of particles to have no heterogeneous nucleation sites. Because the alloy can be fluxed in a separate processing step, the emulsion would not need to be in any particular type of suspension, just one that did not materially contribute heterogeneous nucleation sites. Emulsions have been used successfully to measure the thermodynamic properties of metallic glass alloys[65], and these alloys should be readily processable in DSCs using the emulsion approach given the lack of reactive metals. However, it will likely be difficult to stabilize any emulsion at high temperatures, so understanding the role of overheating is likely to be not possible using an emulsion approach. Given that this alloy has a relatively high liquidus compared to the precious metal

alloys that emulsions have been used on previously, it may not be easy to create emulsions of this alloy.

While this work provided some tantalizing glimpses of some very interesting effects in a commercially relevant alloy, on a scientific front it was too difficult to get solid data on relevant timeframes. Other alloys in the family of Ni-based alloys this was derived from may exhibit cleaner nucleation behavior, and other alloy systems might be better suited to drawing out the relevant underlying mechanisms of fluxing and overheating. Chapter 2 goes into depth on work to better understand the physical mechanisms that underlie GFA, and Chapter 4 presents an alloy system that exhibits very interesting undercooling behavior.

Chapter 2

THE ROLE OF FRAGILITY IN GFA

2.1 Abstract

The role of fragility in GFA is explored in the context of a recently discovered set of bulk glass formers in the Ni-Cr-Nb-P-B system. These glass formers were mapped over a multi-dimensional composition space and were shown to have exponential cusps in GFA as a function of composition. The GFA of these glasses are analyzed with a model that explains the GFA as an interplay between the thermodynamics and kinetics of crystal nucleation, showing high variance in liquid fragility as a function of composition.

2.2 Introduction

The previous chapter explored some of the numerous ways that environment, impurities, and other external factors could affect a glass former's GFA. There are several intrinsic factors that help determine a material's GFA, and considerable work has been done to try and identify the characteristics of good glass formers. Over time there have been several notable characteristics of good glass formers, and these characteristics became heuristics in developing new alloys. The most prominent heuristic is to identify deep eutectics in composition space. The first metallic glass developed was based around the very deep Au-Si eutectic[44] and many of the best metallic glasses are based around deep binary eutectics such as Ni-P, Fe-P, Cu-Zr, Pd-Si, among others. While binary phase diagrams exist for almost all alloys of interest, ternary and higher order phase diagrams are significantly rarer. The experimental efforts to create meaningful ternary or higher dimension diagrams are very substantial, so if experimental analysis is done it is usually to map out areas near compounds of interest. Computational techniques are much more able to tackle these higher dimension composition spaces, but it is still very time consuming to make generalized phase diagrams. As such, the ability to use eutectics as the only design tool is very limited.

Other heuristics, such as negative heats of mixing, large differences in atomic size, and having a high number of different elements (usually up to 4, 5, or even 6 for good

glass formers), are used to help design better glasses formers. These heuristics, while useful, struggle in that they do not have any direct relationship with GFA. This has been one of the motivators to identifying material properties that directly relate with GFA. One of the first and perhaps most notable property proposed was the Turnbull parameter, also called the reduced glass transition temperature, $t_{rg} = \frac{T_g}{T_l}$ which is the ratio of the glass transition temperature to the liquidus temperature. Turnbull hypothesized that a t_{rg} greater than 2/3 would result in glasses that would be easy to form and hence would have a large GFA[84]. Other materials parameters proposed include the width of the supercooled liquid region, ΔT[34], $\frac{T_x}{T_g+T_l}$[57] (where T_x is the crystallization temperature on heating), atomic size and electronegativity differences[95], atomic size and chemical compatibility[30], the liquid fragility m [82][60], and the viscosity at the nose[73]. None of these has satisfactorily explained GFA when looking at a wide selection of glasses.

To understand why these single parameters tend to fail, it is useful to remember that glasses are defined by the lack of an expressed crystallization pathway upon cooling a liquid below its thermodynamic melting temperature. Understanding glass forming ability comes from understanding the nucleation of crystals. The previous chapter touched on classical nucleation theory, but did not cover rates of nucleation. Nucleation rates can be expressed as[62]:

$$\tau_X^{-1} = \nu * exp\left[\frac{-W(T)}{k_B T}\right] exp\left[\frac{-\Delta G(T)}{k_B T}\right] \tag{2.1}$$

τ_X^{-1} is the inverse of the time to crystallization and so expresses a nucleation rate. The prefactor ν is taken to be the atomic vibration frequency. The first exponential, $exp\left[\frac{-W(T)}{k_B T}\right]$, is the rate of atomic rearrangement in the liquid, which is proportional to η^{-1}. The second exponential, $exp\left[\frac{-\Delta G(T)}{k_B T}\right]$, is the probability that a composition fluctuation becomes a critically sized nucleus. Both of these exponentials are thermally activated but are very different mechanisms. The first exponential has a barrier to atomic rearrangement, W(T). As temperature rises, this barrier falls, but does not meaningfully change until passing through the glass transition, at which time the barrier falls more quickly. The rate at which this barrier falls can be expressed by the Angell fragility parameter introduced but not defined in the last paragraph as m. The second barrier is related to the energy barrier discussed in the last chapter. Since one barrier is related to kinetics and one to thermodynamics, it would be expected that no single simple parameter could capture all the effects.

The Angell fragility parameter, henceforth m, is given by:

$$m = \left. \frac{d\log_{10}\eta_{eq}}{d(T_g/T)} \right|_{T=T_g} \tag{2.2}$$

η_{eq} is the equilibrium, Newtonian, viscosity. The Angell fragility is a measure of the steepness of the viscosity versus inverse temperature curve at T_g. The Angell fragility parameter m is not the only measure of liquid fragility, notably in Vogel-Fulcher-Tammann (VFT) models of viscosity there is another definition of liquid fragility, given by the letter D, but m has the advantage of being model independent and works well when comparing glasses with different T_g. When using the Cooperative Shear Model, the viscosity model most often used in this text, the Angell fragility can be related to the VFT D via[42]:

$$m = \frac{DT_0T_g}{\ln(10)(T_g - T_0)^2} \tag{2.3}$$

where T_0 is a fitting parameter in the VFT equation and T_g is determined by 10^{12}Pa·s and not the calorimetric T_g. While calorimetric and kinetic T_g are often close, there can be substantial variation between them. Because fragility relates to viscosity most directly, the kinetic T_g is used. Fragile glasses have steep changes in viscosity as a function of temperature near the glass transition and have a high m, where strong glasses have more Arrhenius behavior and have a lower m. Examples of a fragile glass would be o-terphenyl with $m = 81$, and a strong glass is often given by SiO_2 with $m = 20$[8].

2.3 Simple GFA Model

Starting from Eq 2.1 and noting that the crystallization time takes the form of the TTT curve, by definition the minimum of the function happens at the nose temperature, T*. Assuming that time to nucleation is a well-behaved function of composition, a Taylor series can be expanded around an initial composition c_0:

$$\tau_x^*(c) - \tau_x^*(c_0) \approx \exp[\lambda_x \cdot (c - c_0)] \tag{2.4}$$

with

$$\lambda_x = \nabla[\frac{W(T^*, c) + \Delta G(T^*, c)}{kT^*}] \tag{2.5}$$

These equations predict that for a given crystallization pathway small deviations around a composition result in an exponential dependence of τ with respect to composition. Given that in the Fourier heat flow equation τ is proportional to the square of the lateral dimension, by mapping the square of the GFA we can map out the time to crystallization as a function of composition. In Fig. 2.1 we can see that composition does map to piecewise continuous exponential curves. The peak of the curves correspond to a crossover from one nucleation pathway to another, and it is this competition between nucleation pathways that allows for the cusps to exist.

The $W(T^*, c)$ and $\Delta G(T^*, c)$ terms are the drivers of the exponential curves. The first term as noted earlier can be related to the Angell fragility parameter, m. The second term, related to the thermodynamics of the undercooled liquid, is harder to determine. In classical nucleation theory, presented very briefly in Chapter 1, this term has a bulk value due to free energy differences between the liquid and crystal as well as an interfacial term. These terms are non-trivial to determine and are not readily experimentally available. By assuming that T_g and the Kauzmann temperature can be roughly equated, the Gibbs Free Energy term can be approximated to lowest order as $\Delta G \propto (1 - t_{rg})^{-2}$[62]. Despite the somewhat heroic assumptions involved in getting to this expression it has some value. The reduced glass transition temperature is a very readily determined experimental parameter and has been recognized to be correlated with glass forming ability.

This simple model predicts that glass forming ability is a function of of two readily measurable experimental parameters, m and t_{rg} and that the square of the GFA has an exponential dependence on composition. To understand how m and t_{rg} interact, the λ in Eqs 2.4 and 2.5 can be looked at. A λ is defined for a particular nucleation pathyway, with the cusp representing a transition from one pathway to another. The slope difference at the cusp can be given by λ_β - λ_α, where λ_β and λ_α represent the lambdas for the two nucleation pathways. It can be shown that the two factors can be separated without losing any generality into constituent contributions by m and t_{rg}[62]. Thus:

$$\lambda_p = \lambda_m - \lambda_{t_{rg}} \tag{2.6}$$

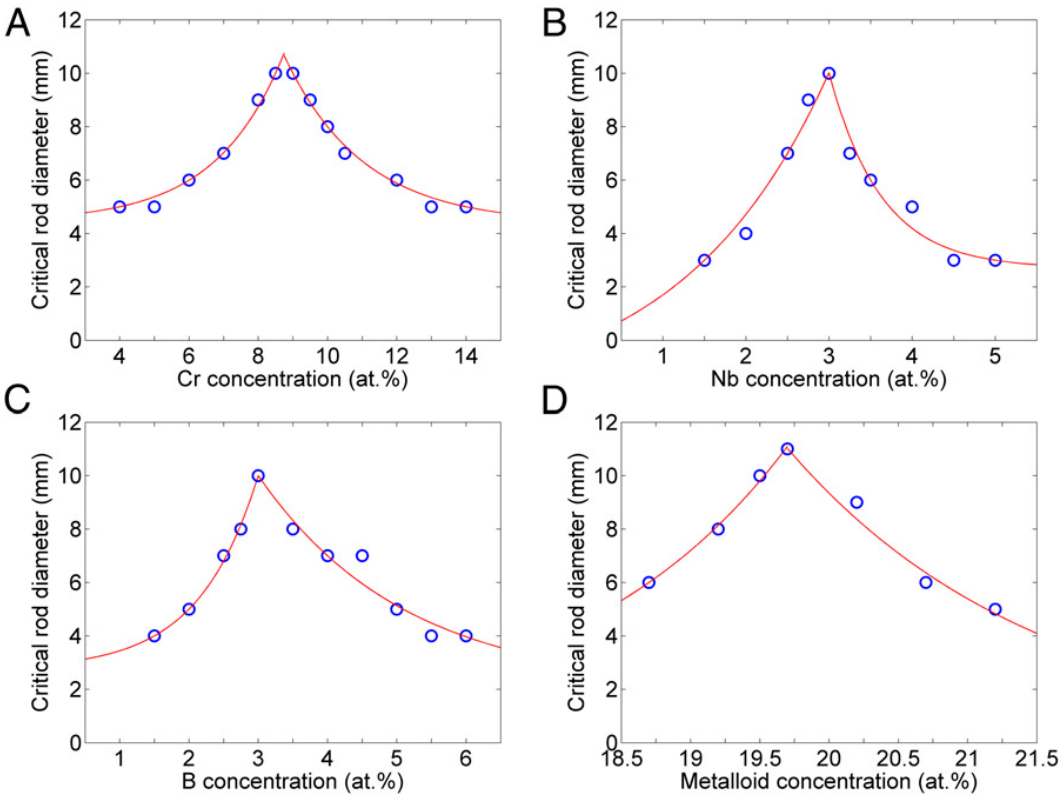

Figure 2.1: Compositional dependence of GFA along four series intersecting a GFA peak at composition $Ni_{69}Cr_{8.5}Nb_3P_{16.5}B_3$. Samples were processed in a quartz tube and were quenched in water. More information on the processing can be found in the paper[62].Solid lines are exponential fits to the experimental data (open circles) on each side of the peak. (A) Critical rod diameter d_{cr} plotted against the Cr atomic concentration as a substitute for Ni according to $Ni_{77.5-w}Cr_wNb_3P_{16.5}B_3$. (B) Critical rod diameter d_{cr} plotted against the Nb atomic concentration as a substitute for Cr according to $Ni_{69}Cr_{11.5-x}Nb_xP_{16.5}B_3$. (C) Critical rod diameter d_{cr} plotted against the B atomic concentration as a substitute for P according to $Ni_{69}Cr_{8.5}Nb_3P_{19.5-z}B_z$. (D) Critical rod diameter d_{cr} plotted against the atomic concentration of metalloids substituting for metals according to $(Ni_{0.8541}Cr_{0.1085}Nb_{0.0374})_{100-(y+z)}(P_{0.8376}B_{0.1624})_{(y+z)}$.

for any arbitrary nucleation pathway p. λ_m is given by:

$$\lambda_m = \frac{d(\ln(d_{cr}^2))}{dm}\frac{dm}{dc} \tag{2.7}$$

and similarly for $\lambda_{t_{rg}}$:

$$\lambda_{t_{rg}} = \frac{d(\ln(d_{cr}^2))}{dt_{rg}}\frac{dt_{rg}}{dc} \tag{2.8}$$

By mapping out the GFA, t_{rg} and m as a function of composition, this model predicts that two of those variables can predict the third. Since m is a property of the liquid and t_{rg} depends on the crystal, m should be a continuous, and likely differentiable, function of composition while t_{rg} should have a discontinuity in its first derivative at the eutectic composition.

2.4 GFA of a Family of Nickel-based Alloys

Na *et al.*[62] developed a series of alloys in the Ni-Cr-Nb-P-B system that allowed for a systematic study of GFA to be undertaken. These alloys were processed in quartz tubes and quenched in water, which largely eliminated shear flow and convective heat flow, making these results more consistent and standardized. Quartz did not materially react with the alloys and would have significant difficulty acting as a nucleation site due to its amorphous nature, further reducing environmental effects from the data.

In one composition dimension the GFA exists as piecewise continuous exponential curves meeting in a cusp as can be seen in Fig. 2.1. These one dimensional cusps turn into ridge peaks in two dimensions, as seen in Fig. 2.2. GFA was mapped in four series of alloys by moving along one dimension in composition space centered at a GFA peak of $Ni_{69}Cr_{8.5}Nb_3P_{16.5}B_3$. These given by (Series I) $Ni_{77.5-w}Cr_wNb_3P_{16.5}B_3$, (Series II) $Ni_{69}Cr_{11.5-x}Nb_xP_{16.5}B_3$, (Series III) $Ni_{69}Cr_{8.5}Nb_3P_{19.5-z}B_z$, (Series IV) $Ni_{0.8541}Cr_{0.1085}Nb_{0.0374})_{100-(y+z)}(P_{0.8376}B_{0.1624})_{(y+z)}$.

2.5 Fragility of Selected Nickel-based Alloys

The fragility of several of the nickel-based alloys was measured. Alloys were selected from each of Series I, III, and IV, with all series being measured from the hypereutectic side and one series (Series III) from the hypoeutectic side. Series II was attempted with both hypereutectic and hypoeutectic compositions but measuring

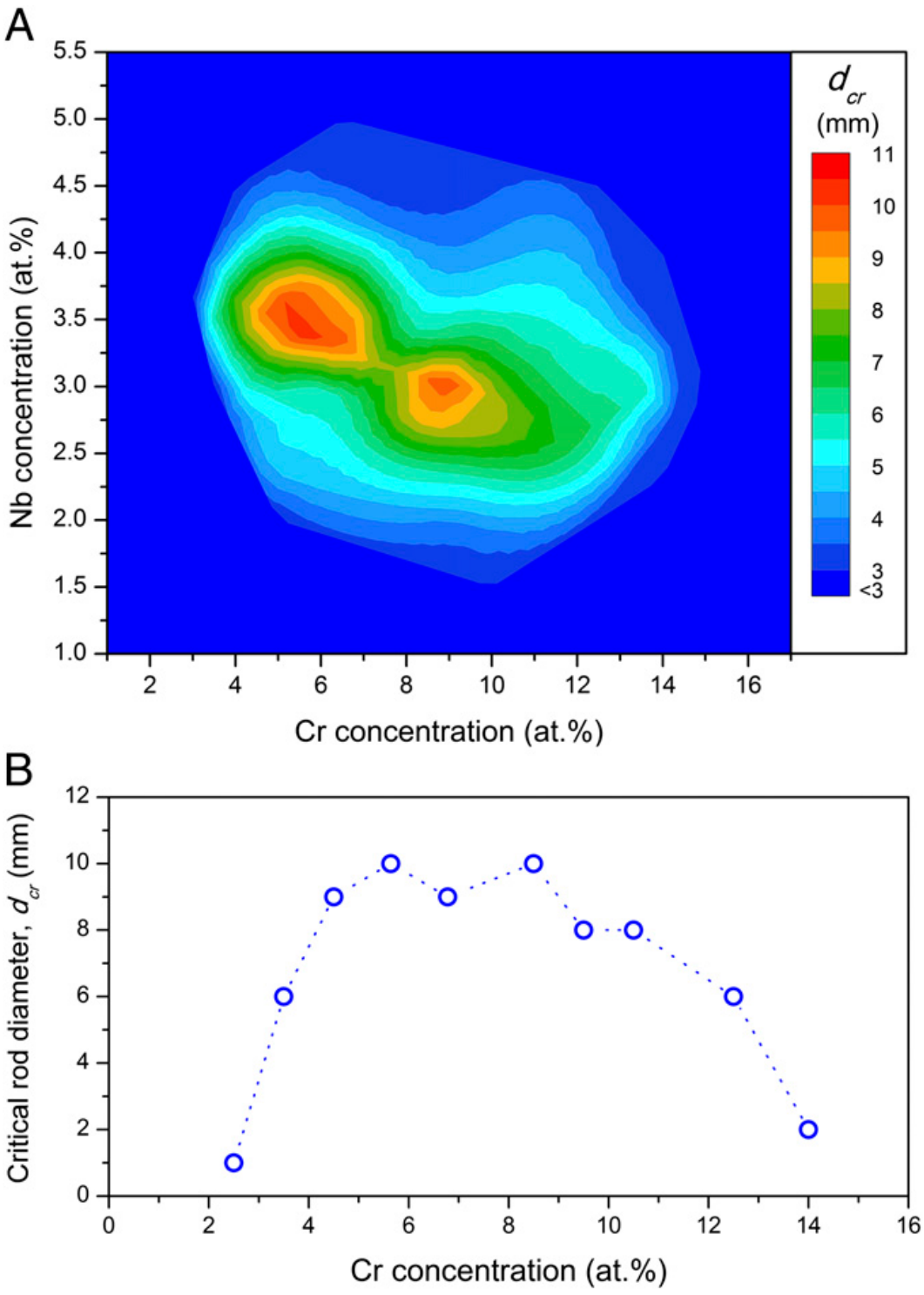

Figure 2.2: (A) Two-dimensional GFA contour map for $Ni_{80.5-w-x}Cr_wNb_xP_{16.5}B_3$ alloys plotting the critical rod diameter d_{cr} against the Cr and Nb atomic concentrations w and x, while keeping the P and B atomic concentrations y and z constant at 16.5% and 3%, respectively. (B) One-dimensional GFA plot for $Ni_{77.4375-0.875w}Cr_wNb_{4.0625-0.125w}P_{16.5}B_3$ alloys plotting the critical rod diameter d_{cr} against the Cr atomic concentration w along the compositional line x = 4.0625 - 0.125w associated with the GFA ridge in the w-x domain shown in A. The dotted line is a trend line through the experimental data given by open circles.

m was limited by too quickly declining ΔT on the sides of the eutectic. In measuring viscosity, crystallization would start before equilibration would occur. In general, ΔT was marginal for these alloys, and so only a small number of alloys could have their viscosity measured accurately.

Fragility was measured using a three point beam bending technique[31] and fitting the data with the cooperative shear model [15]. Rods of amorphous alloy 2mm in diameter and 10mm in length were bent in a Perkin Elmer TMA 7 thermomechanical analyzer. The beam rests on two quartz knife edges 10 mm apart and a quartz rod with a knife edge applies a load in the middle of the rod. A constant force of between 20 mN and 1000mN depending on the set temperature was applied and then a furnace brought the samples to temperature. Due to the nucleation behavior of these alloys, samples could be measured in air and no shielding gas was necessary. Once the samples reach equilibrium, which can take several hours near T_g, a constant deflection of the rod is attained. With that deflection the equilibrium viscosity can be calculated by the following equation:

$$\eta = -\frac{gL^3}{144 I_c \nu}\left(M + \frac{5\rho AL}{8}\right) \tag{2.9}$$

where η is the equilibrium viscosity in Pa·s, g is the gravitational constant 9.8 m s^{-2}, L is the support span length of .01 m, I_c is the cross sectional moment of inertia for the beam in m^4, ν is the equilibrium velocity in m s^{-1}, M is the applied load in kg, ρ is the density (for these alloys, all were very near 8000 kg m^3), and A is the cross sectional area in m^2.

Once the viscosities have been measured for a range of temperatures for an alloy the data are fit to the cooperative shear model[15]:

$$\eta(T) = \eta_\infty \exp\left\{\frac{W_g}{k_B T}\exp\left[2n\left(1 - \frac{T}{T_{go}}\right)\right]\right\} \tag{2.10}$$

with η_∞ being the high temperature limit of viscosity, which for all alloys is assumed to be $4x10^{-5}$ Pa·s[52], W_g is the activation energy barrier at the glass transition, approximated by $W_g \approx k_B T_{go} \log(\eta_g/\eta_\infty)$, where $\eta_g \equiv 1x10^12$ Pa·s, n is the effective fragility parameter, k_B the Boltzmann constant, T temperature, and T_{go} the glass transition temperature associated with a viscosity value of $1x10^{12}$ Pa·s. The fragility parameter m is related to n via:

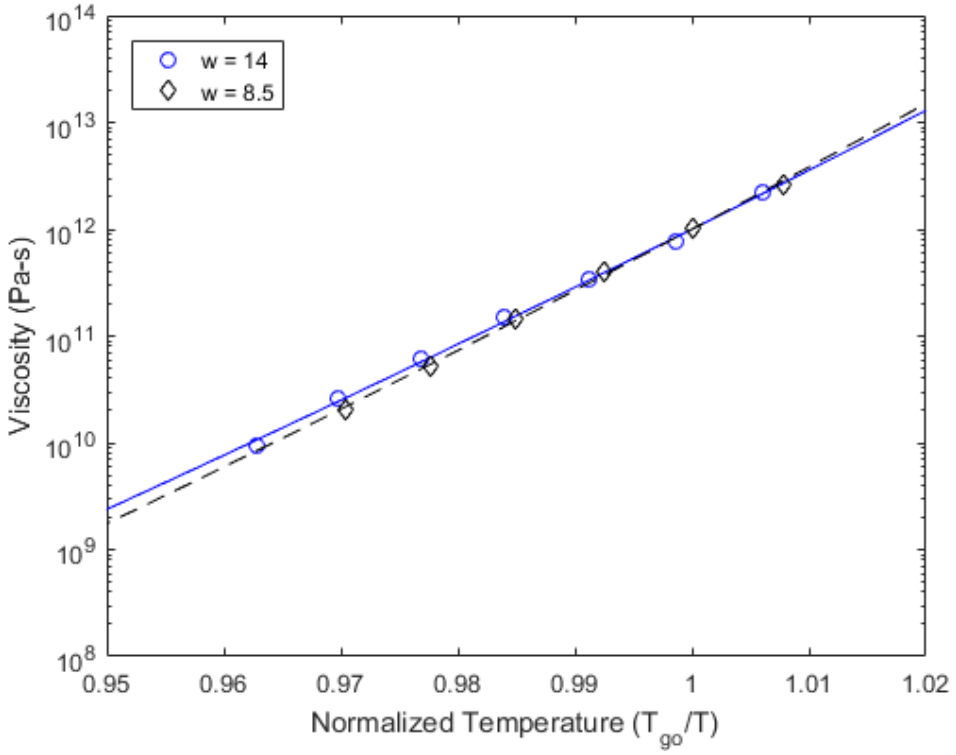

Figure 2.3: Data and fitting curves for the equilibrium viscosity of (series I) $Ni_{77.5-w}Cr_wNb_3P_{16.5}B_3$ metallic glass alloys with w = 8.5 and 14. w = 8.5 has an m of 57.7 and w = 14 has an m of 54.7.

$$m = (1 + 2n)\log(\eta_g/\eta_\infty) \tag{2.11}$$

The cooperative shear model was chosen for its better fit to viscosity data[41] and for the direct connection between fitting parameters and m. However, because the data is based around T_g and m is defined by the slope of the curve at T_g, model selection does not materially affect the values for fragility. Even within the model changing the high temperature limit assumption does not change much. By changing the high temperature limit assumption from $4x10^{-5}$ Pa·s to $1x10^{-6}$ Pa·s or $1x10^{-3}$ Pa·s changes m by less than .3 in either direction, which is well within the experimental error of the underlying viscosity data. For the m to change so little with η_∞ changing orders of magnitude, the n is necessarily changing appreciably, making comparisons with n from other works much less significant.

Results of the beam bending experiments are captured in Figs. 2.3 2.4 and 2.5 for

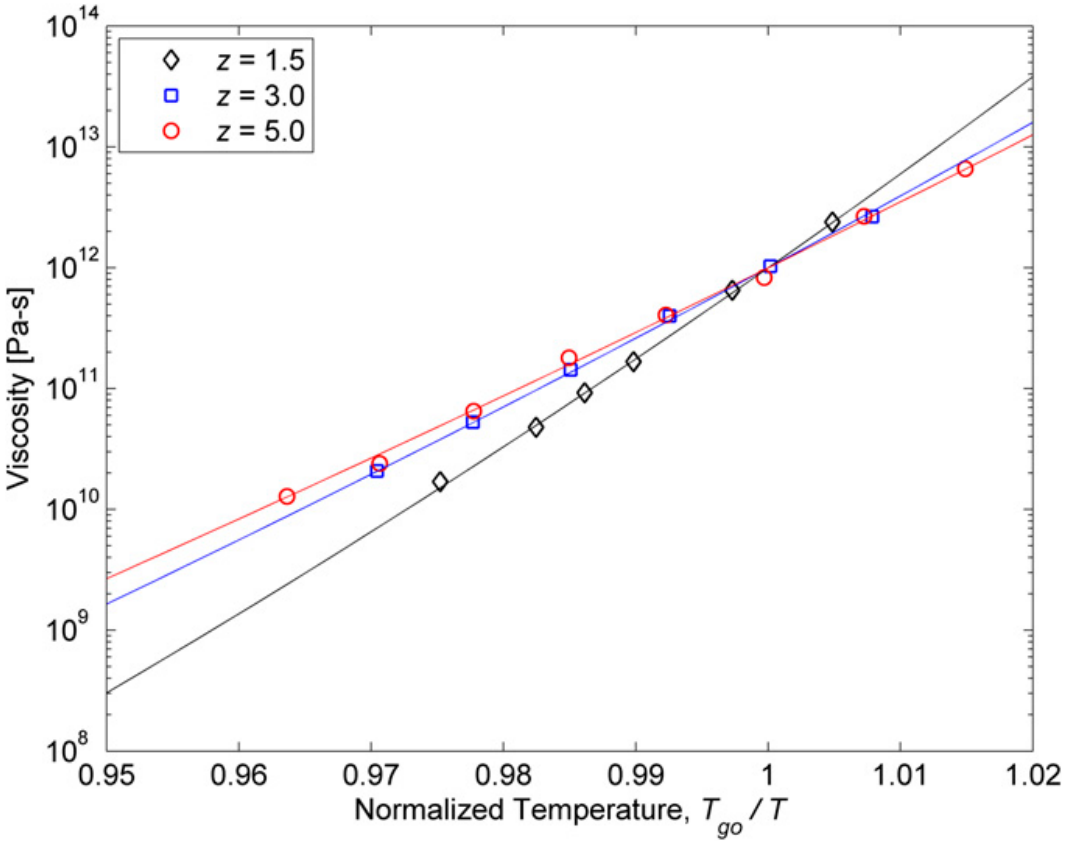

Figure 2.4: Data and fitting curves for the equilibrium viscosity of (series III) $Ni_{69}Cr_{8.5}Nb_3P_{19.5-z}B_z$ metallic glass alloys with z = 1.5, 3, and 5. z = 1.5 has an m of 76.5, z = 3 has an m of 57.7 and z = 5 has an m of 54.0.

each of the respective three series measured. It can be seen that for hypereutectic compositions the alloys are slightly stronger than the eutectic composition, with the smallest strengthening in Series IV, larger in Series I, and the largest increase strength (decrease in m) occurring in Series III. This can be somewhat explained by noting that these were not equal steps in composition space; there was a large increase (5.5 atomic percent) in chromium content between the two data points while the metalloid increase was much smaller (.5). The boron content showed the largest increase in m for a given composition change, but the strengthening of the liquid on the hypereutectic side was not particularly notable, at least with the granularity of the data at hand.

What is particularly interesting and striking is looking at the $B_{1.5}$ hypoeutectic measurement. This alloy is very fragile, with m increasing by nearly 18 for a 1.5 atomic percent decrease in the boron content. This change in fragility has not been seen for

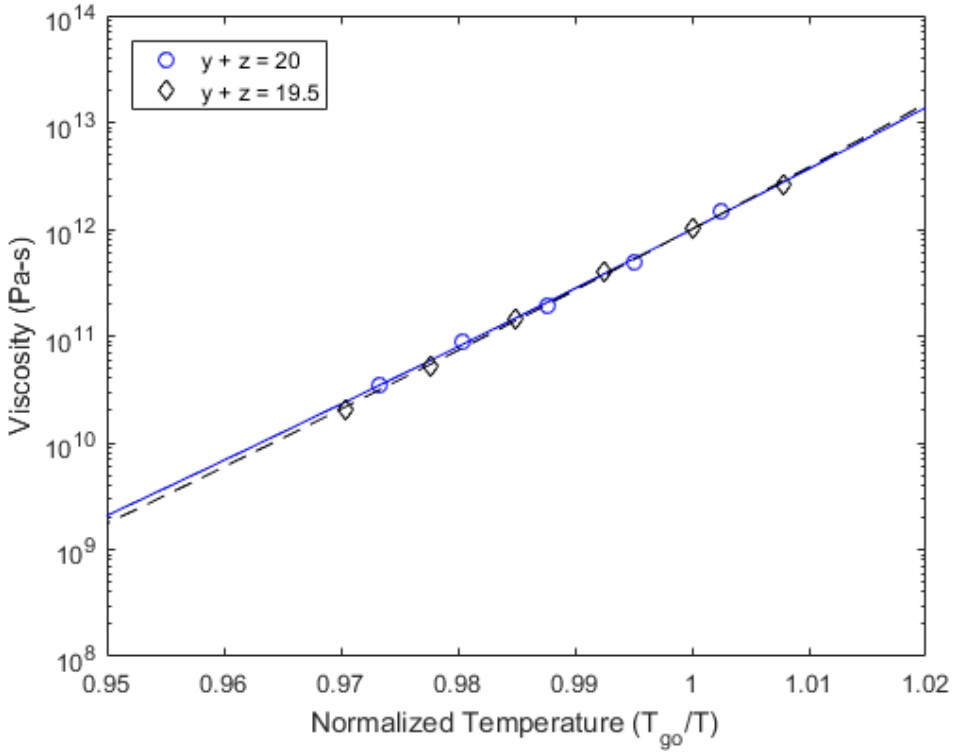

Figure 2.5: Data and fitting curves for the equilibrium viscosity of (series IV) $Ni_{0.8541}Cr_{0.1085}Nb_{0.0374})_{100-(y+z)}(P_{0.8376}B_{0.1624})_{(y+z)}$ metallic glass alloys with y+z = 19.5 and 20. y+z= 19.5 has an m of 57.7 and y+z = 20 has an m of 56.0.

such a small composition change in any metallic glass system.[66] One challenge has been that many alloys have fragility measured using calorimetric techniques, which is an indirect way of measuring fragility and relies on the VFT equations to get the relationship between heating rate and fragility. Using calorimetric technqiues, large differences can be seen with small composition changes in recent work[99] due to minor additions of Ni, but given the large variation between the two techniques[66] large caution should be given to comparing those results. The six viscosity points along the curve near T_g give some degree of confidence that the fragility difference is valid and is not due to any random error in measuring viscosity using beam bending.

2.6 Model Interpretation

The model described earlier predicts that m and t_{rg} solely define GFA. While fragility measurements were limited, they do allow for an analysis of how these parameters would work together to contribute to GFA. Especially given the wealth of GFA

and t_{rg} data even a handful of fragility measurements would allow the model to be checked. The interplay between m and t_{rg} can be best and most easily seen in Fig 2.6.

On the hypoeutectic side, the t_{rg} is mostly flat with some rising. Given the dramatic increase in d_{cr}^2, the marginal improvement in t_{rg} is not explanatory. The dramatic strengthening of the alloy between 1.5 and 3% boron, however, could account for the rapid rise in GFA with increasing boron content. As the liquid becomes stronger, the viscosity at the nose rises and the rate at which new atomic configurations are sampled slows down. This would increase the time necessary to achieve a critically sized nucleus for crystal formation. At ~3% B, there is a cusp and then on the hypereutectic side GFA declines almost as steeply as it rose. The fragility has strengthened some, which on its own would lead to a rise in GFA, but the rapidly declining t_{rg} overwhelms the strengthening liquid and causes the GFA to decline.

The function used to fit the GFA curves in Fig. 2.6 is:

$$d_{cr}^2 = a\exp(bc) \tag{2.12}$$

With c being the composition variable (in atomic units of z), and coefficients a and b being 1.31 and 1.43 on the hypoeutectic side and 800 and -.693 on the hypereutectic side.

Using Eq. 2.4, the hypoeutectic λ (henceforth λ_α, where α will refer to the hypoeutectic region) can be calculated to be 1.43 and the hypereutectic lambda (λ_β with β referring to the hypereutectic region) is -.693. The higher absolute value on the hypoeutectic side is due to the steeper rise of GFA as a function of GFA than the decline on the hypereutectic side.

With Eqs. 2.6 and 2.8 and the fits in Fig. 2.6 we can calculate the remaining variable λ_m. At the cusp composition, we get λ_α = 1.43, λ_β = -.693, $dt_{rg,\alpha}/dc$ = .00211, and $dt_{rg,\beta}/dc$ = -.0213. This results in λ_m = 1.24 and $d(\ln d_{cr}^2)/dt_{rg}$ = 90.6. This gives the $\lambda_{t_{rg}}$ for each pathway as $\lambda_{t_{rg,\alpha}}$ = .191 and $\lambda_{t_{rg,\beta}}$ = 1.93.

2.7 Discussion

Later work has validated the idea that fragility and t_{rg} solely contributed to GFA. Johnson *et al.*[42] showed that a bilinear model with those two terms explained 98% of variation in glass forming ability across many different metallic glass systems,

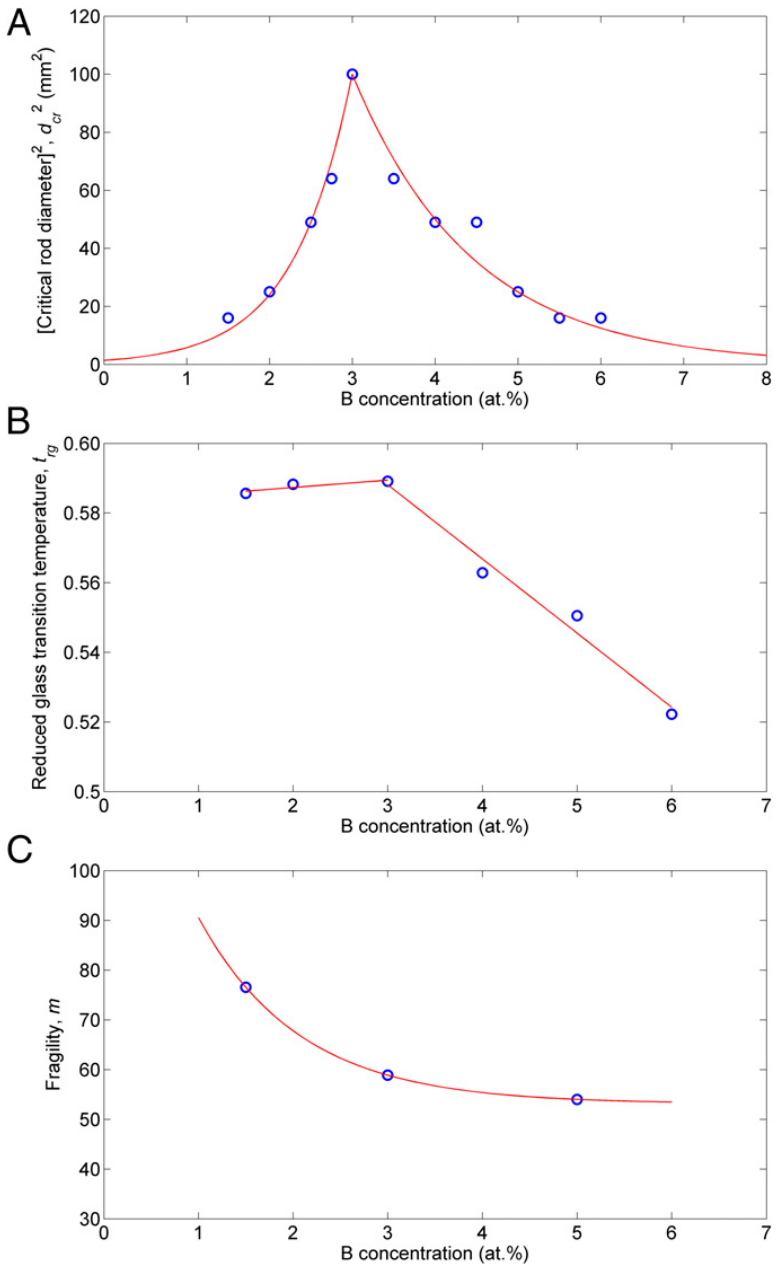

Figure 2.6: (A) Compositional dependence of GFA for $Ni_{69}Cr_{8.5}Nb_3P_{19.5-z}B_z$ plotted in terms of d_{cr}^2 against the B atomic concentration as a substitute for P. Solid lines are exponential fits to the experimental data (open circles) on each side of the peak (at 3 at. % B). (B) Reduced glass transition temperature t_{rg} plotted against the B atomic concentration as a substitute for P according to $Ni_{69}Cr_{8.5}Nb_3P_{19.5-z}B_z$. Solid lines are polynomial fits to the experimental data (open circles) on each side of the cusp (at 3 at.% B). (C) Liquid fragility m plotted against the B atomic concentration as a substitute for P according to $Ni_{69}Cr_{8.5}Nb_3P_{19.5-z}B_z$. The solid line is an exponential fit to the experimental data (open circles).

with every well characterized glass being included in this analysis. The residual error in the model is less than the experimental error, meaning that within measurement error the GFA of metallic glasses can be solely described by these two experimental parameters. There are some very interesting conclusions and practical considerations that can be drawn from this.

Alloy development could see some significant changes due to these results, particularly for large GFA alloys. One challenge in determining GFA of alloys with large GFA is that it takes significant amounts of material and more specialized equipment to adequately make a sample, and this poses a challenge for most lab-scale casting setups. Casting large GFA precious metal glasses becomes prohibitively expensive. Without casting an alloy, the best way to determine GFA is through construction of a TTT diagram. Reducing heterogeneous nucleation can be impossible in some circumstances. For non-reactive metals, quenching a small amount of material in a quartz tube to a target temperature above T_g and waiting for the recalescence event is perhaps the most productive way to generate a TTT diagram. This can be performed either using visual cues of crystallization or using thermal measurements, as with a DSC, though unless a ultra-fast calorimeter is used the timescales of cooling in DSC may be prohibitively slow. For reactive metals, unless there is a container that will not heterogeneously nucleate a crystal phase, containerless methods like electrostatic levitation (ESL) are the only hope to construct a TTT diagram. Due to these limitations, the GFA of even well studied and commercially interesting systems like Vitreloy 1 have not seen any local composition neighborhoods explored with regards to GFA except in a qualitative sense.

Instead of determining GFA of these alloys, the t_{rg} and m of the alloys could be measured, defining what GFA the alloy is capable of. Large GFA alloys tend to be fairly strong glass formers, which should make determining m a bit easier. The t_{rg} of these alloys would be quite easy to measure given that the challenging part is determining the kinetic T_g, as T_L can easily be determined from a DSC scan. This allows for GFA mapping and alloy development using significantly less material and with equipment that is much more readily available. There is still the large challenge of ensuring that good fragility measurements can be taken, with many metallic glasses having insufficient ΔT to equilibrate the liquid near T_g before crystallization. Additionally, measuring fragility takes several days, as near T_g the time to equilibration is often fairly long. Nonetheless, many interesting systems such

as Vitreloy have quite high ΔT, allowing for fragility measurements to be taken, and cannot realistically have the GFA measured in other way besides ESL, which is a very rare and expensive piece of equipment.

Less interesting to most researchers and slightly less necessary, but there are also cases where very low GFA alloys could have their GFA determined better by using t_{rg} and m than current methods. The challenge with determining the GFA of poor glass formers is that most methods of determining GFA require high strain rates, which has been shown to crystallize some metallic glasses (see Chapter 4 and Lohwongwatana *et al.*[55], the latter of whom showed over a two orders of magnitude decrease in GFA by splat quenching compared to quenching a rod of material). Unless the material can be processed in quartz and be cast into a capillary, the methods of determining GFA in poor glass formers has generally been through splat quenching or melt spinning, both of which are limited in how large a sample can be made. As shown by Chen and Turnbull[13], fragility can measured using creep tests on metallic glass ribbons, even for glasses that generally would be considered to have a too low ΔT to measure fragility. By using t_{rg} and m a true intrinsic GFA of poor glass formers can be found. This has less significance for practical applications as manufacturing would likely still require the use of melt spinning, but determining more appropriate GFA could be useful for better determining the utility of different alloys for additive manufacturing.

The interfacial energy difference between a solid and liquid does not appear explicitly in this model, which is very surprising. It is possible that the interfacial free energy is solely determined by t_{rg} and m, though crystal structure, liquid composition, and temperature vary considerably and do not immediately seem to be connected to t_{rg} or m. If there is a timescale to nucleation that controls the process, that could conceivably explain this phenomena. This is especially true if in multicomponent systems the energy cost of chemical fluctuations dominates any interfacial and topological terms[9]. More recent work on the role of composition fluctuations in multicomponent liquids has stressed their importance in crystal nucleation[16][94].

Another surprising element of this research is that heterogeneous nucleation cannot be an important factor for these expressions to work. Within the context of a single alloy system a common heterogeneous nucleation event could be consistent with GFA's dependence on t_{rg} and m, but across a wide variety of alloy systems it would not be possible. The fact that heterogeneous nucleation is not important is testament

to decades of improving the processing of metallic glasses, as these alloys would have needed to use a combination of overheating, fluxing, high purity starting materials, relatively quiescent casting procedures (or using alloys where casting procedures did not affect results), and non-crystalline or containerless processing. In this context, this relationship between GFA, t_{rg}, and m is an indication of limiting behavior. For a given set of values for t_{rg} and m, a maximum GFA for that composition can be calculated, and further improvements in GFA are not possible without composition changes.

This conclusion is surprising given the results in the previous chapter. The alloy measured was a Nickel-based alloy with results consistent with the conclusion in Johnson *et al.*[42]. If the intrinsic GFA of that alloy could be improved by a factor of two or three due to processing improvements, as suggested was possible by the occasional dramatic decrease in undercooling, it would present a challenge in reconciling those results with the ones in this chapter. The alloy in Chapter 1 is in an alloy system with very fast crystal growth kinetics and will completely crystallize with a single nucleation event in the temperatures in question. One possibility is that fluxing the alloy can cause small composition changes, as noted in the conclusion to Chapter 1. While composition changes due to fluxing have not been noted for systems without silicon or other elements with lesser affinities for oxygen[21], it could explain both chapters reasonably well. The Series III alloys had no noticeable change in solidus or liquidus on the hypoeutectic side of the cusp (see Fig. S2 of the supplementary materials of [62]). While the composition in the previous chapter is not one of the series of alloys measured here, a similar effect could be occurring. If $Ni_{71.4}Cr_{5.52}Nb_{3.38}P_{16.67}B_{3.03}$ is slightly hypoeutectic initially with regard to boron content, then fluxing the alloy could be moving the composition closer to the cusp in GFA. These occasional deep undercoolings could then be explained by a changing composition of the liquid due to being cycled in flux repeatedly. In the experiments in Chapter 1 the liquidus and solidus were monitored to ensure that composition did not change during the experiment. However, if the hypoeutectic side of the GFA cusp was as flat as the one seen in this chapter, no changes in the melting behavior would be seen even for relatively large changes in boron content (and hence, GFA). This explanation would be consistent with the very similar typical onset of nucleation in the system as fluxing occurs. The primary heterogeneous nucleation event would still be the limitation to further undercooling in these systems regardless of small boron additions, and the increase of intrinsic GFA may be generally inaccessible

due to challenges in removing the final heterogenous nucleant in these systems, but occasionally realizable in the circumstances described in Chapter 1.

The exponential curve used to fit the fragility data in Fig. 2.6 is clearly not an appropriately physical model. Continuing the extrapolation much further on the hypoeutectic side would result in extremely high fragility values, ones that would exceed that seen for pure metal melts (which would likely be about as fragile a system as could be achieved). Unfortunately, not enough data was collected to make an accurate determination of what function actually fits the data appropriately. An argument can be made that a sigmoidal function could fit the data near these GFA cusps well. A sigmoidal function could capture the very large changes in fragility seen near the GFA cusp, while having the appropriate limiting behavior on the hypoeutectic side and capturing the flatting seen on the hypereutectic side. Because fragility is solely a function of the liquid composition, it makes some intuitive sense that a sigmoid could adequately represent the underlying physics. A sigmoid would imply limiting behavior of constant fragility (with different fragility for each liquid) with a transition region with large changes in fragility. If the metallic liquids on each side of a eutectic represented different liquids (such as differently structured icosahedra), the eutectic would be a region of transition between these two liquids, where each get expressed in some part. As you move further away from the eutectic on each side, one configuration tends to dominate until sufficiently far from the eutectic only one configuration is almost solely expressed.

In addition to the physically intuitive nature of the above description, some minor evidence exists that is what is occurring. In these nickel alloys the toughness demonstrates interesting behavior[61]. In these systems a large composition range has notch toughnesses above 90 MPa$\sqrt{m}$, another large composition range has notch toughness below 30 MPa$\sqrt{m}$, and the transition region between the two is rather narrow and corresponds with the GFA peak. Distinct liquids in these two regions being quenched to form materially different glasses makes sense, as many other factors to explain different toughnesses (process history, cooling rates, material quality, etc.) should be quite similar between these different composition ranges. This certainly does not prove the simple model described earlier, but it provides a modicum of support for the idea of sigmoidal fragility curves near the glass transition. Significantly more work would need to be done to validate this hypothesis. One challenge in pursuing this line of work is that there are very few

systems that can map a wide range of fragility around a glass forming peak. Ideally, systems would have large GFA around a peak, have relatively sharp changes in m as a function of composition, avoid nanocrystallization near Tg, and have a relatively wide range of structural stability on each side of a peak so that no other structural changes interfere with the tail of the sigmoid. As shown in Chapter 4, even when all the factors are seemingly in place, getting quality fragility data over a wide composition range is quite challenging.

Computational approaches to determining structural data may be very helpful here. The largest limitation in using computational techniques to study glassy phenomena is that the timescales for molecular dynamics and first principles approaches are many orders of magnitude too fast to capture the relaxation of the glassy structure. Because this would be looking at liquid structure, the challenges in timescales would not materially factor into the equation and study of the structure of these near-eutectic liquids could be pursued, greatly helping understand the physical models behind liquid fragility in these systems.

Chapter 3

VIBRATIONAL ENTROPY OF METALLIC GLASSES THROUGH THE GLASS TRANSITION

3.1 Abstract

Vibrational entropy does not materially contribute to the excess entropy of metallic glasses. Measurements of the phonon density of states at temperatures above and below the glass transition were measured using inelastic neutron scattering, and vibrational entropy was determined from the density of states. DSC measurements using step calorimetry were used to determine the overall heat capacity of the glass, liquid, and crystal states. By comparing the contribution of vibrational entropy to the overall increase in entropy in a relatively fragile glass, $Zr_{50}Cu_{50}$, and a relatively strong glass, $Zr_{46}Cu_{46}Al_8$, it is shown that vibrational entropy does not materially contribute to the excess entropy for these two alloys, and it is likely that this is true for metallic glasses in general.

3.2 Introduction

3.2.1 Nature of the Glass Transition

Despite millenia of humans' use and creation of glasses, understanding the nature of the glass transition is an unresolved problem in glass physics. Compared to crystalline counterparts, glasses have some unique challenges in understanding the underlying physical mechanisms. Notably the lack of translational symmetry means that a lot of mathematical tools developed for studying the underlying structure of crystals are not available for understanding the random structure of glasses. Additionally, the random structure means that there is significant heterogeneity in an atom's local environment. This variation will result in different areas responding differently to environmental effects like stress and temperature. While there are bulk responses from a given glass sample, the lack of consistent long range order means that teasing out information about structure from aggregate data is limited. With the rise of atomic scale resolution in microscopy the local atomic arrangements can be understood much better, but there are still significant problems in elucidating what occurs during the glass transition, in no small part because there is no good physical

understanding of what the glass transition is.

The glass transition, which is the transition from a glassy state to a supercooled liquid state upon heating, is a challenging phenomena to study. This transition has been defined kinetically and thermodynamically, and while these definitions often give similar values for the glass transition temperature, the differences that can arise can be notable. The kinetic definition is that the glass transition has an equilibrium viscosity 10^{12} Pa·s or equivalently 10^{13} Poise. This definition, while concrete, is ultimately unsatisfying, as there is no real underlying physical significance to that viscosity; it is essentially a measure of when the deformation of a sample changes from solid to deformable under laboratory timescales and forces. While unsatisfying, there are some notable advantages to the kinetic definition. The number is well defined, and does not materially depend on experimental parameters with the notable exception that faster deformation rates can often make the flow non-newtonian, which can lower the viscosity for these materials. For sufficiently slow strain rates, the values will be constant. Viscosity near the glass transition has been shown to be processing path dependent, and there is good reason to believe that it is independent of processing path. More experimentally favorable, the data is very easy to interpret, and problems like nanocrystallization show up very readily. And the viscosity measurement of choice in this viscosity range, beam bending, has very easy sample production and preparation.

There are notable downsides with using this definition of the glass transition temperature. As noted earlier, there is no physical significance to the definition of 10^{12} Pa·s, it is merely a convenient cut off point. This makes this definition useful as a comparator between systems and as a processing parameter, but it is otherwise not meaningful. Additionally, not all glasses can have their viscosity measured in this range. When a materials ΔT is too low, the sample will crystallize before the material can relax into its equilibrium liquid state. There is a way to extrapolate the equilibrium value by the relaxation behavior of the material before crystallization using a Kohlrausch stretched exponential function[18], but this can be very tricky to do, and in cases where the ΔT is quite low the extrapolation could be over an order of magnitude, greatly reducing confidence in the conclusion.

The thermodynamic definition defines the glass transition as the temperature where the heat capacity of the sample increases discontinuously upon heating. This definition can be described using the Gibbs and DiMarizo[37] approach, which has the

glass below T_g stuck in a single configuration and the liquid above T_g free to explore additional configurations. This approach forms the foundation for the canonical Adam-Gibbs relationship, which connects the kinetics of the glass transition to the changes in potential configurations[2].

This thermodynamic approach has more of a physical basis but presents its own unsatisfying problems. This change in heat capacity does not happen at a set temperature, the temperature changes with different heating rates and is spread out over a wide temperature range (the width of the transition is dependent on the heating rate). This ultimately is because the glass transition defined this way is related to atomic mobility, which changes in a continuous fashion in these temperature ranges. Without a binary transition, the glass transition is going to occur when the material relaxation timescales overlap with laboratory timescales. Additionally, due to the random nature of the glass, in the process of moving towards equilibrium certain regions are going to be less constrained by their local environment and will readily move to equilibrium, but other regions will be hampered by their environments and will move more slowly to equilibrium. When heating at faster rates there is less time for the atoms to rearrange themselves at lower temperatures, and the apparent glass transition is higher. Notably, requires a heating rate to see this effect, moving to a temperature and holding does not cause the signal to show up as it does when heating the sample. Equilibrium can be attained, and the heat capacity of the liquid will be higher than the glass when it is attained, but the timescales involved smear out any signal past the point of utility.

There are some advantages to this definition. Essentially every glass, even ones with very low ΔTs, can have a glass transition identified. Due to heat capacity's connection with the other thermodynamic variables, you can get a lot more information from a well done experiment than you can by doing viscosity measurements. And if the signal is weak, it is often merely a function of adding more sample to improve the signal, an advantage that cannot be nearly as readily replicated in the beam bending case. Because of these advantages, the glass transition is often defined using this method, and is usually defined for a 20 K min^{-1} heating rate, though 10 K min^{-1} is often used as well.

While experimental approaches have challenges, there are also significant problems in doing calculations of physics during the glass transition. First principles calculations struggle due to the lack of periodicity and the wide variety of atoms that are

often present in glasses. Methods such as molecular dynamics struggle with glass transitions due to the wide disparity in time scales, with molecular dynamics doing calculations at pico- and nanoseconds, while the timescales of glass transitions being on the order of seconds, minutes, and hours. Continuum approaches can model glasses, but lack the ability to understand the underlying structure and physics.

While thermodynamics is inherently an aggregate measurement, it may be one of the most promising approaches to understanding the underlying physics. Because of the connections between the different thermodynamic functions and statistical mechanic ensembles you can learn a lot about structure from thermodynamics. There is one big problem with the way most experiments of the thermodynamics of metallic glasses are done, a heat capacity measurement during a constant heating scan is used as the basis of all the calculations. However, because of the heterogeneity of local structures there is heterogeneity in relaxation times, and these constant scan rates do not account for these effects. Other approaches are significantly more challenging, and so for metallic glasses there is a dearth of quality thermodynamic data.

3.2.2 Entropy in Metallic Glasses

Entropy is a thermodynamic state variable that has a direct relationship with the structure and composition of the material. While entropy cannot directly be measured, changes in entropy are related to the heat capacity of a material when the material undergoes heating or cooling as given by:

$$c_p = T\frac{\partial S}{\partial T}_P \tag{3.1}$$

Entropy can also be found by measuring the enthalpy evolved in a phase transition, given by:

$$\Delta S_{transition} = \frac{\Delta H_{transition}}{T_{transition}} \tag{3.2}$$

Thus, by measuring the heat evolved in a phase change or during a controlled heating or cooling of a material the change in entropy of a system can be measured.

While there are many source of entropy, in metallic glasses it can be broken down into two main components: vibrational and configurational. Configurational entropy

is the entropy given by the possible unique arrangements of atoms in the liquid or solid. In crystals this calculation is straightforward, but in random structures like glasses and liquids it becomes useful to utilize a potential energy landscape (PEL) approach to address available configurations.

The potential energy landscape was first conceived by Goldstein[25] and was latter developed by Stillinger and Debenedetti [14] into the potential energy landscape. One useful aspect of the PEL framework is that it allows for a convenient separation of entropy into configurational entropy, which is due to the ability to sample different energy minima, and vibrational entropy, which is due to the vibrations in those minima. Going beyond the PEL abstraction, the vibrational entropy arises from the phonons in the material. This dynamical entropy is measurable: by taking integrating over the phonon density of states a quantitative value of vibrational entropy can be determined.

The entropy of glasses and liquids is often referenced with regards to a crystal. Due to their random configuration, glasses and liquids have higher entropy than their crystalline counterparts. By taking the difference of the crystal entropy from the glass or liquid entropy you get a measure known as excess entropy. The origin of this excess entropy is not well known. The classic description of the origin of excess entropy was given by Gibbs and DiMarizo[37], shown in Fig. 3.1a, where the excess is strictly due to the increase in configurational entropy. Another model, as given by Goldstein[26] and shown in Fig. 3.1b, says that vibrational entropy contributes to the excess entropy of the glass and supercooled liquid. This data has been measured for molecular and network glasses[26][29][39], and in these systems vibrational entropy did contribute to excess entropy (see discussion for further details).

Collecting vibrational entropy data and discovering the origin of excess entropy in metallic glasses is challenging. As noted in the preceding subsection, metallic glasses often have very low ΔT, which means that the temperature region for collecting data is small and time-limited. It is only with recent improvements in neutron beam lines and instrumentation that the timescales of measurement have shrunk below the timescales to crystallize a glass near the glass transition temperature. Other approaches, such as cooling a liquid from above the liquidus and measuring the phonon spectra near the liquidus has several challenges. Liquids cannot be easily measured at the SNS. Metallic glasses often contain reactive metals (the ones studied in this experiment contain zirconium) which make finding suitable containers very

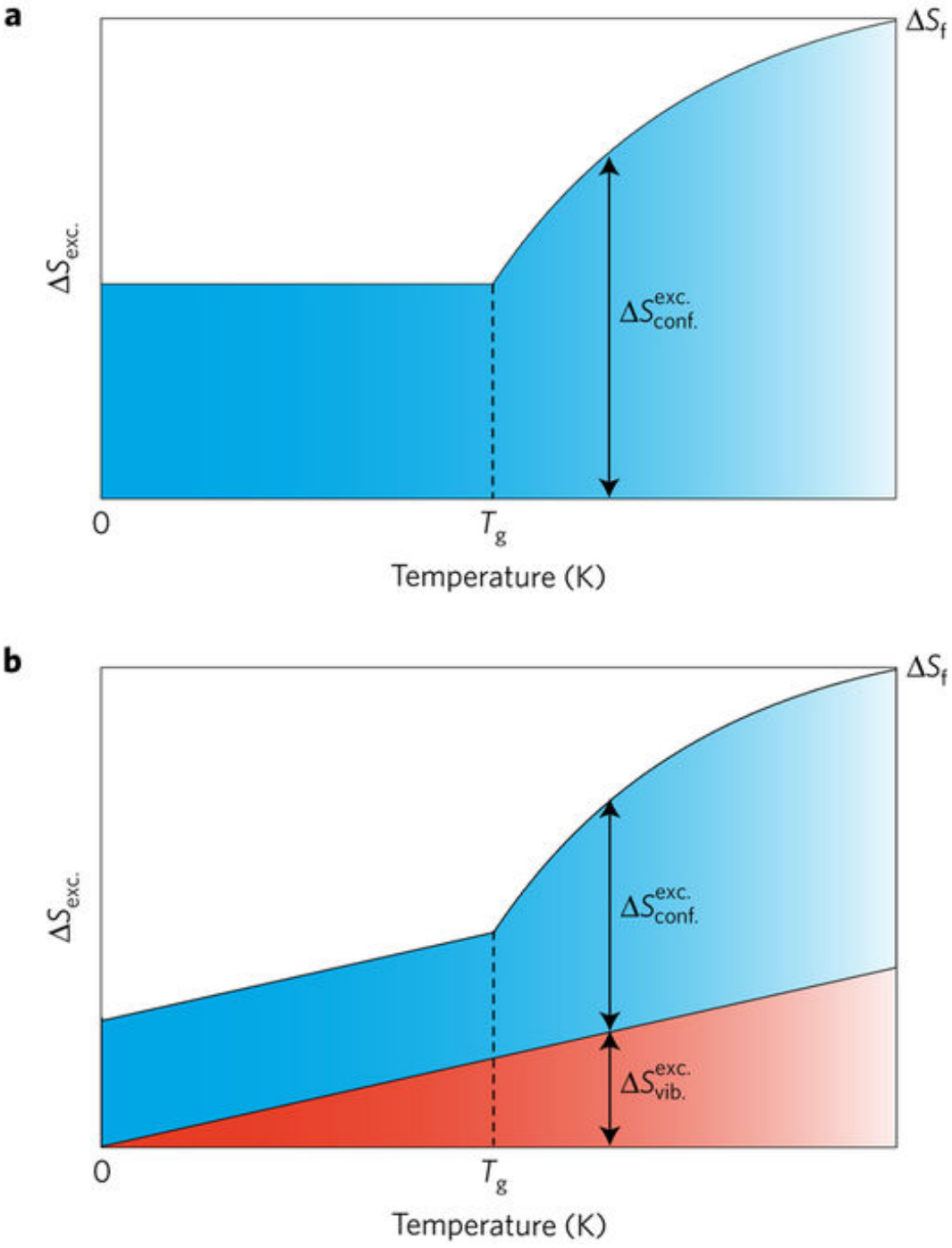

Figure 3.1: Schematic diagram of excess entropy of a glass in the glass and supercooled liquid temperature ranges. a) shows the excess entropy in a Gibbs and Dimarizo[37] model. b) shows the excess entropy where the vibrational entropy contributes to the excess entropy, as argued by Goldstein[26]

challenging.

3.2.3 Inelastic Neutron Scattering

Inelastic neutron scattering is a powerful technique to understand atomic motion in materials. This thesis will only provide a short introduction necessary to understand the principles and experimental overview, more detailed treatments can be found in a handbook [22] or in any number of Fultz group theses.

Scattering can be characterized using two main distinctions: whether the scattering is coherent and whether it is elastic. Coherent scattering maintains the phase relationship between the incident and final waves. In incoherent scattering the phase information is not preserved. Elastic scattering has no gain or loss of energry in the wave due to interacting with the scattering centers. Inelastic scattering has a gain or loss of energy to the scattering center which is manifested as the creation or annihilation of a phonon.

Neutron scattering has several uses, but most notably for this work it is the ability to determine atomic and molecular motions that make it useful. Coherent inelastic neutron scattering is used to generate a phonon density of states for the material being studied. Measured simultaneously, elastic scattering gives a diffraction pattern that can show the evolution of structure in the supercooled liquid and as the material crystallizes.

Neutrons have no charge and so can penetrate materials and scatter from atomic cores by interacting using nuclear forces. Neutrons tend to scatter weakly, and measurement of uncharged particles is more challenging. Due to these and other factors, the flux of neutrons is significantly lower than that of other sources, on the order of 10^4 s^{-1} mm^{-1}[75]. Older systems, with even lower fluxes, basically precluded the study of metallic glasses in the supercooled liquid temperature range as the timescales to get good statistics did not allow for liquids to exist without crystallizing. Previous studies of phonon spectra in metallic glasses only looked at the glass and did not take any measurements in the supercooled liquid[80][81][79].

3.3 Results and Methods

3.3.1 Sample Preparation

The alloys were chosen because they satisfied a number of criteria. They had a sufficiently high ΔT to get sufficient data in the supercooled liquid while collecting

neutron scattering data. Their scattering cross sections, weighted by their concentration, were similar, so the signal was not dominated by the scattering off of any one element. Binary copper zirconium alloys are one of the most canonical metallic glass sytems, with significant study both experimentally and computationally. $Cu_{50}Zr_{50}$ has a higher GFA than most binary alloys, so it could be make into samples more easily. $Cu_{50}Zr_{50}$ additionally has a B2 phase transition in the crystal which is of interest. $Cu_{50}Zr_{50}$ has an Angell fragility of 62, making it a relatively fragile glass[68][98][4]. $Cu_{46}Zr_{46}Al_8$, a ternary derivative of the binary alloy, is much stronger with a fragility of 42[98][4][38].

Ingots of $Cu_{50}Zr_{50}$ and $Cu_{46}Zr_{46}Al_8$ were prepared from a mixture of the elements of purity ranging from 99.99% to 99.999% by arc-melting under a Ti-gettered argon atmosphere. They were rapidly cast into evacuated copper molds under inert gas atmosphere to form amorphous strips. X-ray diffraction and differential scanning calorimetry confirmed that the as-cast strips were fully amorphous.

3.3.2 Inelastic Neutron Scattering

The ARCS neutron spectrometer at the Spallation Neutron Source allows the acquisition of an INS spectrum in a few minutes[1] [76]. INS data were acquired during continuous heating of the amorphous material at a rate of 2 K min^{-1} through the glass transition and above crystallization, and again when cooling to room temperature. Event mode data collection assigns a detector position and time stamp to each neutron detection event, and all processing and binning occurs later. This approach allows the data to be post-processed in several ways to compare the effect of binning over different temperature ranges. The rate of heating, 2 K min^{-1}, was selected to allow sufficient collection of statistics to obtain a density of states (DOS) with as little as 120 s of data, or a 4 K change in temperature.

Differential scanning calorimetry (DSC) measurements with continuous heating were performed to verify the onset of the glass transition and crystallization during the neutron experiment. DSC scans at 2 K per minute are shown in Fig. 3.6. The onsets of the glass transition and subsequent crystallization transition are indicated by arrows. The shaded region in Figs. 2–4 indicates the temperature range where each material is in the supercooled liquid state. Diffraction patterns obtained from elastic scattering during the neutron scattering experiment were used to determine the absolute sample temperature, in combination with the crystallization temperature

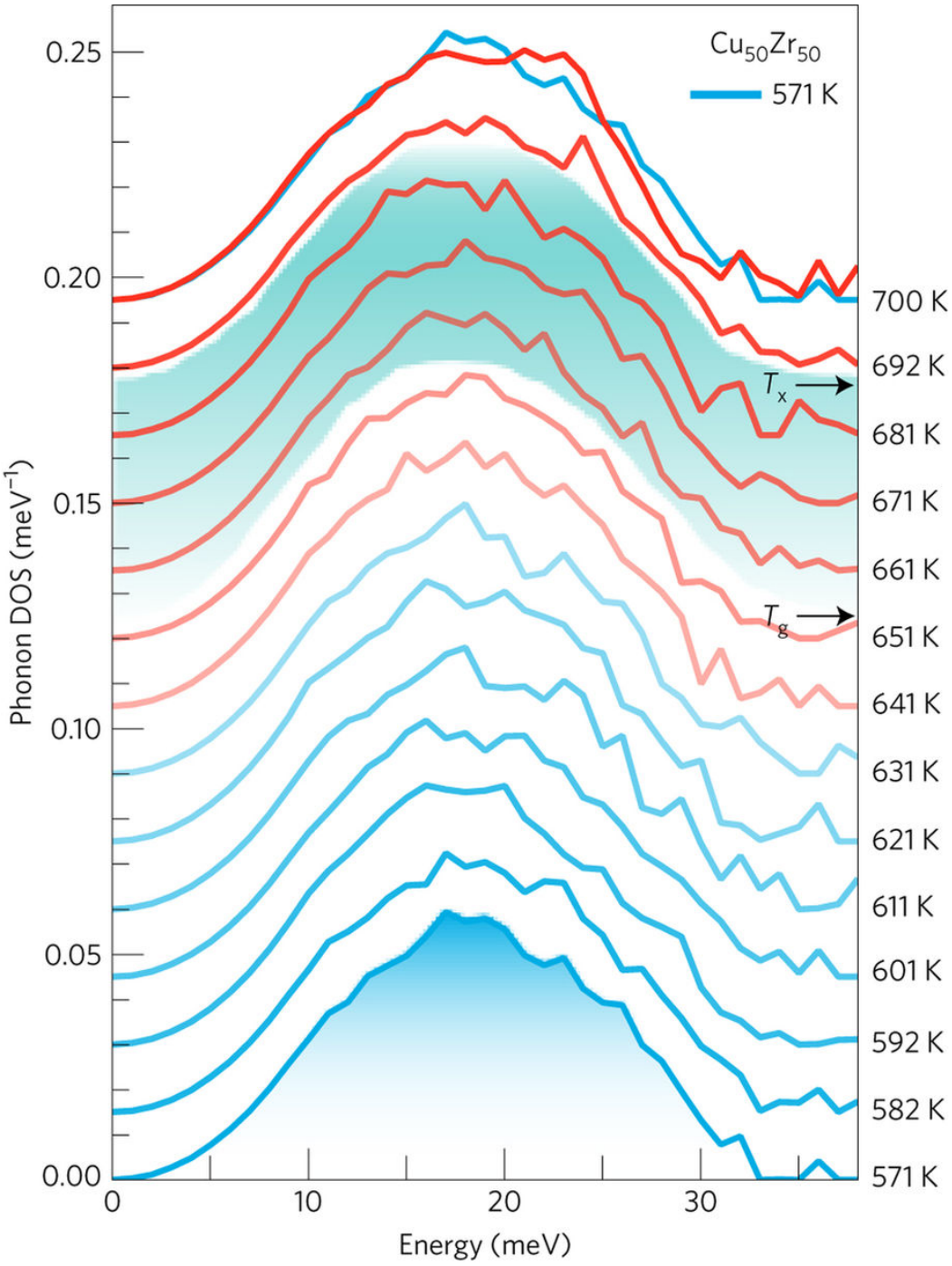

Figure 3.2: DOS curves were obtained during the heating from the amorphous state at 571 K through the glass transition and crystallization transition 790 K. Data were acquired during continuous heating at 2 K min^{-1} and binned in 10 K intervals. Each spectrum was acquired in 3–6 min. The 571 K DOS of the amorphous phase (shaded blue) is shown also at high temperature, overlaid with the DOS of the crystalline phase at 700 K.

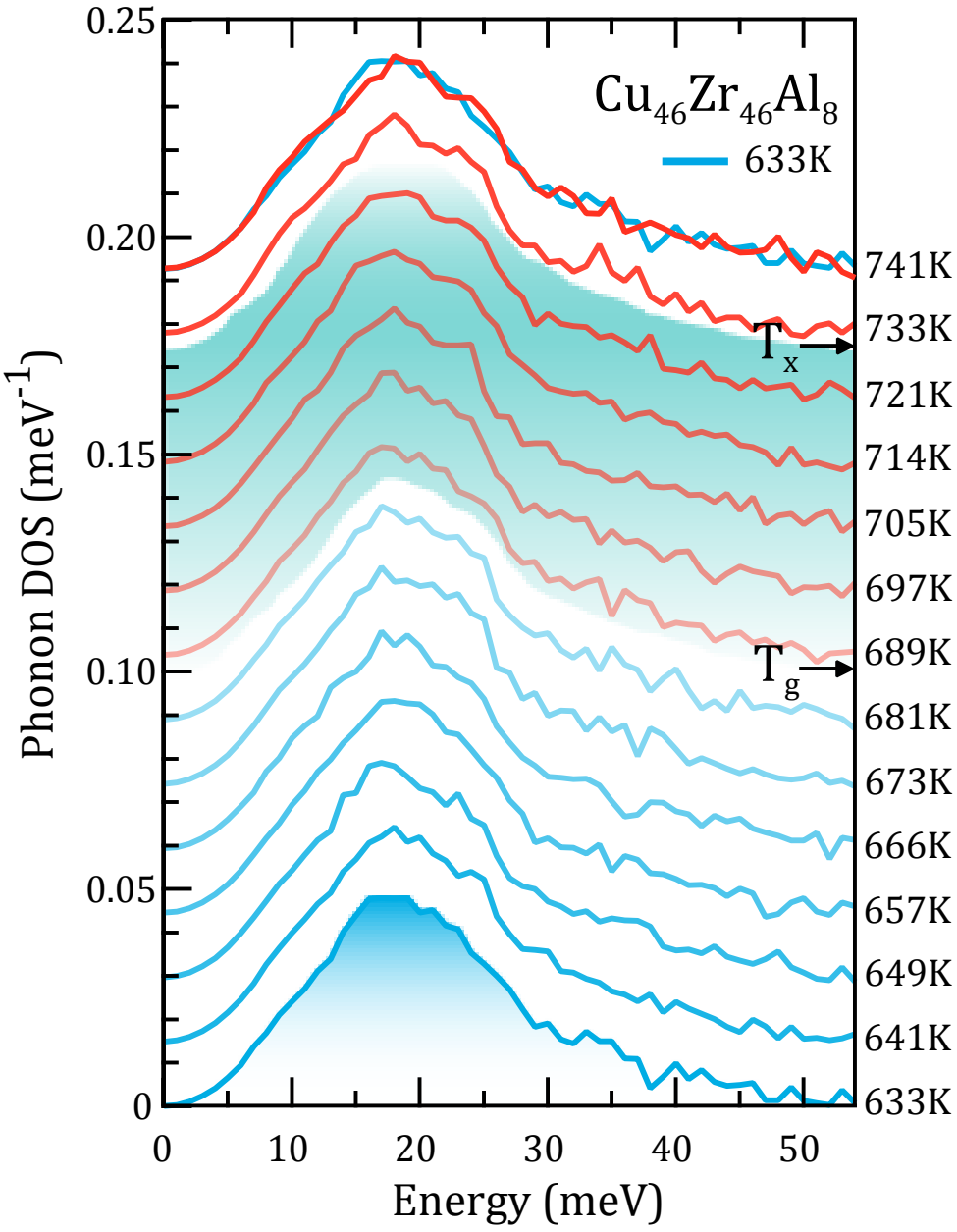

Figure 3.3: DOS curves were obtained during the heating from the amorphous state at 633 K through the glass transition and crystallization transition 730 K. Data were acquired during continuous heating at 2 K min^{-1} and binned in 8 K intervals. Each spectrum was acquired in 3–6 min. The 633 K DOS of the amorphous phase (shaded blue) is shown also at high temperature, overlaid with the DOS of the crystalline phase at 741 K.

determined from DSC. The diffraction patterns are shown in the Supplementary Information.

Analyses of the inelastic scattering data were used to obtain phonon DOS curves for data averaged over 4 K, 10 K and 25 K ranges of temperature with the energy axis binned between 1 and 3 meV. A representative set of spectra for $Cu_{50}Z_{50}$ averaged over 10 K in temperature with the energy axis binned every 1 meV are shown in Fig. 3. The shaded region indicates the temperature range during which the material is in the undercooled liquid. These curves show little change with temperature. The spectrum at the highest temperature shows a small change after crystallization. A similar set of phonon DOS curves for $Cu_{46}Zr_{46}Al_8$ are included in the Supplementary Information. The vibrational entropy was assessed for each DOS curve, g (E), in Fig. 3.4 as:

$$S_{Vib}(T) = 3k_B \int_0^\infty g(E)([1 + n(T)]ln[1 + n(T)] - n(T)lnn(T))dE \tag{3.3}$$

where

$$n(T) = \frac{1}{e^{\frac{E}{k_B T}} - 1} \tag{3.4}$$

is the Planck distribution for phonon occupancy[87][3]. When g (E) is measured at the temperature of interest, equation (3.3) is rigorously correct for the effect of harmonic and quasiharmonic vibrations on the entropy, and for the effects of electron–phonon interactions on these vibrations. It also provides a good accounting for any anharmonic entropy shifts of vibrational frequencies[87][3]. Fig. 3.4 presents the vibrational entropy obtained during heating of the glass/liquid phase (red filled symbols) and cooling of the crystalline phase (blue open symbols) for $Cu_{50}Zr_{50}$ and $Cu_{46}Zr_{46}Al_8$. Square symbols represent temperature bins of 8 or 10 K and circle symbols represent temperature bins of 25 K. The red filled symbols show the vibrational entropy of the amorphous material through the onset of T_g with the shaded region indicating that the material is in the undercooled liquid. The blue open symbols show the vibrational entropy of the crystalline phase measured after the material is cooled from above the crystallization temperature. Differences in the glass/liquid and crystalline phases for each material are absolute; however, direct quantitative comparison of the vibrational entropy values for $Cu_{50}Zr_{50}$ and $Cu_{46}Zr_{46}Al_8$ should

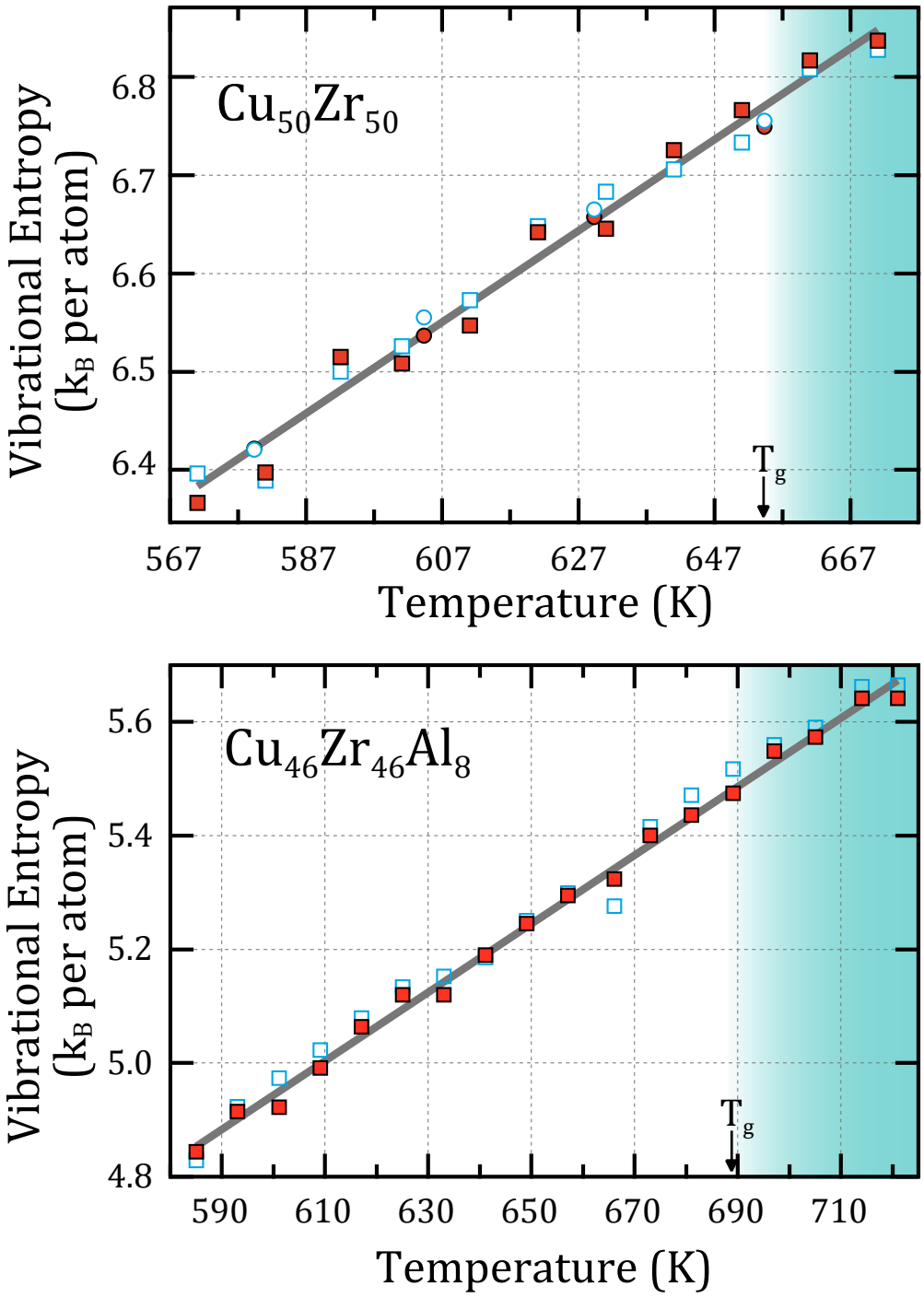

Figure 3.4: The vibrational entropy is assessed by integration of the DOS curves that were acquired during heating of the glass and supercooled liquid (red filled symbols) and cooling of the crystalline phase (blue open symbols). Square symbols represent temperature bins of 8 or 10 K while circle symbols represent temperature bins of 25 K. The red filled symbols give the vibrational entropy of the glass through T_g, indicated by an arrow, where the glass relaxes to the supercooled liquid indicated by the shaded region. The blue open symbols give the vibrational entropy of the crystalline phase measured during cooling from above the crystallization temperature. Linear fits to all data are shown in grey.

be avoided because the addition of aluminium skews the weighting of the densities of states, which was not corrected here. In addition, the use of two different furnaces for these measurements provides significantly different background profiles, complicating the elimination of multiphonon and multiple scattering (see the last two paragraphs of this subsection).

Two features are notable in both plots in Fig. 3.4. First, the vibrational entropy through the glass transition into the supercooled liquid increases monotonically with temperature, with no discernible discontinuity in slope at T_g . Second, there is little difference in the vibrational entropy of the glass/liquid phase and the crystalline phase. Specific differences in the data for heating (red filled symbols) and cooling (blue open symbols) are difficult to distinguish. At a given temperature, the difference in vibrational entropy between the glass/liquid and crystal is approximately 0.1 J mol^{-1} K^{-1}, or approximately $0.01k_B$ per atom, for both materials. This indicates that while there is a contribution of vibrational entropy to the total entropy, there is very little excess vibrational entropy contribution to the total excess entropy. A linear fit to all of the data is indicated with a grey line.

The present neutron scattering results are not sensitive to phonons with long wavelengths, owing to the tails of the elastic peak in the inelastic spectra. Corrections for these tails were done consistently for all spectra, but the shape of the low-energy part of the DOS may not be accurate. The low-energy part of the phonon DOS can be estimated from measurements of the velocity of sound through the glass transition in a compositionally similar metallic glass, $Zr_{46.25}Ti_{8.25}Cu_{7.5}Ni_{10}Be_{27.5}$[48]. It was reported that the shear and bulk moduli decreased by approximately 7% and 4%, respectively, giving an approximate change in vibrational frequency at long wavelengths of 3%. In the high-temperature limit, this corresponds to a change in vibrational entropy of $\Delta S = 3\ln(1.03) = 0.09k_B$ per atom. Generously assuming that 10% of the phonon DOS follows the change of sound velocity through T_g, we obtain an increase of vibrational entropy at T_g of approximately $0.01k_B$ per atom, which is very small.

The increasing viscosity of a liquid with increasing undercooling reflects the decreasing mobility of atoms. Measured viscosities and diffusivities allow estimates of the characteristic structural relaxation time of glass-forming liquids. In the high-temperature liquid (above the melting temperature), relaxation times are very short, on the order of nanoseconds, but around T_g, where the current measurements were

performed, relaxation times are on the order of 1-100 s[10]. The energy resolution, a design property of the neutron spectrometer, determines the timescale of the measurement. For the spectrometer used in these neutron experiments, flow on this timescale will not be observable, as sampling times for the dynamics are set by the neutron monochromatization and are on the order of 10-11 s.

Inelastic neutron scattering measurements were performed with ARCS, a time-of-flight Fermi chopper spectrometer at the Spallation Neutron Source at Oak Ridge National Laboratory. For $Cu_{50}Zr_{50}$, eighteen amorphous plates were arranged to form a larger plate approximately 30 mm in width and 39 mm in height, and held in an Al foil packet. For $Cu_{46}Zr_{46}Al_8$, five amorphous plates were arranged to form a larger plate approximately 30 mm in width and 40 mm in height, and held in a Nb foil packet. Both samples had a thickness of 1.0 mm, giving a ratio of multiply to singly scattered neutrons of approximately 5%. The measurements were performed with a monochromatic beam of neutrons with an incident energy of 85 meV and 70 meV, respectively. Measurements of $Cu_{50}Zr_{50}$ were performed in a low-mass electrical resistance furnace with aluminium shielding. Measurements of $Cu_{46}Zr_{46}Al_8$ were performed in a radiative furnace (MICAS furnace) designed for high-temperature operation and shielded with five concentric vanadium cylinders.

Data reduction was performed with DGS reduction in Mantid[5]. For each data set, the raw neutron detection events are binned to obtain a scattering intensity S(E, 2θ) as a function of energy transfer (E) and scattering angle (2θ), and normalized by the proton current on target. A white-beam measurement of a standard vanadium sample is used to correct for detector efficiency. The S(E, 2θ) is then rebinned into the intensity S(Q,E) with momentum transfer $\hbar$Q ranging from 1.0 to 10.0 Å^{-1} and binned every 0.05 Å^{-1}. Elastic scattering gives most of the intensity, but its shape is set by the spectrometer resolution[1], which does not change with the sample. The elastic linewidths for all three states of the material measured (amorphous, liquid and crystal) were consistent with a standard sample of vanadium, an incoherent scatterer. To separate the dominant elastic scattering from the inelastic scattering, the elastic peak is subtracted from the data below a given energy and replaced with a monotonic function of energy that is characteristic of the inelastic scattering in the long-wavelength limit. Reduction to a 1-phonon profile and a phonon DOS is based on the multiphonon expansion[72], which works best over a range of momentum transfer[90]. The data were corrected for multiple and multiphonon scatterings

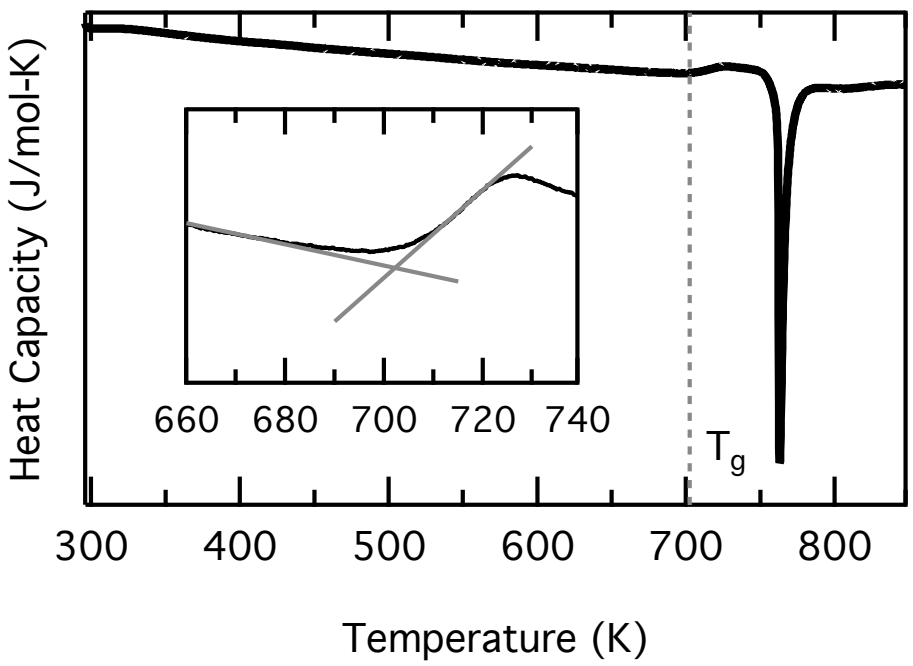

Figure 3.5: Differential scanning calorimetry of $Cu_{46}Zr_{46}Al_8$ at 10K min^{-1} from room temperature through crystallization. Figure inset is a zoomed in view of the curve near the glass transition, showing the use of common tangents to determine the glass transition temperature.

simultaneously with the getdos package (http://code.google.com/p/getdos) as described by Kresch and colleagues[17].

3.3.3 DSC

Calorimetry was used to determine the heat capacity of the metallic glass in the glass, supercooled liquid, and liquid regimes. Fig. 3.5 shows a continuous heating of $Cu_{46}Zr_{46}Al_8$ at 10 Kelvin per minute from room temperature through crystallization. The glass transition and crystallization temperatures are obtained from this continuous scanning process. A comparison of $Cu_{50}Zr_{50}$ and $Cu_{46}Zr_{46}Al_8$ near the glass transition can be seen in figure 3.6 and an overall DSC run can be seen in figure 3.7. The discrepancies in T_g in the different runs are due to the varying heating rates.

Heat capacity data, however, should not be obtained using continuous scans. For a more thorough discussion of heat capacity data collection, see the discussion

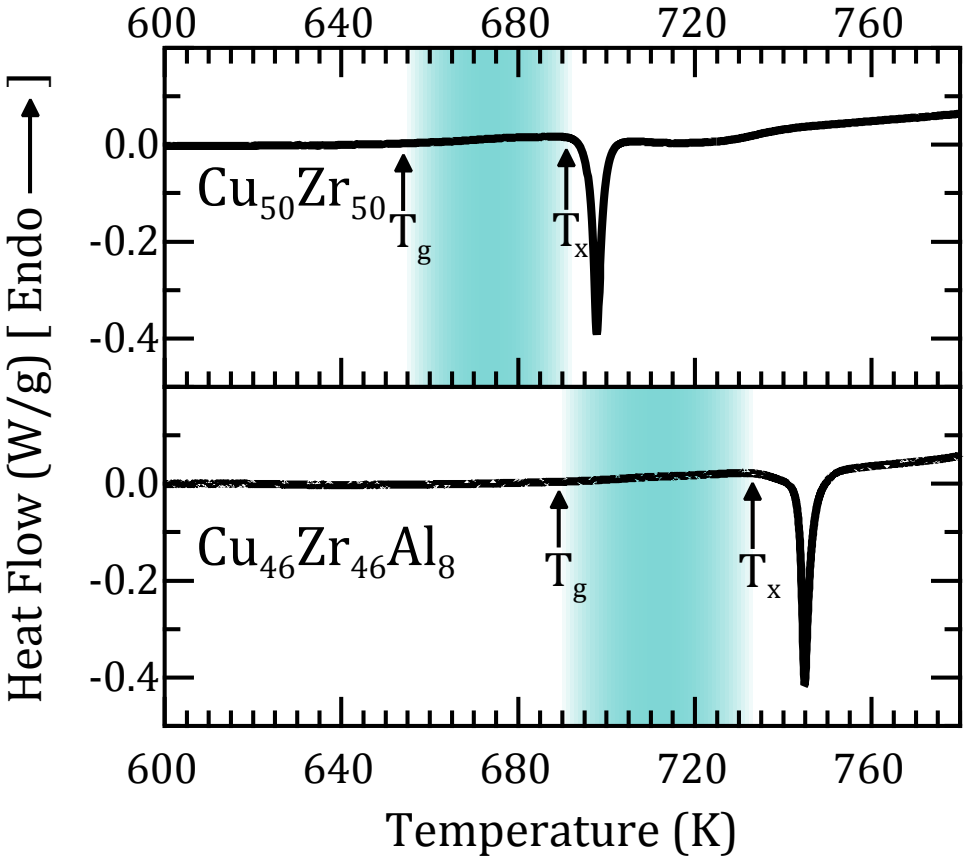

Figure 3.6: Differential scanning calorimetry of $Cu_{50}Zr_{50}$ and $Cu_{46}Zr_{46}Al_8$ at 2K min^{-1} near the glass transition. The ternary $Cu_{46}Zr_{46}Al_8$ has a slightly wider ΔT and a significantly higher T_g than binary $Cu_{50}Zr_{50}$.

section of Chapter 4. Step calorimetry was used to determine the heat capacity of the samples.

Step calorimetry was done for the glassy, supercooled liquid, and high temperature liquid (higher than T_L) regimes independently. This was done for two reasons. Firstly, the Netzsch DSC used had limitations on the number of steps that could be done in a single program, necessitating breaking up the analysis into several temperature ranges. Secondly, results were most accurate when the signal of the sample, $m * c_p$ was comparable in magnitude to the signal of the sapphire calibration standard. In the region of the glass transition where the heat capacity is changing rapidly (in Figure 3.8 the heat capacity in question is ~30-~45) a new sensitivity calibration would have to be done for each data point, and the process of getting the

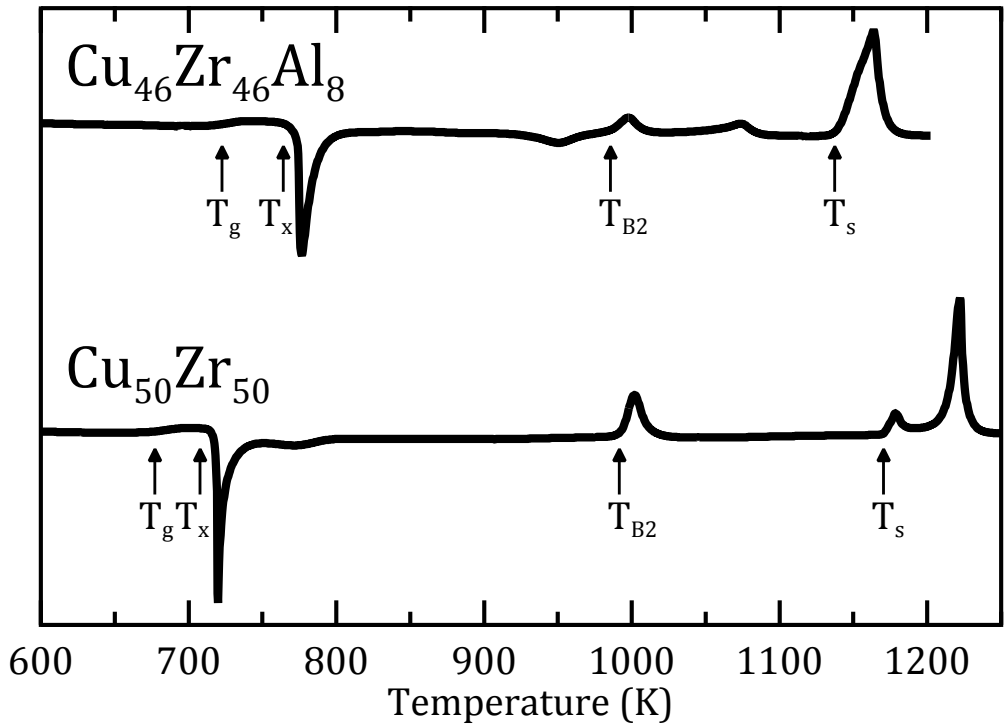

Figure 3.7: Differential scanning calorimetry of $Cu_{50}Zr_{50}$ and $Cu_{46}Zr_{46}Al_8$ at 20K min^{-1} through melting. The highlighted temperatures are the glass transition T_g, the crystallization temperature T_x, the B2 phase transition temperature T_{B2}, and the solidus temperature T_s.

right masses for a given calibration was a laborious trial and error process.

Step calorimetry is the most accurate scanning method of determining heat capacities in a DSC, but it presents unique challenges. Given the often narrow temperature range that a metallic glass can exist as a supercooled liquid, the step calorimetry program limited data collection in the supercooled liquid region for the alloys studied to a handful of points at most. For temperatures around and above the liquidus step calorimetry added significant amounts of time to the data collection process. These alloys contain zirconium, and at the liquidus temperature of the alloys the free energies of formation for the most stable oxides of aluminum and zirconium are essentially the same. So, at these temperatures, the alloy will reactively wet the alumina crucible and will proceed to start stripping oxygen from the sample container. This not only limits the amount of time available to make a measurement, but the wetting ruins the sample pans and makes the process of collecting data above the liquidus very tedious.

Step calorimetry can be done in some DSC systems as part of the run program, though those machines were not available for these experiments. The samples were heated at 20 K min^{-1} to the lowest temperature of interest, held for one minute isothermally, then raised at 20 K min^{-1} for one minute and then held isothermally again. These steps were continued for the temperature range of interest and gave an effective heating rate of 10K min^{-1} for the run.

We can then calculate the specific heat capacity of the sample using the following formula:

$$c_p(T)_{sam} = \frac{\dot{Q}_{sam} m_{ref} \mu_{sam}}{\dot{Q}_{ref} m_{sam} \mu_{ref}} c_p(T)_{ref} \tag{3.5}$$

$\dot{Q}_{sam}$ is the heat flux for the sample, $\dot{Q}_{ref}$ is the heat flux for the sapphire standard, m_{sam} is the mass of the sample, m_{ref} is the mass of the sapphire standard, μ_{sam} is the molar mass of the sample, μ_{ref} is the molar mass of sapphire, and $c_p(T)_{ref}$ is the specific heat capacity of the sapphire standard. It should be noted that the heat flux terms in the preceeding equation implicitly include the subtraction of the reference pan ($\dot{Q}_{sam}$ is really $\dot{Q}_{sam}$-$\dot{Q}_{refpan}$), but this is often transparent to the operator of the DSC.

The heat capacity fit for the liquid in figure 3.8 is given by a Kubaschewski relation[45]:

$$c_p(T)_{liq} = 3k_B + aT + bT^{-2} \tag{3.6}$$

with a=.0093 and b=3.78x10^6

The heat capacity for the crystal data is given by the following equation:

$$c_p(T)_{xtal} = 3k_B + cT + bT^2 \tag{3.7}$$

with c=.003 and d=6.52x10^{-6}

The data for $Cu_{50}Zr_{50}$ around the glass transition presents some challenges. The single data point was measured using many times using several different step sizes and they were all consistent, which gives some confidence in the value. However, it is just data for one temperature value. While the ΔT of $Cu_{50}Zr_{50}$ is sufficient

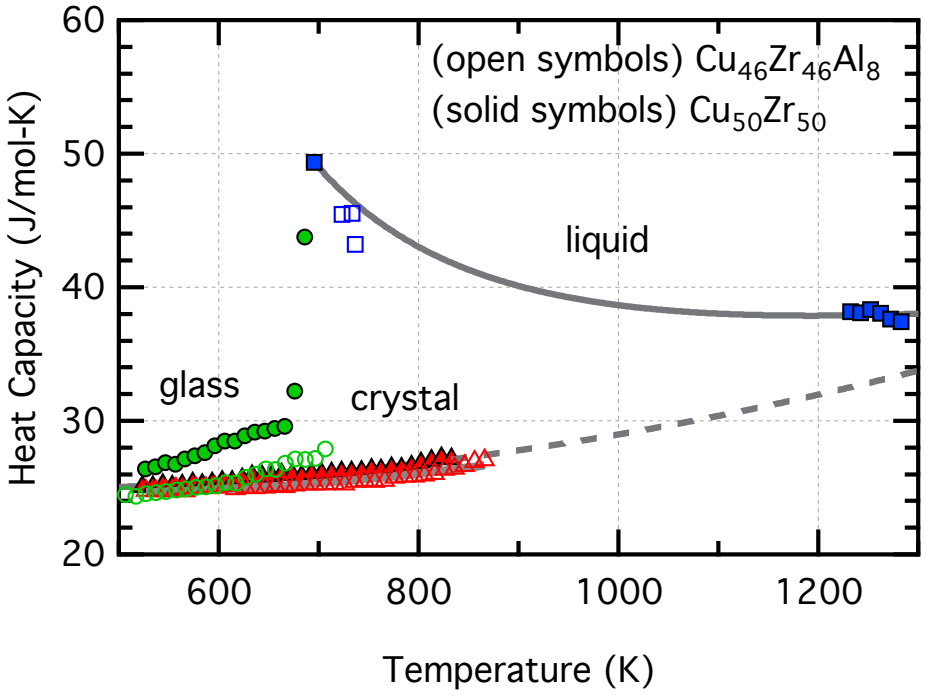

Figure 3.8: Heat capacity data for $Cu_{50}Zr_{50}$ and $Cu_{46}Zr_{46}Al_8$ with curve fits applied to the $Cu_{50}Zr_{50}$ data. Curve fits are given by equations (3.6) and (3.7). The blue squares are liquid data, green circles are glass data, and red triangles are crystal data.

to get one data point, the limits of step calorimetry with alloys with small ΔT present themselves here. Even the ternary $Cu_{46}Zr_{46}Al_8$, which had a wider ΔT, was only able to get a handful of data points in the supercooled liquid. Additionally, it presents some challenges when fitting the curve. Not only is using just a single point problematic for curve fitting in terms of the error it introduces, it does not let us actually determine whether or not the curve used to describe the thermodynamics in the supercooled liquid is up to the task. Given how much of the curve is interpolated, additional data points at the edges would be helpful, but data in the middle region would be significantly more helpful for fitting the curve.

In presenting the crystal data, while the crystal exists up to the liquidus at 1200K, the B2 phase transition prevents a simple illustration of the data above 850K. The dotted line in Fig. 3.8 is the extrapolated data from the lower temperature crystal phase.

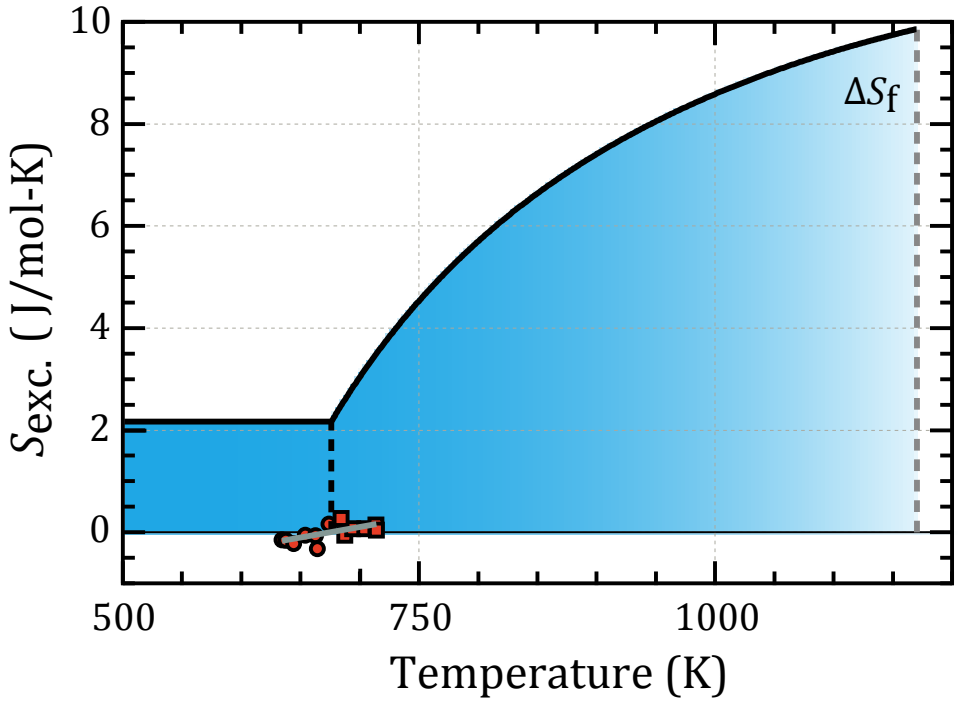

Figure 3.9: Total excess entropy of the liquid over the crystal phase of $Cu_{50}Zr_{50}$. The total excess entropy is evaluated by integrating the region between the fitted functions in Fig. 5. The glass-transition temperature Tg of 675 K (as determined from the step calorimetry experiments in Fig. 3.8) is indicated by a black dashed line, while the liquidus temperature of the alloy at 1,170 K is indicated by a grey dashed line. The symbols overlaid near Tg give the measured excess vibrational entropy of the glass (red circles) and liquid (red squares) phases over the crystalline phase. A linear fit through the symbols is also presented (grey line), revealing a negligibly small excess vibrational entropy. The residual excess entropy of the glass below Tg (black line) is approximately 2.2 J mol^{-1} K^{-1} and assumed to be entirely configurational.

3.3.4 Configurational Entropy

Using the entropy of fusion and fits to the crystal, glass, and supercooled liquid heat capacity data for $Cu_{50}Zr_{50}$, the area between the curves can be integrated to give the excess entropy of the liquid over the crystal. This data gives the black curve in Fig. 3.9. The entropy of fusion, ΔS_f, is calculated with reference to the crystal that is formed from the devitrification of the supercooled liquid. To calculate this value the entropy of formation of the B2 phase from the reference crystal is added to the entropy of fusion of the B2 phase. The entropy of formation for the B2 phase is 2.9

J mol^{-1} K^{-1} and the entropy of fusion for the B2 phase is 7.0 J mol^{-1} K^{-1}. The total entropy of fusion for the reference crystal is 9.9 J mol^{-1} K^{-1}.

Because the particular curve fits for the excess entropy above the glass transition temperature rely on underlying models which have not been fully validated by the data, caution should be taken when looking at the specifics of the curve. The general shape shown in Fig. 3.9is correct, though since many different power laws could fit the experimental data, functions with significantly more or less curvature could realistically fit the data. The Kauzmann temperature, which can be found by extrapolating the excess entropy in the supercooled liquid to zero, is evaluated to be 627K using the fits as determined earlier.

The vibrational entropy as shown in Fig. 3.4 are plotted in Fig. 3.9 with the glass data points corresponding to red circles and the supercooled liquid data points corresponding to red squares. A linear regression is shown in the figure as a solid gray line revealing a slight positive increase as a function of temperature. This increase should not be over analyzed, all the data points are close to zero and the regression would suggest a very slightly negative excess entropy below the glass transition, a result which suggests that this may just be the error of the data collection. Taking the data at face value, we can say that the excess vibrational entropy at the glass transition is .1 J mol^{-1} K^{-1} (0.01 K_B per atom), or about 4-5% of the overall excess entropy at the glass transition. The remaining excess entropy, 2.2 J mol^{-1} K^{-1} (0.27 K_B per atom), is therefore almost entirely configurational. Assuming no secondary configurational relaxations (that is, β relaxations) occur at T_g at the slow sampling rate (2 K min^{-1}), and accounting for an essentially zero excess vibrational entropy, as measured here, the excess entropy of the glass below T_g can be approximated as a horizontal line that intercepts the excess entropy of the liquid at T_g (black horizontal line in Fig. 3.9). The evaluated entropy function is therefore roughtly consistent with the classic picture of the glass transition as described by Gibbs and DiMarzio.

3.4 Discussion

Experimental assessment of vibrational and configurational entropy has previously been performed on molecular and network glasses. Low-temperature calorimetry measurements on such glasses[26][29][39] confirmed Goldstein's argument that the excess entropy of the liquid has contributions from molecular vibrations and anhar-

monic forces, in addition to configurational contributions[26]. By assuming that the vibrational entropy at 0 K is zero such that the excess entropy is entirely configurational, an excess vibrational contribution at T_g was obtained in those experiments by subtracting the excess entropy at 0 K from that at T_g. These measurements attribute between 20 and 80% of the excess entropy to excess vibrational entropy[26][29][39]. A few direct measurements of vibrational entropy have also been reported for network glasses. INS experiments by Phillips et al., on glassy and liquid selenium indicated a vibrational entropy contribution of 30% to the excess entropy at the glass transition[67], but aspects of their analysis have been questioned[40]. A more recent experimental study on $Ge_{20}Se_{80}$ using Raman spectroscopy suggested that vibrational entropy could provide as much as 20% of the additional entropy above the glass transition, but this study measured only a few vibrational modes in the material[23].

In the metallic glasses investigated here, the similarity of the DOS curves above and below T_g (as in Figs. 3.2 and 3.3) is direct evidence that the excess vibrational entropy is largely unchanged as the glass transition is traversed. From the phonon entropy data presented in Fig. 3.4 we can conclude that the change in vibrational entropy between the glass/liquid phase and crystalline phase is negligible, resulting in essentially zero, or very small, excess vibrational entropy in both $Cu_{50}Zr_{50}$ and $Cu_{46}Zr_{46}Al_8$. The excess entropy of the liquid and glass is therefore dominated by configurational entropy in these metallic glasses. This result was demonstrated here for two metallic glasses with significantly different fragilities, pointing to this being a universal feature of metallic glasses. However, this result need not be universal for all glasses. In fact the analysis of molecular and network glasses, where a significant vibrational contribution to the excess liquid/glass entropy was reported[26][29][39], points to a different conclusion. The authors of those studies attributed the higher vibrational entropy of the glass and liquid compared with that of the crystal to the low density and large anharmonic effects characterizing molecular and network glasses. Metallic glasses lack soft van der Waals bonds that dominate molecular and network glasses, and, as such, the difference in the density and thermal expansion between a metallic glass and its crystal is generally smaller[63]. The difference in bulk modulus between a metallic glass and its crystal is also known to be small[48]. Consequently, compared with molecular and network glasses, one may expect the vibrational entropy of a metallic glass to be closer to the crystal.

These results can be further interpreted in terms of the PEL theory[78][71]. In the PEL approach, the configurational entropy is determined by the number density of basins accessible at a given energy. The configurational entropy increases with increasing temperature as additional basins become accessible to the system with increasing temperature. Differences in the vibrational spectra of these additional basins could result in changes to the vibrational spectrum, but this effect is small for both the fragile $Cu_{50}Zr_{50}$ and strong $Cu_{46}Zr_{46}Al_8$. Martinez and Angell proposed that vibrational contributions to the excess entropy would be manifested as changes in the shape of potential energy basins with increasing temperature[58], and further interpreted such basin shape changes as vibrational contributions to the liquid fragility. The small excess vibrational entropy measured here suggests either that such basin shape changes are small, or that similar changes may be occurring in the crystal basin.

In conclusion, the high flux and detection efficiency of the ARCS neutron spectrometer made it possible to measure the phonon DOS in amorphous $Cu_{50}Zr_{50}$ and $Cu_{46}Zr_{46}Al_8$ in real time during continuous heating through the glass transition. Within the limits of statistics, there was no observable change in the phonon DOS across the glass transition for either alloy and the change in vibrational entropy during crystallization was also small. At T_g, the total excess entropy of liquid/glass $Cu_{50}Zr_{50}$ measured calorimetrically was $0.27k_B$ per atom, while the excess vibrational entropy measured from INS was $0.01k_B$ per atom at T_g. Therefore, we can conclude that the excess entropy at the glass transition is nearly all configurational in both $Cu_{50}Zr_{50}$ and $Cu_{46}Zr_{46}Al_8$.

The present result reveals that unlike molecular and network glasses, the vibrational entropy in a metallic glass (and its undercooled liquid) is approximately equal between the amorphous phase and the crystal. The implication of this result is that the excess vibrational entropy of the glass and undercooled liquid is essentially zero, and as a result the excess entropy of the amorphous phase is mostly configurational. It should also be noted that these measurements of vibrational entropy were obtained near T_g; at higher temperatures anharmonicity may cause thermodynamically significant changes in the vibrational dynamics of the liquid.

As two metallic glasses with very different fragilities were investigated, we expect this result to apply generally to all metallic glasses independent of their fragility. As such, we can conclude that the glass transition in metallic glasses is accommodated

solely by a change in configurational entropy, consistent with the classic pictureof the glass transition proposed by Gibbs and co-workers[2][37]. In the language of PEL theory, this result suggests that the excess entropy at the glass transition originates nearly entirely from the multiplicity of equivalent basins available to the material above T_g, as intrabasin vibrations through T_g do not change significantly in relation to the crystal.

Chapter 4

THERMODYNAMICS AND NUCLEATION BEHAVIOR OF $Pt_{57}Cu_{23}P_{20}$ AND $Pt_{60}Cu_{20}P_{20}$

4.1 Abstract

The supercooled liquid configurational enthalpy referenced to the crystalline state of two ternary alloys based on the $Pt_{57}Cu_{23}P_{20}$ eutectic are measured and show that the Kubachewski expression for the heat capacity of metallic glasses does not explain the data. The enthalpy in the undercooled liquid from the liquidus to the nose shows a startlingly low heat capacity which is unexplainable with current models of metallic glass thermodynamics. Undercooling is improved with cycling even in the absence of flux and allowed for the collection of the enthalpy data. Fragility measurements of the eutectic alloy demonstrate the very fragile nature of this system.

4.2 Introduction

The canonical expression for the thermodynamics of metallic glasses in the liquid state is the Kubachewski relation, given in the preceding chapter as:

$$c_p(T)_{liq} = 3k_B + aT + bT^{-2} \tag{4.1}$$

The origin of this expression was originally formulated by Hoch and Vernardakis[32] in 1976. The expression was used to fit data for a collection of pure metals near the liquidus. The leading term comes from the high temperature Debye limit and the second term derives from anharmonicity. The third term, bT^{-2}, had no explained physical significance but rather was chosen to fit the data. It was later written in Kubaschewski *et al.*[45] where it gets its name. Later interpretations of the expression explained that term by the Gaussian shape of the basins in an inherent configurational state potential energy distribution[77]. This term then represents the excess configurational enthalpy of the liquid.

This expression is widely used in the metallic glass literature, but it is by no means the only expression. Another expression for the configurational contribution used

is only linear in temperature[47][93], but once again no physical mechanism is used to explain the form of the expression, it is based on experimental results.

The heat capacity and enthalpy of these liquids is often hard to measure for undercooled metallic glasses, so often the total enthalpy of the liquid is referenced to a given crystal state as a function of temperature:

$$\Delta H(T)_{l-x} = \Delta H_f - \int_T^{T_f} \Delta c_p^{l-x}(T')\mathrm{d}T' \tag{4.2}$$

with the Δc_p term given by the differences in heat capacities between the liquid and crystal states, Δc_p^x being given by Eq 3.7, the bounds of integration being the temperature being evaluated and the melting temperature, and ΔH_f being the heat of fusion. The heat capacity of crystals is generally well understood due to the ease in measuring heat capacities and lack of many fundamental experimental challenges that liquids present, though the heat capacity of liquids is generally much more difficult. If it is assumed that both the crystal and liquid exhibit contributions of the form in Eq. 4.1, and further assumed the first two terms are roughly equal, then this difference represents the configurational contribution of the liquid as discussed in Chapter 3.

4.3 Methods

Experiments were carried out in a Netzsch 404C DSC (which, despite the name, is a DTA). Samples were measured in specially-made quartz DSC crucibles. In comparison to the experiments in Chapter 1, there is no alumina sample pan as shown in Fig. 1.4, with these experiments having the bottom of the quartz being flattened and perpendicular to the walls of the crucible.

Undercooling was performed with no active fluxing agent. In comparison to other experiments of noble metal metallic glasses looking at the near liquidus thermodynamic behavior[49][93][56], no boron oxide was used. This was done for two main reasons. Firstly, this alloy system did not require B_2O_3 to achieve significant undercooling so using fluxing was unnecessary. Secondly, calibrating experimental designs involving B_2O_3 is very challenging as the presence of B_2O_3 does not merely add its own signal but changes the heat flow profile of the sample. Given that these are measured in a DTA, where changes in temperature are backed out from

temperature differentials at a fixed point relative to the sample, changes in the heat flow profile can change the measured signal.

The sample was first heated from room temperature to 700°C at 20°C min^{-1}, then cooled at 20°C min^{-1} to 200°C, and then cycled between 200°C and 700°C until limited by the number of program steps the Netzsch software allowed. An ultra high-purity argon flow of 30 ml min^{-1} was used as the atmosphere.

Calibration was performed using a sapphire standard. Two calibrations were made, one for heating and one for cooling, which necessitated doing the calibrations in an external program. Because the sapphire and sample have different heat flow profiles due to the differences in how they are situated in the crucible, the sapphire was used as a relative calibration compared with the heat of fusion. A sample ran separately at 5°C min^{-1} with the corresponding calibration provided the absolute value of the heat of fusion.

A roughly 50 mg sample was used for these experiments. The material was provided by Dr. Na at Glassimetal Technologies who processed these alloys with no flux.

4.4 Results

4.4.1 $Pt_{57}Cu_{23}P_{20}$

As can be seen in Fig. 4.1, there are two primary nucleation pathways for crystallization in the undercooled liquid. One nucleation pathway for shallow undercoolings starts at 470°C and has a shoulder, with crystallization of the remaining liquid starting roughly 20°C lower. The second primary pathway occurs at deeper undercoolings around 370°C, with a single, sharp crystallization event. There are several runs that nucleate in an intermediate temperature range, and it is unclear whether this is due to a less potent heterogeneous nucleation events that are only occasionally expressed or due to small perturbations in the system which induce premature nucleation.

The effects of cycling can be seen in Fig. 4.2. After the first seven cycles the alloy transitioned to nucleating from the nucleation pathway with the shoulder to nucleating at significantly lower temperatures in single, sharp nucleation events. This transition to deep undercooling was semi-permanent, although occasional runs would nucleate at the shallow undercooling temperatures or at intervening temperatures. However, even samples that nucleated at temperatures near the original temperatures did not have a shoulder and nucleated more or less in single sharp

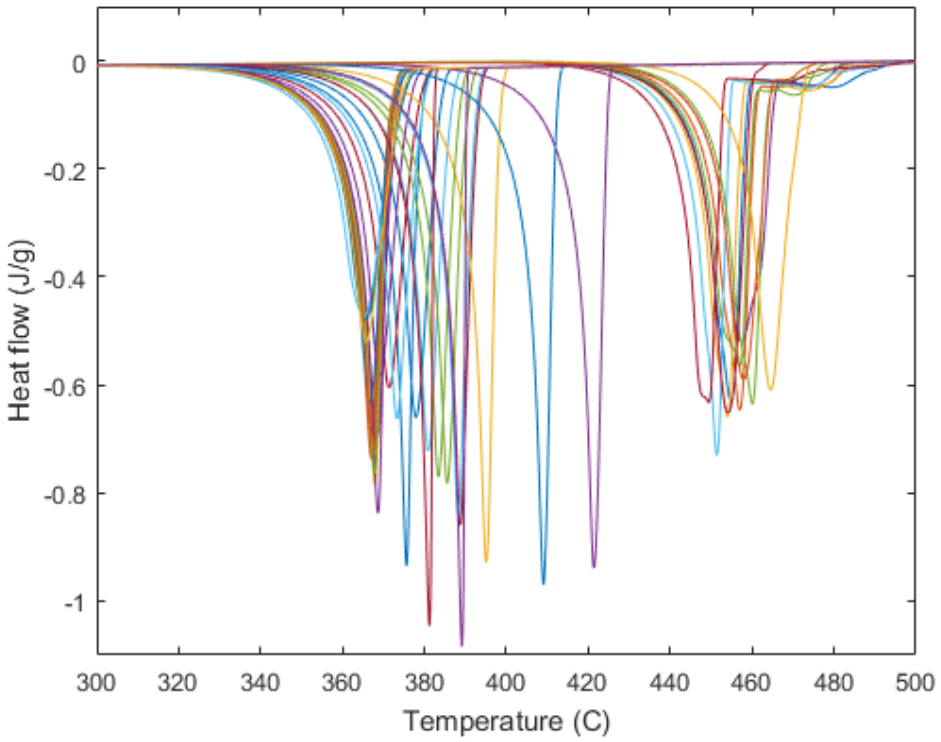

Figure 4.1: Nucleation of undercooled $Pt_{57}Cu_{23}P_{20}$. $Pt_{57}Cu_{23}P_{20}$ was cycled and demonstrated a cycling effect. There exist two main nucleation pathways clustered around 470°C and 370°C, each due to some heterogeneous nucleation pathway. The ability to undercool below that initial 470°C nucleation event suggests some mechanism to either clean the sample or reduce the effect of impurities.

events. Nucleation at these deep undercoolings seemed to have a lower bound of 650K.

Enthalpy of the crystalliation of the undercooled liquid is shown in Fig. 4.3. The high temperature data above roughly 755K shows an apparent offset compared to data even just below 755K. The seven data point above 755K were the first seven cycles of the run before any significant undercooling could occur and may result in a different microstructure and final crystallized state. The offset, if it is a manifestation of physical phenomena and not noise or some artifact of the data, would be on the order of roughly 3% of the total enthalpy of crystallization. It is likely that this offset represents slightly different crystallization products. Figs. 4.4 and 4.5 show the heating curves that occur subsequent to crystallization of the liquid. While the melting transition itself is very similar between runs, there are signals in the

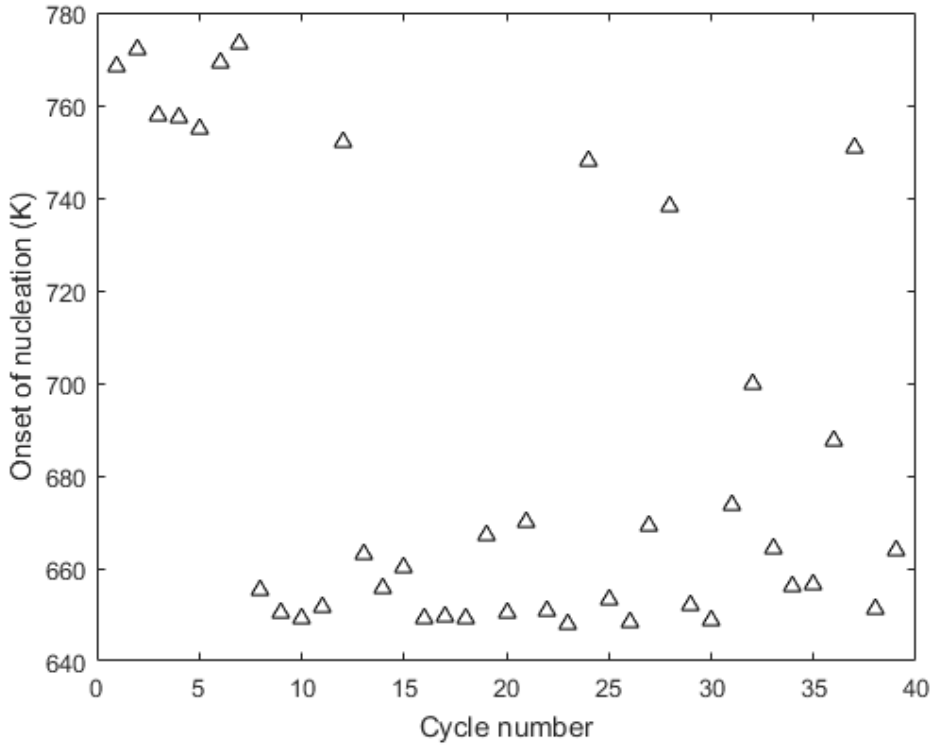

Figure 4.2: Undercooling behavior with cycling for $Pt_{57}Cu_{23}P_{20}$. The onset of nucleation of $Pt_{57}Cu_{23}P_{20}$ is plotted against the number of cycles. There is a transition at the 8th cycle where the alloy transitions to a lower nucleation temperature, though occasional runs revert to the higher nucleation threshold. There is a roughly 100K increase in undercooling due to this transition, with some scatter, but seemingly is bounded by 650K as the deepest undercooling.

crystal before melting that can vary substantially. There exist two different heating behaviors, with either two large, diffuse exothermic bumps at 400°C and 490°C or with an exothermic signal right before melting at roughly 530°C. The crystallization events with the shoulder, which corresponded with the offset, correspond also to the events at 530°C.

Even including the offset, above 670K there is very little change in crystallization enthalpy. The liquidus is 840K and T_g is 500K, so through 50% of the supercooled liquid region there is between 2-5% change in the excess enthalpy of the liquid compared to the crystallized state, depending on the inclusion of the offset. Below 670K there is a large change in the trend of the enthalpy. It is hard to draw strong conclusions because nucleation occurred before more undercooling could be

achieved, and this is at the limits of the cooling rate capabilities of the Netzsch DSC in this temperature range. What the data show is that there is roughly a 5% change in enthalpy between 650K and 670K, comparable to or even exceeding the entire enthalpy change in the 670K to 840K range. Apparently, the configurational enthalpy of the liquid is nearly constant over a broad range of T, then drops rapidly below this range.

The signals in the heating curves are small, but not negligible. One challenge in measuring the magnitude of the signals is that the bounds of the signal are hard to determine, and may overlap with melting. Depending on the bounds of integration used, the broad peaks amount to between 3% and 10% of the total heat of fusion. The signal for the near melting transition peak is around 2% and 3% of the heat of fusion, with possible additional signal preceding that event. The blue curve in Fig. 4.5 that peaks near 430°C is anomalous in that it is a single peak and does not correspond to any apparent differences in the crystallization behavior for the preceding or following cooling cycles.

Viscosity was measured using a three-point bending fixture more fully described in Chapter 2 with the results shown in Fig. 4.6. The Angell fragility was measured to be 67.1 with fitting parameters T_g=500.1K, n=1.55, and η_∞ was set to $4x10^{-5}$.

4.4.2 $Pt_{60}Cu_{20}P_{20}$

$Pt_{60}Cu_{20}P_{20}$ was cycled in the same manner as the eutectic alloy and demonstrated a cycling effect on the amount of undercooling and the nucleation pathway as can be seen in Fig. 4.7. Similarly to the eutectic alloy, there is an improvement in undercooling as a function of cycling, which can be seen in Fig. 4.9. The first 17 runs were scattered exhibit an average undercooling to around 490°C. These runs also exhibited a shoulder, which was significantly broader than the eutectic for the highest onset nucleation events, but eventually fully merged into a single broader crystallization event below around 455°C. After the 17th run a transition occurred which caused crystallization to occur at significantly lower temperatures and with a single, sharp crystallization event. These averaged around 80K lower in temperature for the onset of nucleation, but scattering was very high and the highest temperature crystallization events were very similar in temperature and character to the lowest crystallization events from the first set of runs.

Undercooling of $Pt_{60}Cu_{20}P_{20}$ showed a similar if even more pronounced trend than

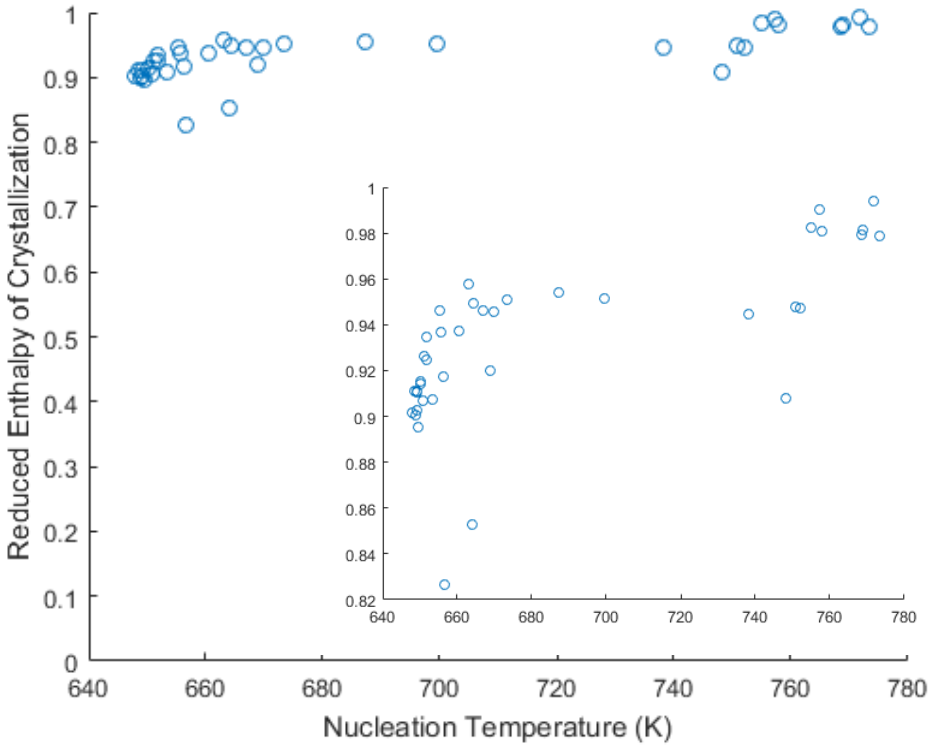

Figure 4.3: Reduced enthalpy of crystallization of $Pt_{57}Cu_{23}P_{20}$. The enthalpy of crystallization was scaled by the heat of fusion, which was 74 J/g. The inset shows the data scaled to show the data in higher detail.

the eutectic $Pt_{57}Cu_{23}P_{20}$. Due to the slightly higher liquidus temperature and lower GFA for the hypoeutectic alloy undercooling did not proceed to lower T as far as in the eutectic. The enthalpy data is shown in Fig. 4.8, and it can be seen that undercooling the melt by 150K results in very little change in enthalpy, on the order of 2-3%. In comparison to the eutectic alloy, there appears to be no offset in crystallization enthalpy at shallow undercooling versus deep undercooling, with with the higher nucleating temperature crystals within 1% of the lower nucleating temperature crystals.

Melting of $Pt_{60}Cu_{20}P_{20}$ is shown in Fig. 4.10. In comparison to the eutectic alloy, the melting behaviors of the crystalline sample vary somewhat among the runs. There is no broad exothermic signals far before melting, but there is still some signal 20°C before melting in these runs. Some runs show a slight melting shoulder that begins at the solidus of the majority of the runs, but does not fully begin melting until

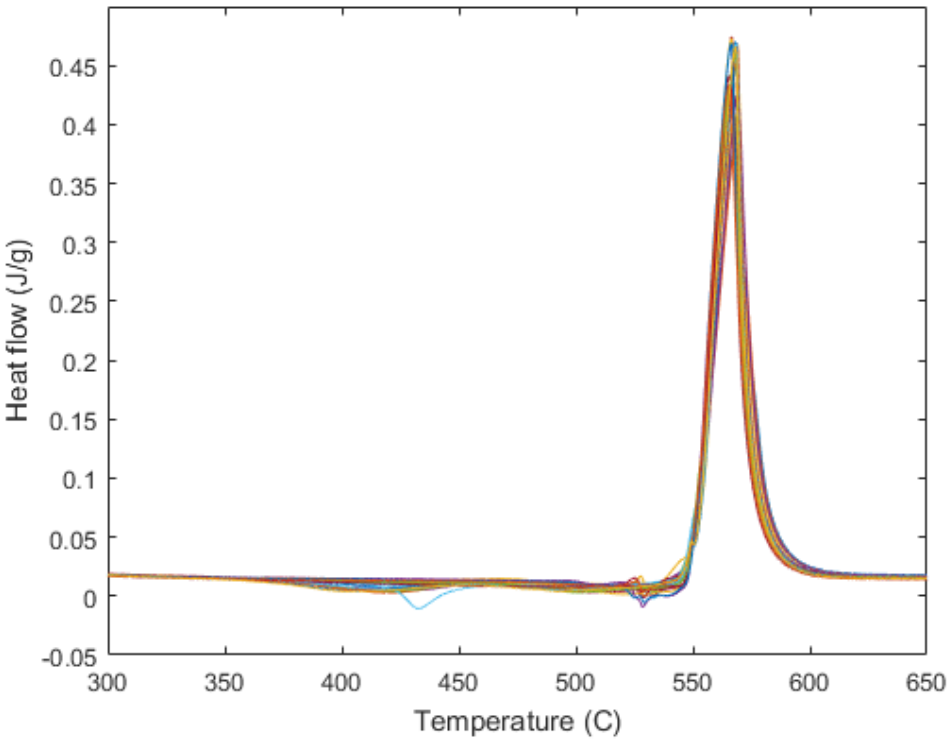

Figure 4.4: Heating curves of $Pt_{57}Cu_{23}P_{20}$. Superimposed heating curves of $Pt_{57}Cu_{23}P_{20}$ through melting with scanning rates of 20°C min^{-1}.

5°C higher. These runs all occur following the transition to deeper undercooling, though not all runs after that transition exhibited this behavior. The longer-tailed melting transition curves occurred following the first 8 cycles but otherwise seemed unremarkable. The pre-melting signal was small for these alloys, on the order of 2% of the heat of fusion.

Viscosity measurements for this alloy were attempted but accurate data could not be attained. No samples could be equilibrated during flow without crystallizing, even at low temperatures with very low loads and strain rates. This alloy had a similar ΔT as the eutectic alloy, with similar T_g and nucleation behavior in the DSC. At temperatures slightly above kinematic T_g and with 20mN forces in the TMA, deflections were below $3x10^{-10}$ m s^{-1}, with strain rates in the 10^{-7} range. Apparently crystallization is induced in flows at very low strain rates. Similar, but likely stronger, alloys transition to non-Newtonian behavior at strain rates several orders of magnitude higher[41]. In the cooperative shear model, strain rates this

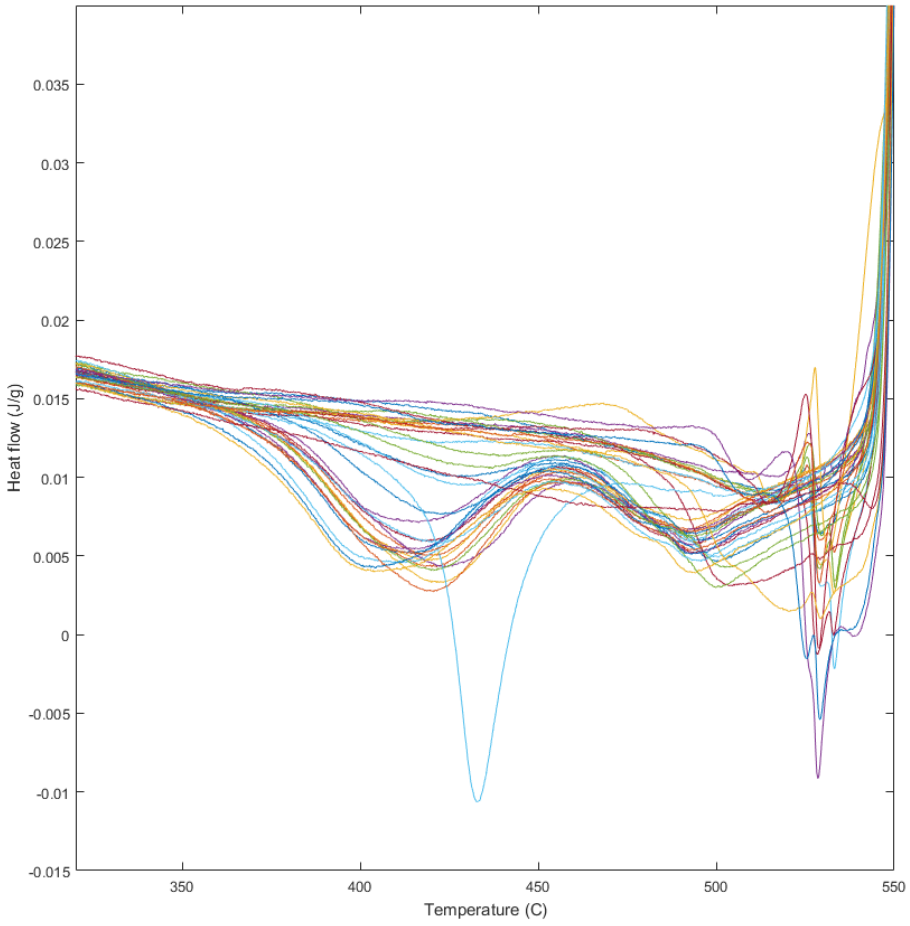

Figure 4.5: Heating curves of $Pt_{57}Cu_{23}P_{20}$. Zoomed in view of pre-melting behavior of $Pt_{57}Cu_{23}P_{20}$.

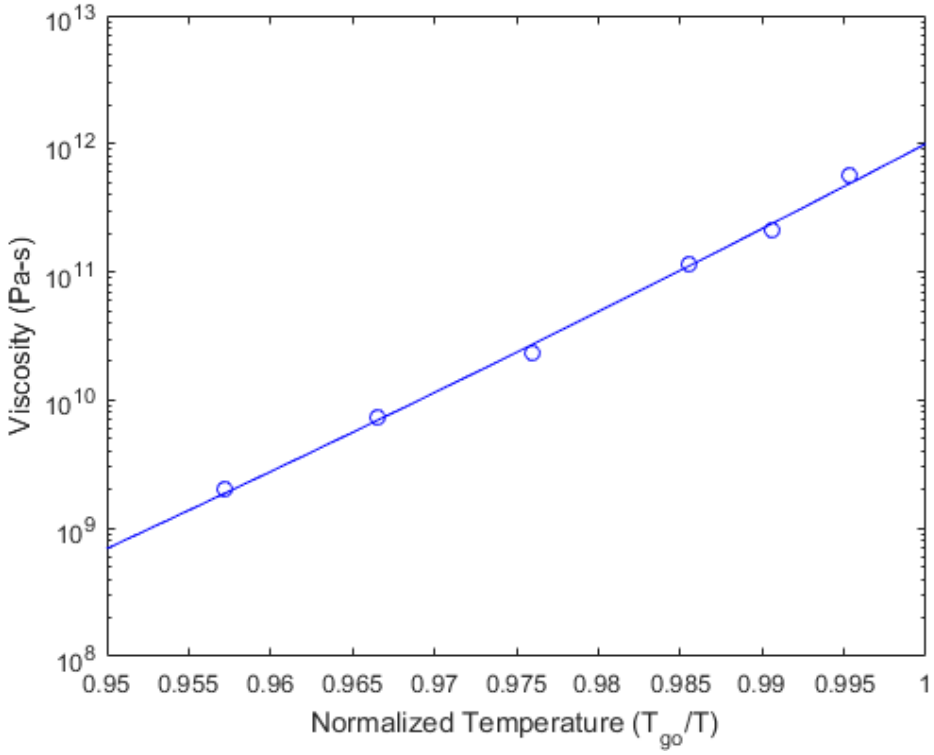

Figure 4.6: Angell plot of $Pt_{57}Cu_{23}P_{20}$. Fragility of $Pt_{57}Cu_{23}P_{20}$ was measured to be 67.1.

low should be orders of magnitude below that necessary to transition to a non-Newtonian flow, and even in the non-Newtonian regime there is no reason to expect that crystallization would be induced at these temperatures and strain rates. This alloy shows anomalous strain rate behavior in the undercooled liquid as well. The measured GFA (critical casting thickness) of the alloy was found to increase by a factor of 3x if minor shear stresses were reduced during casting (from personal discussion, see footnote)[1]. The normal processing route has alloy melted in a quartz tube; that alloy is brought to equilibrium above the liquidus temperature, and the quartz tube is quenched in a soapy water mixture and gently stirred to increase the cooling rate. By not stirring the quartz tube, the cooling rate is lowered, but the GFA for this alloy increased by a factor of three, with everything else kept constant. This strongly suggests that crystal nucleation rates are dramatically increased by shear flow.

[1]Communication with Prof. William L. Johnson, California Institute of Technology, December 2017

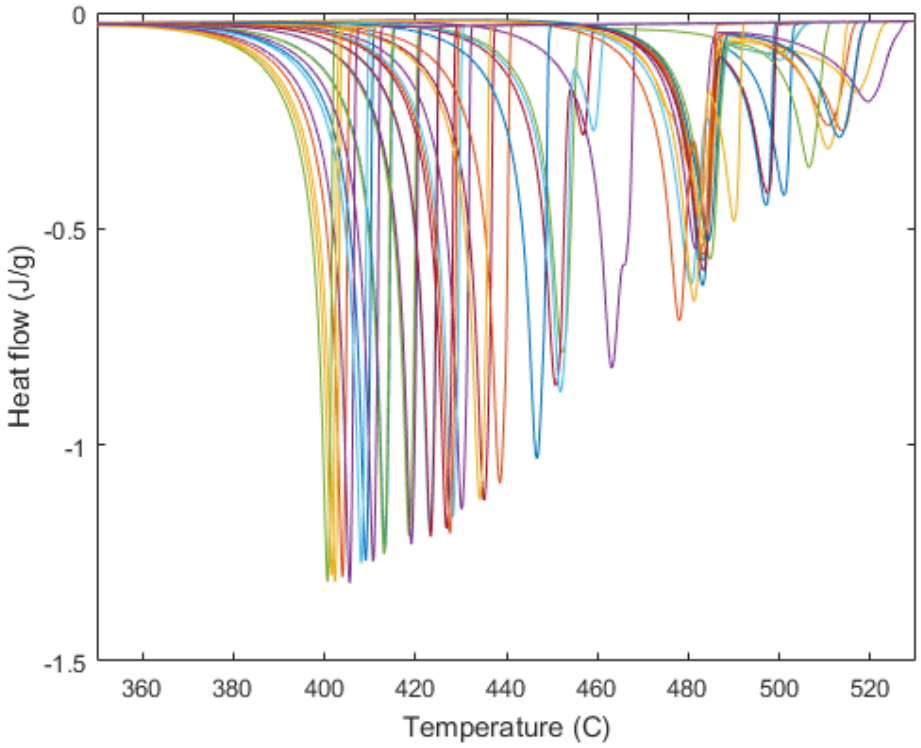

Figure 4.7: Nucleation of undercooled $Pt_{60}Cu_{230}P_{20}$. The first seventeen crystallization events had the the highest nucleation temperatures and exhibited a shoulder in crystallizing, but subsequent runs were uniformly single, sharp crystallization events with lower nucleation onset temperatures.

4.5 Discussion

It is unclear what caused the jump in undercooling during cycling of these glasses. Since no active fluxing was used the only method of cleaning the sample would be fluxing from the SiO_2. This process would be a rather slow process given that the experimental temperatures are far below the glass transition of SiO_2 and diffusion would be very slow, though glass encapsulation is known to improve undercooling in glass systems[85]. Fluxing from the SiO_2 could occur through a process similar to that observed in B_2O_3 fluxing. Overheating is another possible explanation, though in other overheating experiments the overheating temperatures that lead to deeper undercooling tend to be further above the liquidus and do not require cycling to achieve improvements in undercooling. In cycling experiments of gold Wilde *et al.* showed that cycling improved the undercooling linearly until plateauing at a fixed temperature[92]. Because there is a difference in the crystals being nucleated it is

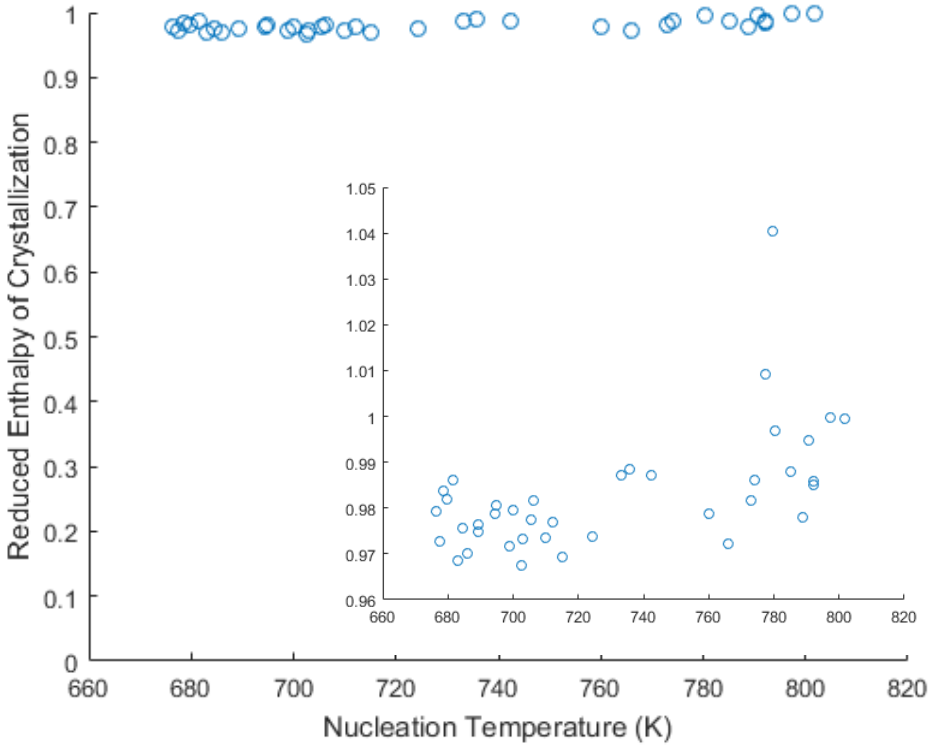

Figure 4.8: Reduced enthalpy of crystallization of $Pt_{60}Cu_{20}P_{20}$. The enthalpy of crystallization was scaled by the heat of fusion. The inset shows the same data scaled to show higher detail.

likely that there is either some heterogenous nucleating agent that is progressively eliminated by the cycling and slight overheating of the experiment. The failure to maintain the deep undercooling in all subsequent runs could be due to a failure to getter the incoming atmosphere, the continued presence of oxide or other nucleating particles that occasionally reform after melting, or the presence of other external sources of noise (like vibrations) that may trigger nucleation at higher temperatures through the strain rate effect already noted above.

Deeper undercooling may be possible. The easiest way to achieve deeper undercooling would be to cool the sample more quickly. Because the eutectic alloy undercooled to what is likely the nose of the TTT-diagram, small further increases in cooling rates should allow access to the entire supercooled liquid region. True DSCs should be able to achieve higher cooling rates due to the significantly smaller thermal mass of the system, though given the temperature limitations potential chal-

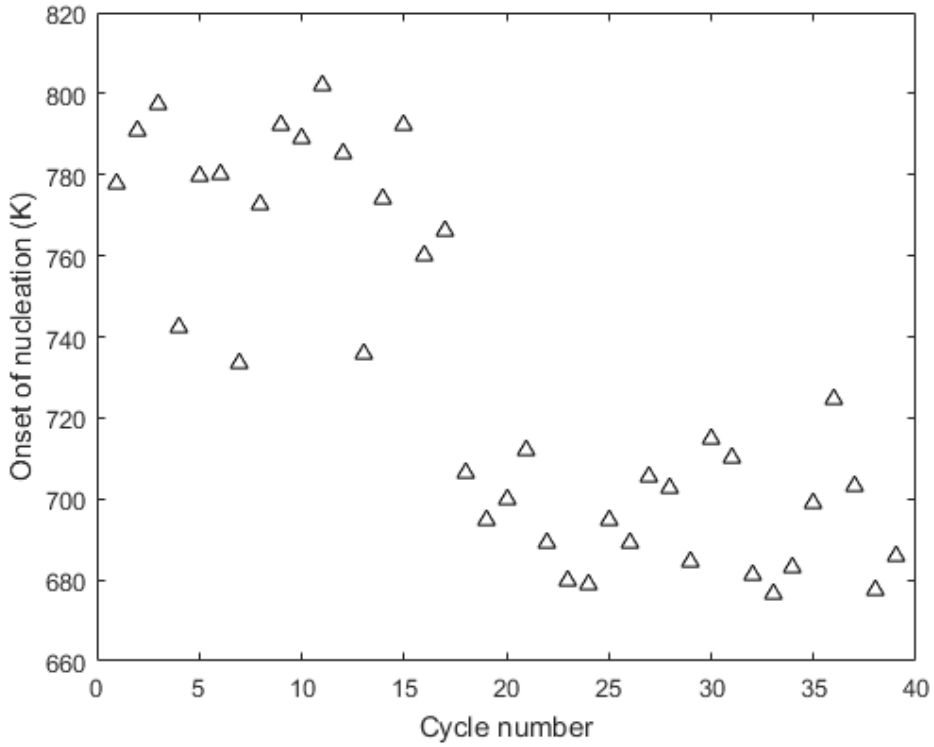

Figure 4.9: Undercooling behavior with cycling for $Pt_{60}Cu_{20}P_{20}$. The onset of nucleation of $Pt_{60}Cu_{20}P_{20}$ is plotted against the number of cycles. There is a transition at the 18th cycle where the alloy permanently transitions to a lower nucleation temperature, but the variance in nucleation temperature onset before and after this transition remains substantial. The increase in undercooling at this threshold is slightly less than that for the eutectic alloy.

lenges with overheating might limit the ability to dissolve heterogeneous nucleation sites. Systems with active cooling should also be able to achieve necessary cooling rates to at least explore the effect of deeper undercooling, if not bypass crystallization completely. Newer flash DSC instruments should be able to not only easily bypass the TTT-nose but also perform isothermal measurements. Isothermal measurements would be an improvement over the current scanning measurements because while this data shows that the enthalpy is released over a relatively small temperature range, and relaxation times should be more than sufficiently quick, isothermal crystallization would allow for somewhat higher quality data than can be achieved by scanning.

Löffler has carried out separate experiments and found 4 phases in the fully crystal-

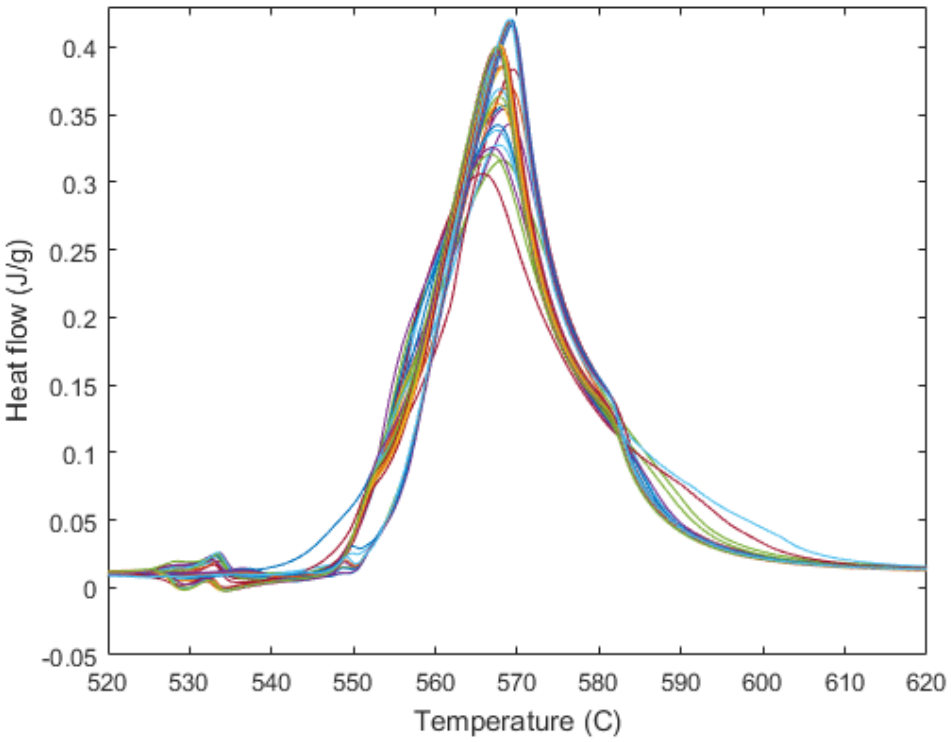

Figure 4.10: Heating curves of $Pt_{60}Cu_{20}P_{20}$. Superimposed heating curves of $Pt_{60}Cu_{20}P_{20}$ through melting with scanning rates of 20°C min^{-1}

lized eutectic liquid(from personal discussion, see footnote)[2]: a P-rich Pt-P binary alloy, likely PtP_2; two Pt-Cu phases with the higher Cu phase having some phosphorus; and a Pt-rich phase with phosphorus and some copper, likely based on the Pt_5P_2 crystal with copper in a solid solution with the platinum. The Pt-Cu phases are likely based on a solid solution for the more Pt-rich phase and an ordered PtCu phase for the higher Cu phase. Because phosphorus has very little solubility in platinum but upwards of 3.5% in Cu, the presence of phosphorus with platinum indicates either a Pt-P compound or copper allowing for some solubility.

The Gibbs phase rule says that there should only be three crystal phases in equilibrium for a three component alloy, so the presence of a fourth phase indicates that in crystallizing the melt a metastable crystal phase is formed that does not transform to equilibrium. In the binary Pt-P system there are actually two eutectics separated by a miscibility gap. In the liquid near the $Pt_{80}P_{20}$ eutectic the preferred crystal phases

[2]Communication with Prof. Dr. Jörg F. Löffler, ETH Zurich, December 2017

are PtP_2 and Pt. It is only below the eutectic temperature of 590°C, but not significantly below it, that the Pt_5P_2 phase becomes stable and Pt_2P_5. Any undercooling below the eutectic temperature would preferentially nucleate the Pt_5P_2 phase and a Pt phase given the compositional proximity to the melt, but there may be very P-rich liquid or PtP_2 crystallites that have already formed. Given the large separation in composition space, and the slow kinetics of diffusion in crystals, two Pt-P phases exist when in equilibrium only one would be expressed. This may also explain the shoulder of the crystallization curves at high temperature, but more work is needed to validate that hypothesis.

The shape of the enthalpy curve in Fig. 4.3 is quite remarkable. The percentage change in enthalpy from the liquidus to near the nose is less than 10%, with half of that change coming in the last 20 degrees. The flatness of the enthalpy curve below the liquidus is unprecedented in the literature, and the sharp downturn near the TTT-nose is hard to explain. It would be wrong to draw too many conclusions from the slope of the downturn below 670K. Given that this is right at the limit of this experiment's ability to undercool, there may be some additional noise due to clustering many data points around a small temperature range. If there is a sharp downturn starting at this temperature, the fact that these measurements were obtained by scanning as opposed to isothermal experiments might raise questions regarding the ability of the scans to adequately represent fully relaxed, equilibrium behavior. This would not fundamentally change that the conclusion that some phenomenon occurred at that temperature range, but rather the specific details of the ehat release profile would be open to interpretation. Since this is near the TTT-nose, the possibility of a phase change in the liquid cannot be ruled out.

There are good reasons to suspect that configurational changes in the liquid are driving the sharp downturn in ΔH^{l-x}. As detailed in chapter III, the differences in vibrational entropy between selected metallic glass liquids, crystals, and glasses are virtually indistinguishable, indicating that configurational changes are dominating any enthalpy changes. While the exact nose temperature of the TTT diagram is not precisely known, it is likely that undercooling to midway between T_g and T_L should be very close to the nose temperature, where any changes in liquid structure would more likely result in crystallization and manifest as a shorter time to crystallization. The common expression for liquid heat capacity, Eq. 4.1, has a T^{-2} term which at first glance suggests a similar qualitative primary shape to the enthalpy data curve.

In Eq. 4.2 the only temperature dependence in the heat of crystallization arises from the integral of c_p^{l-x}. Because the heat capacity of the crystal as given in Eq. 3.7 has no terms that show any qualitative similarity to enthalpy data, it is the integral of c_p^l that drives the configurational enthalpy. While a first glance indicates similarity between the liquid heat capacity expression and the data, integrating the liquid term gives a T^{-1} expression for enthalpy, which does not come close to explaining the sharp changes and flat slopes of the curves above the TTT-nose seen in Fig. 4.3.

Taking the rather sudden drop of enthalpy curves observed in the eutectic alloy at face value, a liquid-liquid phase transition is possible. There are significant challenges in finding these transitions in glass-forming liquids, but evidence has been reported for a liquid-liquid phase transition in Vitreloy 1[89], and indirect support for these transitions in the form of strong to fragile crossovers in viscosity curves in similar systems[88][19]. In comparison to previous work, the alloys in this work are significantly more fragile than the Vitreloy alloys. Additionally, the liquid-liquid transition in Vitreloy 1 appears above the liquidus, whereas the present work suggests a transition in the supercooled liquid near the TTT-nose. This increases the challenge of determining if a transition occurs as the timescales for experiments becomes significantly shorter. Additionally, it is likely a different physical mechanism is in play from the particulars of that transition.

Jong Hyun Na has observed a very steep rise in the enthalpy of crystallization at low temperatures near T_g for the present alloys. The low temperature enthalpy data was measured by isothermal crystallization using a Netzsch DSC, and somewhat higher temperature data was measured with rapid discharge heating. The results are shown in Figs. 4.11 and 4.12 with the high temperature data measured by undercooling in the present work.

Two points are immediately apparent when looking at the overall enthalpy data in these figures: the fit given by the power law shows the inability of the standard heat capacity expression to capture the thermodynamics of these alloys, and a single function fits the data quite well. The latter point suggests that if a liquid-liquid phase transition exists near the TTT-nose it would likely be a transition with a small change in configurational enthalpy, such that distinguishing the transition would not be possible without carefully mapping out the configurational enthalpy on both sides of the transition. The overall data is fit to a power law of the form[3]:

[3]Publication in preparation

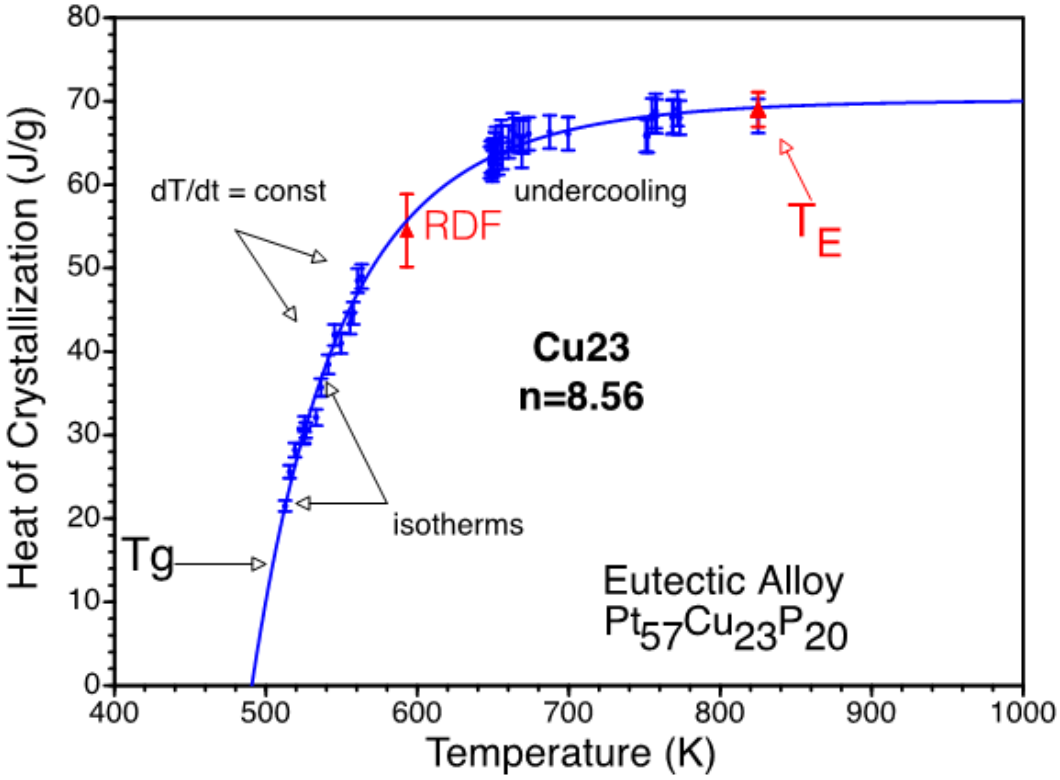

Figure 4.11: Configurational Enthalpy of $Pt_{57}Cu_{23}P_{20}$. The configurational enthalpy of the liquid referenced to the crystal state is plotted against temperature. Moving from left to right the different techniques used to collect the data are labeled. The techniques were isothermal crystallization, constant heating rate DSC measurements, rapid discharge forming, and undercooling. The curve was fit to Eq. 4.3 and the fitting parameters were Θ_h=490 K, $h_c(\infty)$ = 70.2 J/g, and n=8.56.

$$\frac{h_c(T)}{h_c(\infty)} = \left[1 - \left(\frac{\Theta_h}{T}\right)^n\right] \tag{4.3}$$

where $h_c(T)$ is the liquid configurational enthalpy, $h_c(\infty)$ is the limit of the configurational enthalpy as $T \rightarrow \infty$, Θ_h is a sample dependent characteristic isenthalpic temperature, and the exponent n will be interpreted as a sample dependent thermodynamic "fragility" index for the liquid and should not be confused with the n fitting parameter from the cooperative shear model.

The exponent n in Eq. 4.3 is 1 for the standard Gaussian distribution of inherent states in a potential energy landscape as described in the introduction. The eutectic $Pt_{57}Cu_{23}P_{20}$ has a fitted n of 8.56 and the hypoeutectic $Pt_{60}Cu_{20}P_{20}$ has a fitted n of 12.9. Given the amount of data collected, it is extremely unlikely that the

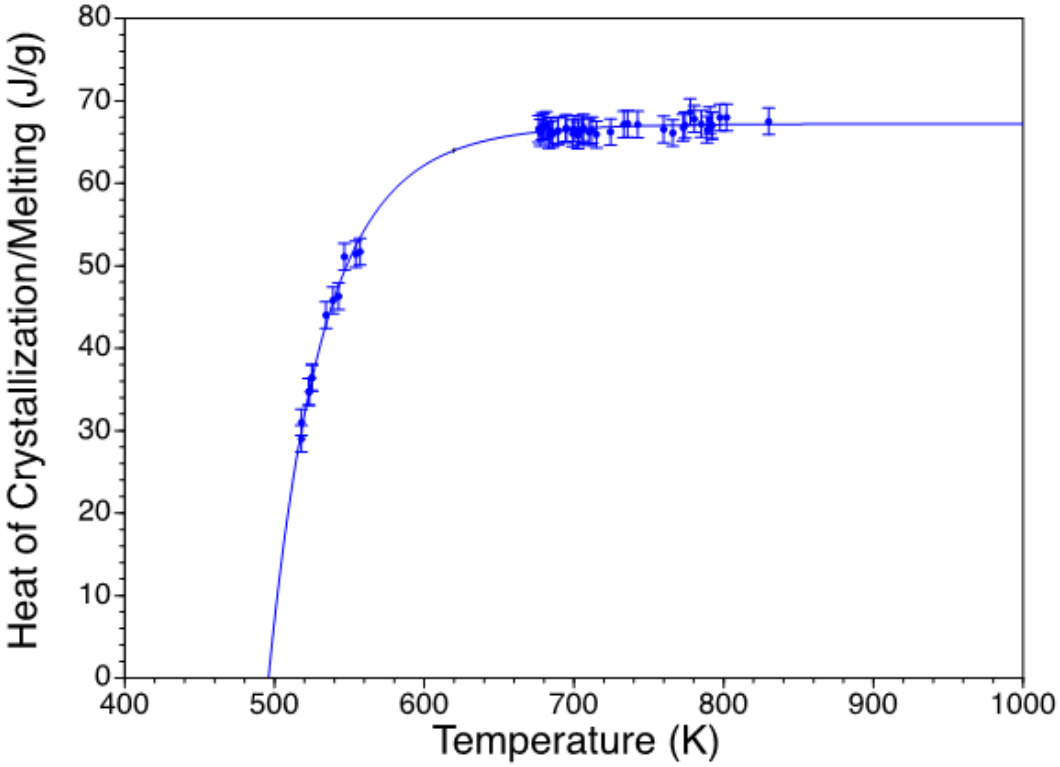

Figure 4.12: Configurational Enthalpy of $Pt_{60}Cu_{20}P_{20}$. The configurational enthalpy of the liquid referenced to the crystal state is plotted against temperature. The curve was fit to Eq. 4.3 and the fitting parameters were Θ_h=495 K, $h_c(\infty)$ = 67.1 J/g, and n=13.7.

deviations from a T^{-1} are due to noisy data. Because different measurements, using different instruments, techniques, operators, and locations give results that independently validate this large deviation from T^{-1} it is unlikely to be a systematic error. Such large deviations from the Gaussian model indicate that the physics of these alloys is not described by the standard Gaussian PEL framework. Putting the curves from Figs. 4.12 and 4.11 along with Vitreloy 1b, a relatively strong metallic glass, into the dimensionless units of Eq. 4.3 gives Fig. 4.13. In the case of a pure Gaussian landscape, where n=1, the graph would show a straight line with slope of -1, intersecting the x and y axes at 1.

The steepness of these curves near the glass transition have another implication- configurational entropy of these glasses referenced to the crystal state extrapolate to zero extremely close to T_g. Unless there is an inflection point and the curve stretches out at lower T, the Kauzmann temperature is almost exactly at T_g. For the eutectic

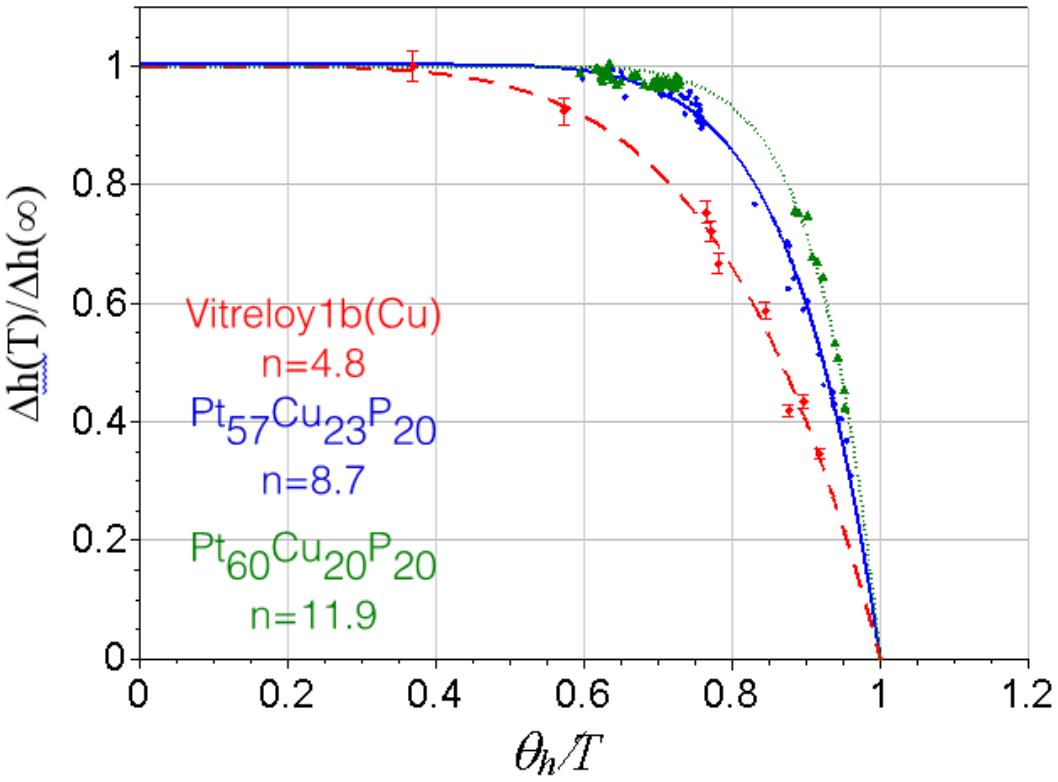

Figure 4.13: Dimensionless plot of configurational enthalpy versus inverse temperature. Eq. 4.3 was used to fit the data of this work as well as Vitreloy 1b, a relatively strong metallic glass

$Pt_{57}Cu_{23}P_{20}$ alloy, the Kauzmann temperature, T_K, is 501 K. The calorimetric T_g is 506 K and the rheological T_g is 506 K. This implies that the relaxed liquid at T_g is as ordered as the crystalline alloy. Even as the entropy goes to zero, there exists a residual configurational enthalpy. For both $Pt_{57}Cu_{23}P_{20}$ and $Pt_{60}Cu_{20}P_{20}$ the residual enthalpy is around 30% of the high temperature enthalpy limit.

Previous work on $Pt_{57.3}Cu_{14.6}Ni_{5.3}P_{22.8}$, a similar but likely significantly stronger glass former, showed different behavior that could be reasonably fit by a Gaussian expression[49]. Because $Pt_{57}Cu_{23}P_{20}$ is a eutectic alloy that crystallizes in one crystallization event at low temperature we can anchor the bottom of the curve, which gives us significantly more confidence in our data. Another key difference is that the addition of Ni likely makes the alloy stronger, with fragility measured from the DSC giving m=50 compared with the eutectic alloy with m=73 measured with beam bending. Other metallic glass alloys where the thermodynamics were measured tend to either have only a few data points near T_g and T_L[76][24][20],

are very strong glass formers[12][93], or both[11]. Interestingly, the only alloy with as complete a set of data, work that was done on $Pd_{40}Ni_{40}P_{20}$[93], also shows a deviation from T^{-1} behavior, but this relatively strong glass demonstrates T^1 behavior in c_p and T^2 behavior in enthalpy, which is a puzzling result on its own and markedly deviates from a Gaussian model.

The Pt-Cu-P ternary alloy system has advantages over other metallic glass alloys in measuring equilibrium configurational enthalpy over a wide range of temperatures in the supercooled liquid region. The measured alloys crystallize in a single, sharp nucleation event over a wide range of temperatures. In the temperature range that these alloys do not have a sharp crystallization event the crystallization shoulder is relatively small. Other systems, particularly other Pd- and Pt-based glasses, are often very far from a eutectic composition and have significantly more complicated melting or crystallization pathways. Due to the high ΔT and GFA and low T_L a significant portion of the supercooled liquid region could be accessed. These alloys lack any reactive metals, which allowed the samples to be processed indefinitely in quartz. These alloys exhibited undercooling improvement due to cycling, which allowed for a single sample to provide enthalpy data over a wide range of crystallization temperatures near T_L using the same experimental conditions.

Lastly, near T_g heat capacity in the supercooled liquid state is often collected instead of isothermal crystallization data. The challenge with continuous scans is that the relaxation timescales near T_g are often quite long, significantly longer than the timescale of the scan. In deeply undercooled liquids relaxation is not an exponential process, and instead follows a stretched exponential Kohrausch relaxation law (KWW), given by:

$$\Delta S(t) \sim e^{-(t/\tau)^{\beta}} \tag{4.4}$$

At the rheological T_g (viscosity of 10^{12} Pa·s), relaxation of the stretched exponential takes 10^3-10^4 s, as determined by heat capacity spectroscopy measurements on molecular glasses.[7][36][97][96] While relaxation does occur, and often a significant portion of the relaxation occurs on an experimentally relevant timescale, the liquid is not fully equilibrated by the time a new temperature is sampled in a continuous scan. This can be partially ameliorated by doing step calorimetry, which is quasi-isothermal, but full equilibration has not yet occurred by the next step.

Isothermal experiments at low temperature are very challenging, which is why it is rarely done. Crystallization events which look very sharp in a continuous scan will, in the best circumstances, spread out dramatically due to slower kinetics. The large majority of the time, the crystallization spreads from one peak to multiple peaks, and occasionally cannot be fully crystallized isothermally on any relevant experimental timescale. The signals become very small, making the data noisier. Alloys need a sufficiently high ΔT to fully equilibrate before crystallizing, but too high a ΔT results in waiting days or even weeks for crystallization to occur near T_g. These platinum alloys are ideal glasses to do these measurements. Their ΔT allows for measurements near T_g to crystallize in about 2-3 days, and at higher temperatures the time decreases markedly. Crystallization happens in a single peak, but only after the sample has annealed at T_g for a sufficient amount of time. In these experiments, the sample was held at T_g for 24 hours before ramping and holding at the desired measurement temperature. If this step did not occur, a secondary crystallization peak of around 10% of the primary crystallization peak would occur during ramping the temperature up to melting.

Because collecting high quality thermodynamic data in the supercooled liquid region is challenging there is not a good pre-existing experimentally-validated framework to interpret these results. Looking at the form of the data, a very surprising inference can be drawn — the hypoeutectic $Pt_{60}Cu_{20}P_{20}$ looks much more like a Heaviside function than a Gaussian distribution of inherent states. A Heaviside function in enthalpy would define a first order phase transition, with the alloy transitioning from a frozen, glassy configuration to a liquid. This phase transition would correspond to $n \rightarrow \infty$ in Eq. 4.3, a result that would likely be impossible to realize in a physical system for two primary reasons. Firstly, it would be impossible to see a sharp phase transition due to configurational changes because glasses and liquids are inherently disordered, and transitioning from one disordered state to another disordered state would be limited by the inherently different local configurations, which would smear out any signal. Secondly, the phase transition would be in the infinitely fragile limit. While no direct connection between the thermodynamic fragility parameter n in Eq. 4.3 and the Angell fragility parameter m exists, initial analysis suggests that the two are correlated, and in the same way that m is limited in physical systems, n should also be finite.

The nature of such a phase transition is not clear from this work. Indeed, the

underlying physical mechanism that explains this data is not immediately obvious. A physically plausible explanation for this behavior would be the existence of an onset of cooperativity in undercooled liquids. This has sometimes been referred to in the glass literature as the onset of "frustration"[83]. Above some transition temperature, the liquid exists as free shear transformation zones (STZs)[41][15] unconstrained by any other STZs. Below this transition temperature, Eschelby stress fields generated by neighboring STZs introduce cooperativity between STZs. In the limiting case of the phase transition, this onset of cooperativity is instantaneous and nearly total, whereas in more physically realizable systems a more gradual transition would be expected. In the opposite limit behavior similar to SiO_2 would be expected. There would be essentially no changes in cooperativity and the only effect is due to the breaking and recreation of single bonds, analogous to the rearrangement of free STZs. In terms of enthalpy, the limiting cases represent a Heaviside function for the phase transition and a perfect fit to a Gaussian landscape model (T^{-1} in enthalpy) for the free STZ case.

This transition on cooling from a liquid to a configurationally frozen glass has kinetic in addition to thermodynamic implications. In the infinitely fragile limit, a liquid would transition from Arrhenius behavior with a very low activation energy and low (~mPa·s) viscosity above the phase transition to a glass-like viscosity (10^{12} Pa·s) instantaneously, analogous to crystallization. Looking at physically realizable systems, the almost non-existant configurational enthalpy change from near the liquidus to far into the supercooled liquid in $Pt_{60}Cu_{20}P_{20}$ suggests that the high temperature viscosity of these very fragile glasses may exhibit remarkably low viscosity far into the supercooled liquid before rapidly rising until reaching the glass transition. If this mechanism is the origin of these effect, current models of viscosity for glass formers would not be able to capture the physics in these systems. A model that posits an onset in cooperativity in the supercooled liquid would be inconsistent with current viscosity models. The mechanism governing viscosity changes between near T_g and near T_L would be different. The models currently used to describe viscosity over the entirety of its supercooled liquid range, including the best current model for viscosity in metallic glasses, the cooperative shear model, all assume a single mechanism. While deviations from the cooperative shear model are likely to minor, as the model already accounts for not-significant cooperativity at high temperatures, it would be important to account for the differing underlying physical mechanisms in this new explanation.

This alloy system presents an amazing opportunity to better understand and study glass physics. Initial work on alloys further away from the eutectic on the hypoeutectic side indicate even more extreme thermodynamic behavior, while still having decent GFA, workable ΔT, and reasonable crystallization and melting behavior. Additional work, computational, theoretical, and experimental, would be needed to really understand the origin of the behavior in this system. In the short term, easy steps would be to measure the thermodynamics of this alloy system in an ultra-fast DSC to confirm the thermodynamics as well as to map out the entirely of the enthalpy in the undercooled liquid. This should especially be done for alloys that are further away from the eutectic, particularly on the hypoetuctic side. Understanding the nature of the liquid could be very helpful, and computational modelling on the structure of this alloy in the liquid state at and near the eutectic could give valuable insight into the system. This could be matched with additional experimental data, such as capillary flow viscometry or ultrasonic shear modulus to better understand the kinetic behavior of the alloys in the liquid and supercooled liquid state. Collecting synchrotron data for determining structure of the liquid, supercooled liquid, glass, and crystal could go a very long ways to explain the data, particularly near T_g where the configurational entropy of the equilibrium liquid seems to be close to zero.

Chapter 5

CONCLUDING REMARKS

5.1 Conclusion

This thesis is broken down into two parts, the first shows the story of glass forming ability, starting from the processing of metallic glasses and how it affects undercooling and following that by developing a model of glass forming ability in a series of Ni-based glasses. The second part is closely related, and details some experiments into the nature of the glass transition. The thesis explores this first by neutron scattering and calorimetry experiments to show that vibrational entropy does not contribute to excess entropy of the glass transition and then by undercooling experiments in a pair of Pt-based metallic glasses which showed very unexpected behavior.

The undercooling behavior of $Ni_{71.4}Cr_{5.52}Nb_{3.38}P_{16.67}B_{3.03}$ is unexpected and shows promising results. The sporadic deep undercooling in cycling experiments indicates that there exists an alloy that likely exhibits significantly better intrinsic GFA than can be achieved via normal processing routes. The challenge in achieving this intrinsic GFA may be due to the difficulty in fully removing heterogeneous nucleation pathways. Fluxing seems to be necessary to achieve these deep undercooling events, but it also seems to introduce nucleation pathways that express at higher temperatures. The origin of these sporadic deep undercooling events is unexplained.

Glass forming ability can be fully explained by two experimentally determined parameters: the Angell fragility parameter m and the reduced glass transition temperature T_{rg}. This was shown in a Ni-based metallic glass system that was characterized over a wide variety of compositions surrounding the GFA peak alloy $Ni_{69}Cr_{8.5}Nb_3P_{16.5}B_3$. The fragility of the alloys over a 1.5at.% variation in boron composition changed from 58 to 77. This rapid change in fragility is an indication of rapid changes in the local atomic order and is a key driver of increased glass forming ability improvement in this alloy system.

The vibrational entropy through the glass transition is measured using neutron scattering experiments for $Cu_{50}Zr_{50}$ and $Cu_{46}Zr_{46}Al_8$. When combined with additional calorimetry work on these systems, the excess entropy for these alloys through the

glass transition show effectively no contribution from vibrational entropy; the contribution is entirely due to configurational entropy. This result is likely extendable to metallic glasses in general, as $Cu_{50}Zr_{50}$ and $Cu_{46}Zr_{46}Al_8$ span a wide range of fragilities.

And finally, the enthalpy of crystallization below the liquidus was measured for a pair of Pt-based metallic glasses — $Pt_{57}Cu_{23}P_{20}$ and $Pt_{60}Cu_{20}P_{20}$. These glasses exhibit remarkable enthalpy data, with the hypoeutectic $Pt_{60}Cu_{20}P_{20}$ demonstrating almost no change in enthalpy (~2% of the heat of fusion) from the liquidus down to around halfway through the supercooled liquid region. This data was combined with isothermal crystallization measurements near T_g to demonstrate enthalpy of crystallization data that showed behavior suggestive of smeared first order phase transitions. These effects have never been seen in the literature before for any metallic glass system and are not explained by the current models of liquid thermodynamics of metallic glass systems.

5.2 Future work

The results of Chapter 4 present an excellent opportunity and jumping off point to explore fundamental glass physics. A couple experiments that would be very worthwhile to pursue are detailed below.

5.2.1 Evaluating Pt-based alloys with Cu content less than 20%

While the alloys measured in Chapter 4 show remarkable behavior, it is likely that creating and testing alloys with less than 20% copper (commensurately increasing platinum) would demonstrate enthalpy of crystallization data even closer to that of a step function. There are several experimental considerations that would complicate the experiments, but these challenges are likely surmountable.

Creating samples of these hypoeutectic alloys is challenging. The severe strain rate sensitivity demonstrated by $Pt_{60}Cu_{20}P_{20}$ in the supercooled liquid region upon cooling indicates that sample preparation is substantially more difficult than the large majority of metallic glasses. Traditional metrics like GFA are not as helpful in determining the ability to make these glasses. However, the GFA of glasses with sub 20% copper should be above 2 mm for a not insignificant composition range given the high demonstrated GFA of the 20% alloy (>10 mm with optimized processing). The lower the Cu content, the more fragile the system will be.

Other important metrics like ΔT are likely to become less optimal the more hypoeutectic the composition, but given the relatively large ΔT of the starting alloys, there's room to fall while still giving enough processing window to equilibrate before crystallizing at low temperature. A bigger problem is going to be ensuring consistent crystallization pathways, particularly for undercooled liquids. Moving away from the eutectic is likely going to change the nucleation pathway, and it will certainly reduce the amount of undercooling that can be performed. Care will need to be taken to ensure the products of crystallization are the same given different starting temperatures and equilibrium states.

5.2.2 Measuring enthalpies of crystallization using flash calorimetry

A large limitation of the calorimeters available for this study are the limited cooling and heating rates available. Modern flash calorimeters should not have these same limitations and should be able to measure the enthalpies of crystallization over the entire supercooled liquid range.

Flash calorimetry presents several advantages over the current methodologies. The heating and cooling rates available on flash calorimeters are orders of magnitude higher than what can be achieved using traditional calorimeters. This increase in cooling rate allows for the creation of glasses in the calorimeter and hence the sampling of enthalpy data over the entire supercooled liquid. For the eutectic $Pt_{57}Cu_{23}P_{20}$ alloy such cooling rates will be unnecessary, as it is likely that marginal increases in the cooling rate compared to our experimental rates (20 K min^{-1}) will allow cooling past the TTT-nose. For more marginal glasses, including the hypoeutectic alloys, the increased cooling rates will allow access to the regions of the supercooled liquid that would not be accessible using other techniques. The rapidity in heating and cooling also could allow for rapid temperature changes to a target temperature followed by an isothermal hold, allowing for isothermal crystallization measurements over the entire supercooled liquid range. Given the advantages of isothermal crystallization (detailed in the Chapter 4 discussion), this could improve the confidence in the results detailed so far.

Flash calorimeters require substantially smaller samples than traditional calorimeters, and so glasses with more marginal GFAs can be measured. An additional possible analysis enabled by the large range in heating rates will be to look at the change in heat capacity through the glass transition over a wide range of glass

transition temperatures.

5.2.3 Viscosity of alloys near $Pt_{57}Cu_{23}P_{20}$

A detailed study of the composition dependence of Angell fragility has not been studied in metallic glasses. Very fragile systems likely present more interesting physics, and this alloy system, due to the high fragility of these Pt-alloys, even near the eutectic, provides an ideal range to study the composition dependence of fragility. While the hypoeutectic alloys are likely to be unmeasurable due to strain rate induced crystallization below a yet to be determined composition, the change in fragility near the eutectic is likely quite rapid.

The work in Chapter 2 detailing the very high composition dependence of fragility on boron content is likely to be mirrored in this system as a function of copper content. Mapping the fragility of these alloys could give significant insight into the origin of fragility. The model used in Chapter 2 to fit the boron data was an exponential fit and is very likely nonphysical. However, no good model of fragility as a function of composition exists. This is a limitation of the GFA model developed in that chapter, as it limits the predictive power to systems that are already reasonably well characterized.

A related avenue of research would be to look at the strain rate effects near T_g by using three-point beam bending. Starting from the relatively stronger glasses and moving compositionally towards the more fragile glasses, an onset of strain rate induced crystallization for a given strain rate should be observed. This induced crystallization is not understood, and mapping the relationship between strain rate induced crystallization with fragility, strain rate, and composition could well help understand this phenomenon. This can be extended to higher strain rates by using an Instron compression setup, allowing for strain rate effects to be seen for even stronger glasses.

Another related avenue of research would be to look at the high temperature viscosity of these alloys. This is going to be significantly more difficult, but could certainly be done for exemplary compositions. The high temperature viscosity data may provide corroborating insights into the physical mechanism in play, particularly if a transition from Arrhenius to super-Arrhenius behavior is seen (as would be predicted if a cooperativity mechanism is driving the thermodynamic effects). The challenges to this are several-fold. Firstly, the relatively high strain rates needed in

most experimental designs for high temperature viscosity measurements are likely well within the range to begin high temperature crystallization of the hypoeutectic alloys. Secondly, the relatively low temperatures could make imaging of the sample difficult against dark backgrounds, which puts significantly more design constraints of a capillary flow viscometer. This is because readily imaginable designs might use graphite susceptors to create a mostly uniform temperature environment, though other approaches may not have these same challenges. Thirdly, the high density and presence of phosphorus preclude easily using an electrostatic levitator.

5.2.4 Other Experiments

The three experiments detailed in the last section were ones where the equipment to perform the measurement would be readily available to subsequent researchers at Caltech. There are numerous other experiments that would be very valuable, some of which will be very briefly described, and the list will certainly not be fully enumerated.

The ordering of these alloys at low temperature is very substantial. Measurements of the structure of these alloys using pair distribution functions and other techniques might help shed light on the ordering of liquids that are almost ideal. Due to the close proximity of the Kauzmann temperature to the glass transition temperature, the enthalpy and entropy of these alloys can be measured in energy ranges that are inaccessible to other systems. Performing neutron scattering experiments on these nearly ideal glasses would be a very interesting addition to the calorimetric work already performed.

Shear modulus of these alloys through the supercooled liquid region are likely to demonstrate very strong declines in shear modulus with increasing temperature above the glass transition. Performing in situ ultrasonic measurements[51] of the supercooled liquid could show remarkable elastic properties. Mechanical data for these alloys should be quite interesting. There is likely a positive correlation between Angell fragility and toughness, and given the very high fragility of these alloys toughness is possibly comparably high.

There is undoubtedly much more that can be done with these alloys. The most constructive initial data would be data collected to try and help create or validate a model to explain the phenomena already measured. Once a model is developed to explain the behavior of these alloys, other experiments will undoubtedly present

themselves.

BIBLIOGRAPHY

[1] D. L. Abernathy et al. “Design and operation of the wide angular-range chopper spectrometer ARCS at the Spallation Neutron Source”. In: *Review of Scientific Instruments* (2012).

[2] G. Adam and Gibbs. J.H. “On the temperature dependence of cooperative relaxation properties in glass-forming liquids”. In: *Journal of Chemical Physics* (1965).

[3] P. B. Allen. “Anharmonic phonon quasiparticle theory of zero-point and thermal shifts in insulators: heat capacity, bulk modulus, and thermal expansion”. In: *Physical Review B* (2015).

[4] C. A. Angell. “Spectroscopy simulation and scattering, and the medium range order problem in glass”. In: *J. Non-Cryst. Solids* (1985).

[5] O. et al Arnold. “Mantid–data analysis and visualization package for neutron scattering and μ sr experiments”. In: *Nucl. Instrum. Methods Phys. Res. A* (2014).

[6] Hamid Assadi and Jan Schroers. “Crystal nucleation in deeply undercooled melts of bulk metallic glass forming systems”. In: *Acta Materialia* (2002).

[7] N.O. Birge. “Specific heat spectroscopy of Glycerol and Propylene Glycol near the glass transition”. In: *Physical Review B* (1986).

[8] R. Böhmer et al. “Nonexponential relaxations in strong and fragile glass formers”. In: *The Journal of Chemical Physics* (1993).

[9] G. Borelius. “On the theory of conversion of metallic mixed phases, IV. The excretion of unordered mixed phases”. In: *Annalen Der Physik* (1937).

[10] R. Busch. “The thermophysical properties of bulk metallic glass-forming liquids”. In: *JOM* (2000).

[11] R. Busch, Y.J. Kim, and W.L. Johnson. “Thermodynamics and kinetics of the undercooled liquid and the glass transition of the $Zr_{41.2}Ti_{13.8}Cu_{12.5}Ni_{10}Be_{22.5}$ alloy”. In: *Journal of Applied Physics* (1995).

[12] R. Busch, W. Liu, and W.L. Johnson. “Thermodynamics and kinetics of the $Mg_{65}Cu_{25}Y_{10}$ bulk metallic glass forming liquid”. In: *Journal of Applied Physics* (1998).

[13] H.S. Chen and D. Turnbull. “Evidence of a Glass-Liquid Transition in a Gold-Germanium-Silicon Alloy”. In: *The Journal of Chemical Physics* (1968).

[14] P. G. Debenedetti and F. H. Stillinger. “Supercooled liquids and the glass transition”. In: *Nature* (2001).

[15] M.D. Demetriou et al. “Cooperative Shear Model for the Rheology of Glass-Forming Metallic Liquids”. In: *Physical Review Letters* (2006).

[16] P.J. Desre, E. Cini, and B. Vinet. “Homophase-fluctuation-mediated mechanism of nucleation in multicomponent liquid alloys and glass forming ability”. In: *Journal of Non-Crystalline Solids* (2001).

[17] M. Dresch et al. “Neutron scattering measurements of phonons in nickel at elevated temperatures”. In: *Phys. Rev. B* (2007).

[18] Zach Evenson and Ralf Busch. “Equilibrium viscosity, enthalpy recovery and free volume relaxation in a $Zr_{44}Ti_{11}Ni_{10}Cu_{10}Be_{25}$ bulk metallic glass”. In: *Acta Materialia* (2011).

[19] Z. Evenson et al. “High temperature melt viscosity and fragile-to-strong transition in Zr-Cu-Ni-Al-Nb(Ti) and $Cu_{47}Ti_{34}Zr_{11}Ni_8$ bulk metallic glasses”. In: *Acta Materialia* (2012).

[20] G.J. Fan et al. “Thermodynamics, enthalpy relaxation and fragility of the bulk metallic glass-forming liquid $Pd_{43}Ni_{10}Cu_{27}P_{20}$”. In: *Acta Materialia* (2004).

[21] Michael Floyd. “Development of Ferromagnetic Metallic Glasses into Low Loss Power Transformer Cores”. PhD thesis. California Institute of Technology, 2017.

[22] Brent Fultz et al. *Experimental Inelastic Neutron Scattering with a Chopper Spectrometer*. 2016.

[23] E. L. Gjersing, S. Sen, and B. G. Aitken. “Vibrational entropy near glass transition in a chalcogenide glass and supercooled liquid”. In: *J. Non-Crys. Solids* (2009).

[24] S.C. Glade et al. “Thermodynamics of $Cu_{47}Ti_{34}Zr_{11}Ni_8$, $Zr_{52.5}Cu_{17.9}Ni_{14.6}Al_{10}Ti_5$ and $Zr_{57}Cu_{15.4}Ni_{12.6}Al_{10}Nb_5$ bulkd metallic glass forming alloys”. In: *Journal of Applied Physics* (2000).

[25] M. Goldstein. “Viscous liquids and the glass transition: a potential energy barrier picture”. In: *J. Chem. Phys.* (1969).

[26] M. Goldstein. “Viscous liquids and the glass transition. V. Sources of the excess specific heat of the liquid”. In: *J. Chem. Phys* (1976).

[27] D. Granata et al. “Fluxing of Pd-Si-Cu bulk metallic glass and the role of cooling rate and purification”. In: *Acta Materialia* (2014).

[28] D. Granata et al. “The detrimental effect of flux-induced boron alloying in Pd-Si-Cu bulk metallic glasses”. In: *Applied Physics Letters* (2015).

[29] P. D. Gujrati and M. Goldstein. "Viscous liquids and the glass transition. 9. Nonconfigurational contributions to the excess entropy of disordered phases". In: *J. Chem. Phys* (1980).

[30] F.Q. Guo, S.J. Poon, and G.J. Shiflet. "Enhanced bulk metallic glass formability by combining chemical compatibility and atomic size effects". In: *Journal of Applied Physics* (2005).

[31] H.E. Hagy. "Experimental Evaluation of Beam-Bending Method of Determining Glass Viscosities in teh Range of 10^8 to 10^{15} Poises". In: *Journal of the American Ceramic Society* (1963).

[32] M. Hoch and T. Vernardakis. "Thermophysical Properties of Liquid Metals". In: *Berichte der Bunsengesellschaft für physikalische Chemie* (1973).

[33] Douglas C. Hofmann et al. "Designing metallic glass matrix composites with high toughness and tensile ductility". In: *Nature* (2008).

[34] A. Inoue, T. Zhang, and T. Masumoto. "Glass-forming ability of alloys". In: *Journal of Non-Crystalline Solids* (1993).

[35] Akihisa Inoue, Nobuyuki Nishiyama, and Hisamichi Kimura. "Preparation and Thermal Stability of Bulk Amorphous $Pd_{40}Cu_{30}Ni_{10}P_{20}$ Alloy Cylinder of 72 mm in Diameter". In: *Materials Transactions, JIM* (1997).

[36] Y.H. Jeong and I.K. Moon. "Ergodic-nonergodic glass transition and enthalpy relaxation of a supercooled liquid $Ca(NO_3)_2$-KNO_3". In: *Physical Review B* (1995).

[37] Gibbs. J.H. and E. A. Dimarzio. "Nature of the glass transition and the glassy state". In: *Journal of Chemical Physics* (1958).

[38] Q. K. et al. Jiang. "Zr-(Cu,Ag)-Al bulk metallic glasses". In: *Acta Mater.* (2008).

[39] G. P. Johari. "Contributions to the entropy of a glass and liquid and the dielectric relaxation time". In: *J. Chem. Phys* (2000).

[40] G. P. Johari. "The entropy loss on supercooling a liquid and anharmonic contributions". In: *J. Chem. Phys.* (2002).

[41] William L. Johnson et al. "Rheology and Ultrasonic Properties of Metallic Glass-Forming Liquids: A Potential Energy Landscape Perspective". In: *MRS Bulletin* (2007).

[42] W.L. Johnson, J.H. Na, and Demetriou M.D. "Quantifying the origin of metallic glass formation". In: *Nature Communications* (2016).

[43] K.F. Kelton and A.L. Greer. *Nucleation in Condensed Matter*. 2010.

[44] W. Klement, R.H. Willens, and P.O.L. Duwez. "Non-crystalline structure in solidified gold-silicon alloys". In: *Nature* (1960).

[45] O. Kubaschewski, C.B. Alcock, and P.J. Spencer. *Materials Thermochemistry*. 1993.

[46] H. W. Kui, A. L. Greer, and D. Turnbull. "Formation of bulk metallic glass by fluxing". In: *Applied Physics Letters* (1984).

[47] Hin-Wing Kui and David Turnbull. "The Heat Capacity of $Ni_{40}Pd_{40}P_{20}$". In: *Journal of Non-Crystalline Solids* (1987).

[48] Lind M. L., Duan G., and Johnson W. L. "Isoconfigurational elastic constants and liquid fragility of a bulk metallic glass forming alloy". In: *Physical Review Letters* (2006).

[49] Benjamin A. Legg, Jan Schroers, and Ralf Busch. "Thermodynamics, kinetics, and crystallization of $Pt_{57.3}Cu_{14.6}Ni_{5.3}P_{22.8}$". In: *Acta Materialia* (2007).

[50] X. H. Lin, W. L. Johnson, and W. K. Rhim. "Effect of Oxygen Impurity on Crystallization of an Undercooled Bulk Glass Forming Zr-Ti-Cu-Ni-Al Alloy". In: *Materials Transactions, JIM* (1997).

[51] Mary Laura Lind. "Ultrasonic Investigation of the Elastic Properties and Liquid Fragility of Bulk Metallic Glasses in the Supercooled Liquid Region". PhD thesis. California Institute of Technology, 2008.

[52] Mary Laura Lind, Gang Duan, and William L. Johnson. "Isoconfigurational Elastic Constants adn Liquid Fragility of a Bulk Metallic Glass Forming Alloy". In: *Physical Review Letters* (2006).

[53] Guang-qiao Liu et al. "Effect of TRT process on GFA, mechanical properties and microstructure of Zr-based bulk metallic glass". In: *Progress in Natural Science: Materials International* (2011).

[54] Zengqian Liu et al. "Pronounced ductility in CuZrAl ternary bulk metallic glass composites with optimized microstructure through melt adjustment". In: *AIP Advances* (2012).

[55] Boonrat Lohwongwatana, Jan Schroers, and William L. Johnson. "Strain Rate Induced Crystallization in Bulk Metallic Glass-Forming Liquid". In: *Physical Review Letters* (2006).

[56] I.-R. Lu et al. "Thermodynamic properties of Pd-based glass-forming alloys". In: *Journal of Non-Crystalline Solids* (1999).

[57] Z.P. Lu and C.T. Liu. "A new glass-forming ability criterion for bulk metallic glasses". In: *Acta Materialia* (2002).

[58] L.-M. Martinez and C.A. Angell. "A thermodynamic connection to the fragility of glass-forming liquids". In: *Nature* (2001).

[59] S. Mukherjee et al. “Overheating threshold and its effect on time-temperature-transformation diagrams of zirconium based bulk metallic glass”. In: *Applied Physics Letters* (2004).

[60] Jong Hyun Na, Marios D. Demetriou, and William L. Johnson. “Fragility of iron-based glasses”. In: *Applied Physics Letters* (2011).

[61] Jong Hyun Na et al. “Bulk nickel-based chromium and phosphorus bearing metallic glasses with high toughness”. In: *U.S. Patent 9863024* (2018).

[62] Jong Hyun Na et al. “Compositional landscape for glass formation in metal alloys”. In: *PNAS* 111.25 (2014), pp. 9031–9036. DOI: 10.1073/pnas.1407780111.

[63] K. et al. Ohsaka. “Specific volumes of the $Zr_{41.2}Ti_{13.8}Cu_{12.5}Ni_{10}Be_{22.5}$ alloy in teh liquid, glass, and crystalline states”. In: *Appl. Phys. Lett.* (1997).

[64] J. Orava and A.L. Greer. “Fast and slow crystal growth kinetics in glass-forming melts”. In: *The Journal of Chemical Physics* (2014).

[65] J.H. Perepezko and J.S. Paik. “Thermodynamic properties of undercooled liquid metals”. In: *Journal of Non-Crystalline Solids* (1984).

[66] D.N. Perera. “Compilation of the fragility parameters for several glass-forming metallic alloys”. In: *Journal of Physics: Condensed Matter* (1999).

[67] W. A. Phillips et al. “Dynamics of glassy and liquid selenium”. In: *Phys. Rev. Lett.* (1989).

[68] K. Russew et al. “Thermal behavior and melt fragility number of $Cu_{100-x}Zr_x$ glassy alloys in terms of crystallization and viscous flow”. In: *J. Phys. Conf. Ser.* (2009).

[69] Jan Schroers and William L. Johnson. “Crystallization of $Zr_41Cu_12Ni_10Be_23$”. In: *Materials Transactions, JIM* (2000).

[70] Jan Schroers and William L. Johnson. “Highly processable bulk metallic glass-forming alloys in the Pt-Co-Ni-Cu-P system”. In: *Applied Physics Letters* (2004).

[71] F. Sciortino. “Potential energy landscape description of supercooled liquids and glasses”. In: *J. Stat. Mech.* (2005).

[72] V. Sears, E. Svensson, and B. Powell. “Phonon density of states in vanadium”. In: *Can. J. Phys.* (1995).

[73] Oleg N. Senkov. “Correlation between fragility and glass-forming ability of metallic alloys”. In: *Physical Review B* (2007).

[74] T. D. Shen and R. D. Schwarz. “Bulk ferromagnetic glasses prepared by flux melting and water quenching”. In: *Applied Physics Letters* (1999).

[75] Hillary L. Smith. “Phase Transformations and Entropy of Non-Equilibrium Materials”. PhD Thesis. Caltech, 2014.

[76] Hillary L. Smith et al. “Separating the configurational and vibrational entropy contributions in metallic glasses”. In: *Nature Physics* 13 (2017), pp. 900–906. DOI: 10.1038/NPHYS4142.

[77] Robin J. Speedy. “Relations between and Liquid and Its Glasses”. In: *The Journal of Physical Chemistry B* (1999).

[78] F. H. Stillinger. “A topographic view of supercooled liquids and glass formation”. In: *Science* (1995).

[79] J. et al. Suck. “Dynamical structure factor and frequency distribution of the metallic glass $Cu_{46}Zr_{54}$ at room temperature”. In: *J. Phys C* (1980).

[80] G. Syrykh, M. Zemlyanov, and S. Ishmaev. “Experimental study of partial vibrational spectra in amorphous alloys”. In: *Physica B* (1997).

[81] G. Syrykh et al. “Concentration dependence of partial vibrational spectra in Ni-Nb and Cu-Zr metallic glasses”. In: *J. Non-Crys. Solids* (1999).

[82] Hajime Tanaka. “Relationship among glass-forming ability, fragility, and short-range bond ordering of liquids”. In: *Journal of Non-Crystalline Solids* (2005).

[83] G. Tarjus et al. “The frustration-based approach of supercooled liquids and the glass transition: a review and critical assessment”. In: *Journal of Physics: Condensed Matter* (2005).

[84] David Turnbull. “Under What Conditions can a Glass be Formed”. In: *Contemp. Phys.* (1969).

[85] J.L. Walker. *The physical chemistry of process metallurgy*. 1961.

[86] J. J. Wall et al. “Heterogeneous nucleation in a glass-forming alloy”. In: *Applied Physics Letters* (2008).

[87] D. C. Wallace. *Statistical Physics of Crystals and Liquids*. 2012.

[88] C. Way, P. Wadhwa, and R. Busch. “The influence of shear rate and temperature on the viscosity and fragility of the $Zr_{41.2}Ti_{13.8}Cu_{12.5}Ni_{10}Be_{22.5}$ metallic-glass-forming liquid”. In: *Acta Materialia* (2007).

[89] Shuai Wei et al. “Liquid-liquid transition in a strong bulk metallic glass-forming liquid”. In: *Nature Communications* (2013).

[90] F. W. de Wette and A. Rahman. “Inelastic scattering of neutrons by polycrystals”. In: *Phys. Rev.* (1968).

[91] Aaron Wiest. “Thermoplastic forming and related studies of the supercooled liquid region of metallic glasses”. PhD thesis. California Institute of Technology, 2010.

[92] G. Wilde, J.L. Sebright, and J.H. Perepezko. “Bulk liquid undercooling and nucleation in gold”. In: *Acta Materialia* (2006).

[93] G. Wilde et al. “Thermodynamic properties of $Pd_{40}Ni_{40}P_{20}$ in the glassy, liquid, and crystalline states”. In: *Applied Physics Letters* (1994).

[94] D.T. Wu. “Nucleation Theory”. In: *Solid State Physics* (1997).

[95] X.K. Xi et al. “On the criteria of bulk metallic glass formation in MgCu-based alloys”. In: *Intermetallics* (2005).

[96] Q. Yan, T.S. Jain, and J.J. de Pablo. “Density-of-States Monte Carlo Simulation of a Binary Glass”. In: *Physical Review Letters* (2004).

[97] C.C. Yu and H.D. Carruzzo. “Frequency dependence and equilibration of the specific heat of glass forming liquids”. In: *Physical Review E* (2004).

[98] P. Yu, H. Y. Bai, and W. H. Wang. “Superior glass-forming ability of CuZr alloys from minor additions”. In: *J. Mater. Res.* (2006).

[99] Y. Zhao and B. Zhang. “Evaluating the correlation between liquid fragility and glass-forming ability in the extremely strong Ce-based bulk metallic glasses”. In: *Journal of Applied Physics* (2017).

[100] Yanchun Zhao et al. “Overheating effects on thermal stability and mechanical properties of $Cu_{36}Zr_{48}Ag_8Al_8$ bulk metallic glass”. In: *Materials & Design* (2010).

[101] Li Zhong et al. “Formation of monatomic metallic glasses through ultrafast liquid quenching”. In: *Nature* (2014).